論文 / 著書情報
Article / Book Information

題目(和文)	水処理用芳香族ポリアミド膜およびポリベンズイミダゾール膜に関する研究
Title(English)	Fundamental Studies on Aromatic Polyamide and Polybenzimidazole Membranes for Water Treatment
著者(和文)	相羽誉礼
Author(English)	Motohiro Aiba
出典(和文)	学位:博士(工学), 学位授与機関:東京工業大学, 報告番号:甲第10114号, 授与年月日:2016年3月26日, 学位の種別:課程博士, 審査員:松本 英俊,扇澤 敏明,大塚 英幸,斎藤 礼子,早川 晃鏡
Citation(English)	Degree:Doctor (Engineering), Conferring organization: Tokyo Institute of Technology, Report number:甲第10114号, Conferred date:2016/3/26, Degree Type:Course doctor, Examiner:,,,,
学位種別(和文)	博士論文
Type(English)	Doctoral Thesis

Fundamental Studies on Aromatic Polyamide and Polybenzimidazole Membranes for Water Treatment

Motohiro Aiba

Department of Organic and Polymeric Materials,

Graduate School of Science and Engineering,

Tokyo Institute of Technology

Ph.D. Dissertation

Fundamental Studies on Aromatic Polyamide and Polybenzimidazole Membranes for Water Treatment

水処理用芳香族ポリアミド膜およびポリベンズイミダゾール膜に関する研究

2015

Motohiro Aiba

Department of Organic and Polymeric Materials,

Graduate School of Science and Engineering,

Tokyo Institute of Technology

Contents

Chapter 1

General Introduction

1.1 World water shortage

The amount of water on the earth is limited and it consists of salt water (97 %), brackish water (0.5 %), and fresh water (2.5 %).[1] Since the industrial revolution, advances in technology have made human lives safer, easier, and more comfortable so that the world's population has reached 7 billion people in 2011 and is expected to be 10 billion people by 2050. Under these circumstances, the needs of agriculture and industry for fresh water have been increased. Exploitation of groundwater aquifer and surface water has decreased the quantity of the available natural water resources. Additionally, climate changes are predicted to alter the natural availability of fresh water. For example, it is said that receding glaciers causes arterial rivers (such as Ganges, Yellow, and Mekong rivers) to become intermittent, compromising many people during the dry months. Therefore, the water scarcity mainly caused by the rapid growth of the population, industry, and agriculture has become one of the most serious problems. Presently, more than one-third of the world's population lives in water-stressed

countries and this value is predicted to be two-thirds by 2025.[2] Furthermore, water is also strongly connected with energy and food production. The shift to biofuel for alternative energy requires further fresh water for irrigation. Although several measures to address the stresses on water supply (e.g. water conservation, repair of infrastructure, and improvement of reservoir and distribution system) should be implemented, these measures can only improve the use of existing water resources not increase the amount of fresh water. The only methods to increase water supply are desalination and water reuse. Hence, the improvement in technologies for energy-efficient water purification system has become great important.

Reverse osmosis (RO) is a membrane-based desalination process and is able to reject almost colloidal or dissolved compounds from an aqueous solution and to produce fresh water. Up to now, RO has become the dominant desalination technology because of their low energy requirement (less than 4 kWh m^{-3}) compared to other technology, such as multiple effect distillation (18-30 kWh m^{-3}) and multiple stage flash distillation (24-37 kWh m^{-3})[3–5]. Indeed, the market share of RO for seawater desalination in Europe has reached 72 %.[6]

1.2 Water purification by reverse osmosis

As mentioned above, the RO process is an efficient way to produce purified water from the standpoint of energy and environment. In this section, the basic principal of the RO and some examples of the RO process have been introduced.

1.2.1 Reverse osmosis

Dissolved solutes in water generate an osmotic pressure (π), which is thermodynamically defined by the van't Hoff equation:

$$\pi = RT\sum_{i} C_i \quad (1.1)$$

where C_i is the molar concentration of dissolved the species, *i*, in the solution, R is the gas constant, and T is the absolute temperature. Thus, when two solutions with different concentrations are separated by a semipermeable membrane, there exists the osmotic pressure difference ($\Delta\pi$):

$$\Delta\pi = \Delta CRT \quad (1.2)$$

where ΔC is the salt concentration differences between solutions.

Depending on pressure gradient across the membrane, the direction of water flux through semipermeable membranes can become negative (in the direction to the high concentration solution) or positive (in the direction to the low concentration solution). The former and latter are called forward osmosis (FO) and RO. To accomplish water purification by RO, the applied pressure must be higher than the osmotic pressure difference between the salty and the fresh water. A schematic diagram of RO is shown in **Figure 1-1**.

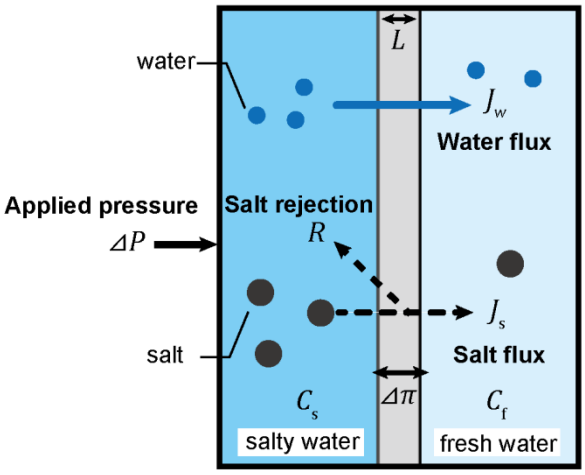

Figure 1-1 Schematic diagram of reverse osmosis

Water flux (J_w), salt flux (J_s), and salt rejection (R) are expressed as follows:

$$J_w = A(\Delta P - \Delta\pi) \qquad (1.3)$$

$$J_s = B\Delta C \qquad (1.4)$$

$$R = \left(1 - \frac{C_f}{C_s}\right) \times 100 \qquad (1.5)$$

where ΔP is the applied pressure, A is water permeability, and B is salt permeability. Basically, ΔP establishes a water concentration gradient inside the semipermeable membrane, which allows water transport by Fickian diffusion. Unlike water, a difference in salt concentrations, which causes a difference in electrochemical potential, generates a salt concentration gradient in the semipermeable membrane and drives salt transport by Fickian diffusion. Thus, J_s is not significantly affected by ΔP value.

According to "Solution-diffusion" model, which is the most accepted framework describing mass transport in a dense nonporous membrane, diffusive permeability of a penetrant (P_i) can be expressed as the product of sorption (K_i) and diffusion (D_i) coefficients:[7]

$$P_i = K_i \times D_i \quad (1.6)$$

A is related to hydraulic water permeability (P_w^H) and diffusive water permeability (P_w) as follows:

$$A = \frac{P_w^H}{L} = \frac{P_w}{L} \times \frac{V_w}{RT} \quad (1.7)$$

where V_w is molar volume of water.

From the equation (1.3) and (1.7), J_w can be rewritten as follows:

$$J_w = A(\Delta P - \Delta\pi) = \frac{P_w^H}{L}(\Delta P - \Delta\pi) = \frac{K_w D_w}{L} \times \frac{V_w}{RT}(\Delta P - \Delta\pi) \quad (1.8)$$

where L is the membrane thickness, K_w is water solubility coefficient, and D_w is water diffusion coefficient. Similarly, diffusive salt permeability (P_s) is connected to B value using the following equation:

$$B = \frac{P_s}{L} \quad (1.9)$$

Using equation (1.6), equation (1.4) can be rewritten as

$$J_s = B\Delta C = \frac{P_s}{L}\Delta C = \frac{K_s D_s}{L}\Delta C \quad (1.10)$$

Besides, to clarify the relationships among *A* value, *B* value, and *R*, *R* is also expressed by the following equation: [8]

$$R = \left(1 + \frac{B}{A(\Delta P - \Delta\pi)}\right)^{-1} \times 100$$

$$R = \left(1 + \frac{P_s}{P_w} \times \frac{RT}{V_w} \times \frac{1}{(\Delta P - \Delta\pi)}\right)^{-1} \times 100$$

$$R = \left(1 + \frac{K_s}{K_w} \times \frac{D_s}{D_w} \times \frac{RT}{V_w} \times \frac{1}{(\Delta P - \Delta\pi)}\right)^{-1} \times 100 \quad (1.11)$$

From the equation (1.8) and (1.11), high K_w and D_w values with low K_s and D_s

values are required to achieve high J_w and R values.

For a variety of commercial RO membranes, there could be seen in a tradeoff relationship between J_w and R.[9–11] Membranes with higher A values often exhibit lower NaCl rejection and *vice versa*. According to the previous studies regarding the relationship between water permeability selectivity (P_w/P_s), and P_w, water solubility selectivity (K_w/K_s), and K_w, and water diffusivity selectivity (D_w/D_s) and D_w for various polymeric single membranes, D_w/D_s values range from less than 10^1 to more than 10^4, whereas the range of K_w/K_s values is from 10^0 to 10^1.[12] This indicates P_w/P_s (i.e. NaCl rejection) mainly derives from D_w and D_s values. Therefore, it seems important to achieve the selective enhancement of D_w value.

1.2.2 Water purification process via RO unit

The simplified schematic flow diagram for membrane-based water purification process is shown in Figure 1-2. Generally, there are two membrane separation steps (*i.e.* membrane pretreatment unit for removal of particles and other macromolecules followed by a RO unit for removal of salts). Disinfection of feed water to membrane pretreatment unit by chlorination is required to avoid biofilm growth on membrane surfaces, which significantly depresses membrane performance. However, RO membranes based on cross-linked aromatic polyamide cannot tolerate continuous exposure to water containing chlorine (as discussed later).[13] Thus, the additional dechlorination step is necessary before water is fed to a RO unit to prevent the degradation of RO membranes. After the membrane pretreatment, separating salt from the feed water is achieved by a RO unit. Among overall RO systems, semipermeable membranes play an important role in the reduction in the total cost for the purification, in spite of its low cost (8 % of the overall investment), since high permeable membranes with high rejection can reduce an operating pressure and hence require less energy.[4] Also, a reduction in an operating pressure leads to the reduction in the cost of pumps and flow devices. Moreover, membranes based on chlorine-tolerant polymer can reduce the cost of the additional dechlorination step.

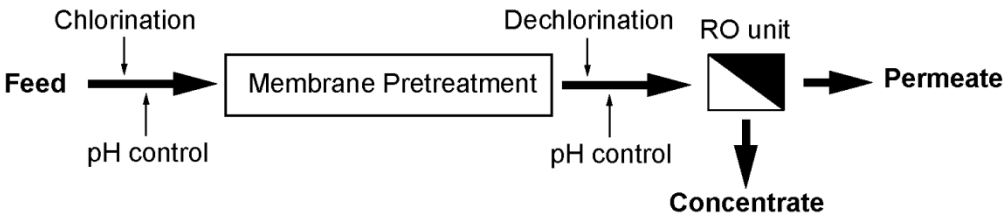

Figure 1-2 Simplified process flow diagram of water purification involving two applications such as pretreatment and salt removal via the RO unit.

1.2.3 Requirements for RO membranes

As discussed above, semipermeable membranes (RO membranes), as one of key materials, play an important role in RO process to reduce the total cost. The principal requirements for RO membrane is transportation of water from salty solution to fresh one with rejecting some salts. RO membranes should have some following requirements: 1) high water flux with high salt rejection, 2) high mechanical strength, 3) high chemical resistance (especially for chlorine), and 4) high fouling resistance. Especially, as discussed in 1.2.1, the control over D_w and D_s values is quite important to achieve high water flux with high NaCl rejection. han 0.5 nm must be established.

Table 1-1 summarizes Stokes radius (r_s) and hydrated radius (r_s) of the objective ions of RO process, indicating that the effective radii of the ions in the aqueous media are larger than water molecules due to the hydration.[14] Thus, the effective method to control over the pore radius with less than 0.5 nm must be established.

Table 1-1 Stokes and hydrated radii of the ions

ion	r_s [nm]	r_h [nm]
Na^+	0.184	0.358
K^+	0.125	0.331
Mg^{2+}	0.347	0.428
Ca^{2+}	0.310	0.412
Cl^-	0.121	0.332
Br^-	0.118	0.330
NO_3^-	0.129	0.335
SO_4^{2-}	0.230	0.379
H_2O	0.138	-

1.3 RO membrane materials

RO membranes for desalination are currently derived from two classes of polymers such as cellulose acetate (CA) and cross-linked aromatic polyamides (PA). Meanwhile, other materials, such as sulfonated poly(arylene ether sulfone), carbon nanotubes, and so for forth, for addressing the shortcoming of CA and PA and improving water transport properties have caught much attention. In this section, RO membranes based on CA, cross-linked aromatic PA, sulfonated poly(arylene ether sulfone), carbon nanotubes, and liquid crystals are described.

1.3.1 Cellulose acetate

CA (Figure 1-3), which is a green polymer synthesized by the acetyl substitution of cellulose known as one of the most common natural organic compounds, possesses unique advantages (such as relatively high hydrophilicity etc.).

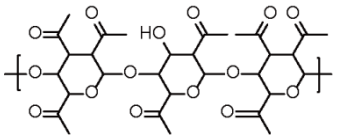

Figure 1-3 The chemical structure of CA.

After Reid and Breton reported in the late 1950s that symmetric membranes based on CA showed high NaCl rejection (98 %) but its water flux was less than 1.0×10^{-2} L m^{-2} h^{-1}, much attention has been paid to the improvement of CA membranes. In 1963, Loeb and Sourirajan has developed CA asymmetric membranes (water flux: 14.6 L m^{-2} h^{-1}, NaCl rejection: 99 %), fabricated by non-solvent induced phase separation method.[15] This development of the skinned asymmetric membranes was a major breakthrough in membrane technology so that many attempts to enhance water and salt transport

properties of CA asymmetric membranes were carried out. Cellulose triacetate (CTA) membrane was designed for increasing its stability in a wider range of temperature and pH as well as higher biofouling resistance compared to CA.[16] HOLLOSEP HM10255®, which is based on CTA and commercialized by TOYOBO as a seawater RO membrane module utilized especially in Middle East, can produce fresh water for 4600 hrs without any chemical cleaning.[17] However, the compaction caused by the operating pressure (30 bar) led to the severe loss of water flux. Although HB 10255® commercialized by TOYOBO are well known as the state-of-art CA asymmetric membranes and utilized in the Fukuoka seawater desalination plant that produces fresh water 50000 m^3 day^{-1}, CA membranes are susceptible to the microbiological attack and are limited to operate in a narrow pH range (3.5 to 6.5) due to the hydrolysis of the acetate groups, in addition to the compaction under high temperature and pressure.[18,19] Therefore, more and more CA membranes has been replaced to the thin film composite membrane.

1.3.2 Cross-linked aromatic polyamides

Since thin film composite membrane that have a thin active barrier layer (thickness: less than 100 nm) synthesized by interfacial polymerization on a porous polysulfone support layer (thickness: about 50 nm) was developed by Caddot in early 1972, much attention has been paid to the composite membranes.[20] The schematic diagram of thin film composite membrane is shown in Figure 1-4. The FT-30®, which was prepared by the reaction between *m*-phenylenediamine and trimesoyl chloride and commercialized membrane by Dow Water and Process Solution in 1981, has dominated the market for desalination application for about 30 years.[1] Interfacial polymerization produces a very specific surface characteristic, which has been described as ‘‘ridge and

valley'' structure. According to the previous reports, this ''ridge and valley'' structure increases the effective membrane surface area for water transport and leads to the increase in water flux.[21]

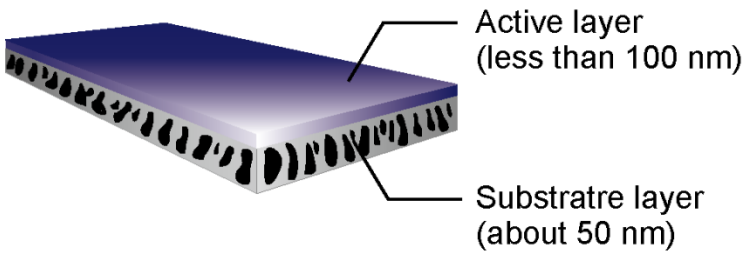

Figure 1-4 A schematic diagram of thin film composite membrane.

Many previous studies concerning the relationship between the molecular structures of cross-linked PAs and water transport properties revealed that the reaction between *m*-phenylenediamine and trimesoyl chloride (Figure 1-5) produces the highest water flux (40 - 60 L m^{-2} h^{-1}) and NaCl rejection (99.6 - 99.8 %).[22–24]

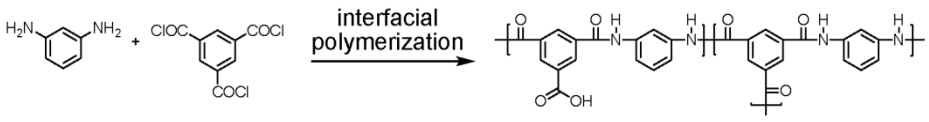

Figure 1-5 Cross-linked aromatic polyamide via interfacial polymerization

PA membranes significantly suffer from performance degradation under the exposure to chlorine, resulted in the additional use of expensive dechlorination and rechlorination steps. The proposed mechanism aromatic polyamide chlorination mechanism by Glator

et al. is shown in Figure 1-6.[25] As has been discussed by Kawaguchi and Tamura, the tertiary amide linkage not possessing a hydrogen atom showed high chlorine resistance, since the secondary amide linkage is the most sensitive moiety toward chlorine attack.[26]

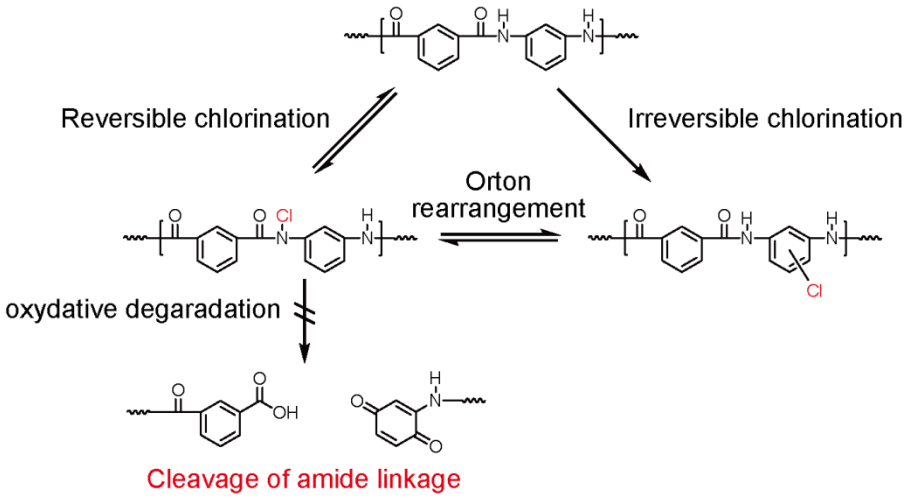

Figure 1-6 Proposal mechanism of chlorination of aromatic polyamide.

Cross-linked polypiperazineamide with tertiary amide linkages (as shown in Figure 1-7) are expected to be chlorine tolerance materials.[27] However, the polypiperazineamide composite membrane exhibited high water flux (71 L m^{-2} h^{-1}) but low NaCl rejection (50 %).

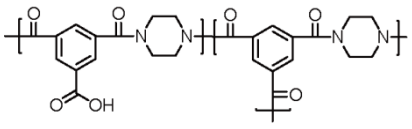

Figure 1-7 The chemical structure of cross-linked polypiperazineamide.

1.3.3 Sulfonated polymers

Without chlorine sensitive amide linkages, poly(arylene ether sulfones) shows excellent thermal and chemical stabilities as well as chlorine resistance.[28] Therefore, poly(arylene ether sulfones) are widely used as porous substrate in thin film composite membranes and considered to become alternative materials to cross-linked aromatic polyamides. Although poly(arylene ether sulfones) are highly hydrophobic, they may be sulfonated. The post-sulfonation, which was usually achieved by the aromatic electrophilic substitution reaction to conventional engineering plastic, was the most common and accessible approach to obtain sulfonated poly(arylene ether sulfones). However, concerned matters, such as the repeatability of post-sulfonation, the limited variety of the polymer structure that could be available for post-sulfonation, and the limited number of sulfonic acid groups that could be introduced into a polymer, impeded the development of sulfonated polymer in the water treatment fields.[29]

In contrast, the preparation of sulfonated aromatic polymers from sulfonated monomers was then developed. McGrath et al. reported the synthesis of 3,3'-disulfonated-4,4'-dichlorodiphenylsulfone, which allowed the preparation of sulfonated aromatic polymers with a defined polymer structure.[30] Using this monomer, they also synthesized sulfonated poly(ether sulfone)s (BPS-X) by the aromatic nucleophilic substitution reaction (Figure 1-8). This not only solved the disadvantages of post-sulfonation but also allowed the synthesis of sulfonated copolymers with any desired compositions between non-sulfonated and sulfonated monommers.

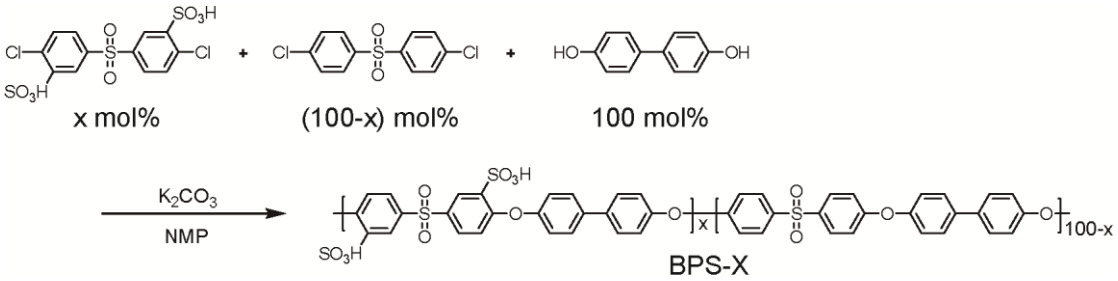

Figure 1-8 Preparation of sulfonated poly(ether sulfone)s from a sulfonated monomer.

McGrath et al. also strenuously studied the water and salt transport properties of BPS-X membranes.[31–33] Because of the absence of the amide linkages, BPS-X exhibited high chlorine tolerance (over 40 h at 500 ppm chlorine). Although BPS-X exhibited high NaCl rejection (99.2 %), the water permeability of BPS-X symmetric membrane (0.03 L μm m^{-2} h^{-1} bar^{-1}) was quite low even if the degree of sulfonation and the form of the counter cation to the sulfonate groups was changed. Furthermore, they revealed that the blends of BPS-X with polyethylene glycol by strong ion-dipole interactions between potassium ions of sulfonate groups and oxyethylene groups in polyethylene glycol led to the plasticization, resulted in an increase in free volume and water uptake.[34] Consequently, the increase in water permeability (0.055 L μm m^{-2} h^{-1} bar^{-1}) was achieved. Kim and coworkers also studied the water and salt transport properties of the membranes based on end-group cross-linked sulfonated and fluorinated poly(arylene ether) (ESF-BP) as shown in Figure 1-9.[35] Although the water permeability of ESF-BP were low (0.6 L μm m^{-2} h^{-1} bar^{-1}), ESF-BP exhibited excellent chlorine tolerance (over 30 days at 4000 ppm chlorine) in addition to high NaCl rejection (98.4 %). Though many efforts to improve water and salt transport properties of ESF-BP have been conducted, the water transport properties was still not sufficient for practical use.

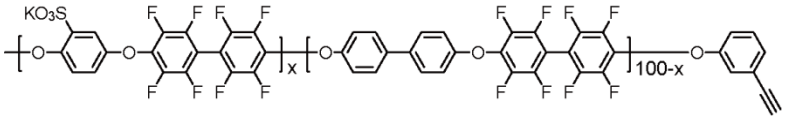

Figure 1-9 Chemical structure of end-group cross-linked sulfonated and fluorinated poly(arylene ether) (ESF-BP).

1.3.4 Carbon nanotubes

Carbon nanotubes (CNTs), 1D-nanomaterials with very high aspect ratio, have gathered much attention of many researchers due to their high water permeability ascribed to the unique hydrophobic character of the membrane surfaces and interior wall, antibiofouling property, and mechanical stability. Especially, the water permeability of the aligned CNTs is theoretically estimated to be more than 1000 L m^{-2} h^{-1} bar^{-1} and the chemical modification of the ends of CNTs to charged or bulky groups can prevent NaCl passage due to the electrostatic interaction and steric hindrance.[36,37] Although there are no reports for the preparation of the membrane with aligned CNTs having large membrane area mainly due to the difficulties of incorporating the aligned CNTs into polymer matrix, membrane having dispersed CNTs as fillers in the polymer matrix have been reported. Lee and coworkers prepared the thin film composite membrane with cross-linked PA active layer incorporating CNTs funtionalized by a sulfuric acid and nitric acid mixture, which high showed water flux (40 L m^{-2} h^{-1}) and NaCl rejection (90 %).[38]

According to the report by Endo and co-workers, the cross-linked PA active layer incorporating 15.5 wt% of multi-walled CNTs enhanced chlorine resistance due to the reduction of chlorine within the matrix and the physical cross-linking effect of CNTs.[39] Their membrane exhibited high water flux (62.5 L m^{-2} h^{-1} bar^{-1}) with high NaCl

rejection (99.3 %), indicating that composite membrane with CNTs can become a promising candidate for tailor-made membranes. However, these experimental results have been lower compared to the theoretically estimated values, implying that more work is necessary for the development of efficient preparation method to align arrays of CNTs, with subnanometer diameters and tip-functionalization of charged groups.

1.3.5 Liquid crystal

It seems difficult to form the cross-linked PA layers with well-defined nanometer-scaled pores due to the interfacial polymerization, the molecular self-organization process is expected as a promising approach to prepare the membrane with ordered nanostructures and to achieve high performance water treatment. Cross-linked ionic liquid is expected to afford well-ordered nanostructures. Gin and co-workers reported that membranes based on cross-linked lyotropic liquid crystals (as shown in Figure 1-10a) as an active layer, which shows mesophase in water and has an effective pore size of 0.75 nm, exhibited high NaCl rejection (95 %) but low water flux (0.06 L m^{-2} h^{-1}).[40] Henmi et al. also demonstrated using the cross-linkable liquid crystal (as shown in Figure 1-10b) that the thin film composite membrane with bicontinuous cubic liquid crystal nanostructure as an active layer shows high water flux (33 L m^{-2} h^{-1}) but low NaCl rejection (60 %).[41] However, water transport properties of these membranes were considerably low for practical use.

Figure 1-10 Chemical structure of liquid crystal molecules.

1.4 Purpose of this work

At present, RO desalination systems based on the cross-linked PA composite membrane have been widely used. However, it is very difficult to characterize the fundamental transport properties of the PA active layer itself, because the PA active layer is not self-standing and its thickness is not well-defined. As a result, the influence of chemical and molecular aggregation structures of polymer on fundamental transport properties of water and salt through the active layer still remains unclear, frustrating the establishment of a guide for material design of semipermeable membranes based on the systematic investigation of structure-property relationship, which have been already accomplished in gas separation membranes.[42–44] In addition, transport properties of sulfonated poly(arylene ether sulfone)s and cross-linked liquid crystal as an alternative materials is not efficient for the practical use. The purposes of this work are to investigate the polymer structure-transport property relationship by using freestanding thin membranes and to develop novel polymeric materials which can be used as alternative active layers for cross-linked PA.

We focused on aromatic PAs and polybenzimidazoles (PBIs) known as engineering plastics for membrane materials due to their high mechanical strength. These materials are about 2.0 μm thick to increase water flux as high as possible. In this dissertation, the development of novel reverse osmosis membrane materials for water treatment is described in the following chapters.

The general introduction regarding the background and the purposes of this study is described in chapter 1.

In chapter 2, ‘‘Preparation and Structure-Property Relationship of Wholly

Aromatic Polyamide Membranes'', the semipermeable membranes based on the various wholly aromatic PAs are prepared through spin-coating or non-solvent induced phase separation methods to reveal the fundamental structure-property relationship and to identify the determining factors toward the enhancement of transport properties. It becomes clear to suppress the polymer aggregation for an improvement of transport properties.

In chapter 3, ''Effect of *N*-Methyl Amide Linkage on Hydrogen Bonding Behavior and Water Transport Properties of Random Aromatic Copolyamide Membranes'', the influence of the tertiary *N*-methylated amide linkage on the transport properties is studied. The suppression of the hydrogen bonding and the change in the conformational preference increase free volume and cosequently lead to an increase in water flux while lowering NaCl rejection due to an increase in water and NaCl diffusion coefficients.

In chapter 4, ''Effect of Cross-linking Reaction of *N*-Substituted Polybenzimidazole Membranes on Water Transport Properties'', the effect of the cross-linking of *N*-substituted PBI on the polymer aggregation behavior and transport properties is investigated. Cross-linked *N*-butyl sulfonated PBI membrane shows higher water permeability with relatively low NaCl permeability compared to various membrane materials, since cross-linking reaction with divinyl sulfone induces the change in the pore radius distribution from monomodal curve to bimodal one and lead to a selective enhancement in water diffusion coefficient.

In chapter 5, ''Solution and Solid-state Structures of Dynamic Covalent Aromatic Polyamides: Effect of Thermal Reorganization Behaviors'', novel main-chain

type dynamic covalent PA and random coPA are synthesized to investigate the effect of the radical crossover reaction on the solution and solid-state. A rise in the membrane fabrication temperature leads to a suppression of the interaction between the polymer chains, a formation of a clear phase separated structure, and an increase in the number of carboxylic acids involved in the surface reorganization induced by water molecule.

Finally, this study on novel semipermeable membranes for water treatment is concluded in chapter 6.

1.5 References

(1) Geise, G. M.; Lee, H.; Miller, D. J.; Freeman, B. D.; Mcgrath, J. E.; Paul, D. R. *J. Polym. Sci. Part B Polym. Phys.* **2010**, *48*, 1685–1718.

(2) Elimelech, M.; Phillip, W. A. *Science* **2011**, *333*, 712–718.

(3) Anderson, M. a.; Cudero, A. L.; Palma, J. *Electrochim. Acta* **2010**, *55*, 3845–3856.

(4) Semiat, R. *Environ. Sci. Technol.* **2008**, *42*, 8193–8201.

(5) Shannon, M. a; Bohn, P. W.; Elimelech, M.; Georgiadis, J. G.; Mariñas, B. J.; Mayes, A. M. *Nature* **2008**, *452*, 301–310.

(6) Fritzmann, C.; Löwenberg, J.; Wintgens, T.; Melin, T. *Desalination* **2007**, *216*, 1–76.

(7) Wijmans, J. G.; Baker, R. W. *J. Memb. Sci.* **1995**, *107*, 1–21.

(8) Cath, T.; Childress, a; Elimelech, M. *J. Memb. Sci.* **2006**, *281*, 70–87.

(9) http://www.dow.com/liquidseps/prod/prd_film.htm.

(10) http://www.gewater.com/.

(11) http://www.membranes.com/.

(12) Geise, G. M.; Park, H. B.; Sagle, A. C.; Freeman, B. D.; McGrath, J. E. *J. Memb. Sci.* **2011**, *369*, 130–138.

(13) Cran, M. J.; Bigger, S. W.; Gray, S. R. *Desalination* **2011**, *283*, 58–63.

(14) Nightingale, E. R. *J. Phys. Chem.* **1959**, *63*, 1381–1387.

(15) Loeb, S.; Sourirajan, S. *Adv. Chem. Ser.* **1968**, *38*, 117–132.

(16) Lee, K. P.; Arnot, T. C.; Mattia, D. *J. Memb. Sci.* **2011**, *370*, 1–22.

(17) Munoz, A.; Nunez, A.; Nishida, M. *Desalination* **1999**, *125*, 55–64.

(18) Kumano, A.; Fujiware, N. *Advaned Membr. Technol. Appl.* **2008**, 39.

(19) Reid, C. E.; Breton, E. J. *J. Apply. Poly. Sci.* **1959**, *1*, 133–143.

(20) Cadotte, J. E.; Petersen, R. J.; Larson, R. E.; Erickson, E. E. *Desalination* **1980**, *32*, 25–31.

(21) Kwak, S. Y.; Jung, S. G.; Yoon, Y. S.; Ihm, D. W. *J. Polym. Sci. Part B Polym. Phys.* **1999**, *37*, 1429–1440.

(22) Kim, J. H.; Moon, E. J.; Kim, C. K. *J. Memb. Sci.* **2003**, *216*, 107–120.

(23) Yong, Z.; Sanchuan, Y.; Meihong, L.; Congjie, G. *J. Memb. Sci.* **2006**, *270*, 162–168.

(24) Petersen, R. J. *J. Memb. Sci.* **1993**, *83*, 81–150.

(25) Glater, J.; Zachariah, M. R. *ACS Symp. Ser.* **1985**, *281*, 345–358.

(26) Kawaguchi, T.; Tamura, H. *J. Apply. Poly. Sci.* **1984**, *29*, 3359–3367.

(27) Eriksson, P. *J. Memb. Sci.* **1988**, *36*, 297–313.

(28) Parekh, B. S.; Parise, P. L.; Swiniarski, E. J.; Corporation, M. *Desalination* **1987**, *64*, 285–304.

(29) Hickner, M. a. *Mater. Today* **2010**, *13*, 34–41.

(30) Harrison, W. L.; Wang, F.; Mecham, J. B.; Bhanu, V. a.; Hill, M.; Kim, Y. S.; McGrath, J. E. *J. Polym. Sci. Part A Polym. Chem.* **2003**, *41*, 2264–2276.

(31) Xie, W.; Ju, H.; Geise, G. M.; Freeman, B. D.; Mardel, J. I.; Hill, A. J.; McGrath, J. E. *Macromolecules* **2011**, *44*, 4428–4438.

(32) Xie, W.; Cook, J.; Park, H. B.; Freeman, B. D.; Lee, C. H.; McGrath, J. E. *Polymer* **2011**, *52*, 2032–2043.

(33) Park, H. B.; Freeman, B. D.; Zhang, Z. B.; Sankir, M.; McGrath, J. E. *Angew. Chem. Int. Ed. Engl.* **2008**, *47*, 6019–6024.

(34) Lee, C. H.; VanHouten, D.; Lane, O.; McGrath, J. E.; Hou, J.; Madsen, L. a.; Spano, J.; Wi, S.; Cook, J.; Xie, W.; Oh, H. J.; Geise, G. M.; Freeman, B. D. *Chem. Mater.* **2011**, *23*, 1039–1049.

(35) Kim, Y. J.; Lee, K. S.; Jeong, M. H.; Lee, J. S. *J. Memb. Sci.* **2011**, *378*, 512–519.

(36) Corry, B. *Energy Environ. Sci.* **2011**, *4*, 751.

(37) Shi, Z.; Zhang, W.; Zhang, F.; Liu, X.; Wang, D.; Jin, J.; Jiang, L. *Adv. Mater.* **2013**, *25*, 2422–2427.

(38) Kim, H. J.; Choi, K.; Baek, Y.; Kim, D. G.; Shim, J.; Yoon, J.; Lee, J. C. *ACS Appl. Mater. Interfaces* **2014**, *6*, 2819–2829.

(39) Endo, M.; Takeuchi, K.; Noguchi, T.; Asano, Y.; Kim, Y. A.; Hayashi, T.; Ueki, H.; Iinou, S. *Ind. Eng. Chem. Res.* **2010**, *49*, 9798–9802.

(40) Zhou, M.; Nemade, P. R.; Lu, X.; Zeng, X.; Hatakeyama, E. S.; Noble, R. D.; Gin, D. L. *J. Am. Chem. Soc.* **2007**, *129*, 9574–9575.

(41) Henmi, M.; Nakatsuji, K.; Ichikawa, T.; Tomioka, H.; Sakamoto, T.; Yoshio, M.; Kato, T. *Adv. Mater.* **2012**, *24*, 2238–2241.

(42) Koros, W. J.; Fleming, G. K. *J. Memb. Sci.* **1993**, *83*, 1–80.

(43) Freeman, B. D.; Carolina, N. *Macromolecules* **1999**, *32*, 375–380.

(44) Robeson, L. M.; Freeman, B. D.; Paul, D. R.; Rowe, B. W. *J. Memb. Sci.* **2009**, *341*, 178–185.

Chapter 2

Preparation and Structure-Property Relationship of Wholly Aromatic Polyamide Membranes

2.1 Introduction

Polymeric semipermeable membranes for reverse osmosis (RO) have been important materials for water treatment from the standpoint of environment and energy.[1–5] In a RO process, a significant amount of energy is required since a high hydraulic pressure to overcome the osmotic pressure difference is applied as the driving force of water permeation. Currently, cross-linked polyamides (PA) are commonly used as active layers of commercial RO membranes.[6] However, the cross-linked PA active layer prepared by interfacial polymerization on the surface of the supporting layer cannot be used without a supporting layer, since this layer with around 50 nm thickness has a very low mechanical strength. Thus, the fundamental transport properties of the cross-linked PA could not be directly measured, frustrating the development of the systematic elucidation of the structure and property relationship.

In this chapter, we have prepared and characterized novel ultrathin

single-component wholly-aromatic PA membranes with about 2.0 μm thickness to investigate the structure-property relationship. First, the primary structures of PAs were designed by changing the molecular structures in monomer repeating units, *e.g.* by introducing hydrophilic groups into polymer backbone. Second, the effect of non-solvent induced phase separation method on the transport properties of ultrathin PA membranes was investigated for the improvement in the water transport properties.

2.2 Result and discussion

2.2.1 Synthesis and characterization

A series of polyamides (**PA1**, **PA2**, **PA3**, and **PA4**) and random copolyamides (**PA2-xx**, where xx indicates the feed molar ratio of the hydrophilic 3,5-diaminobenzoic acid among the diamine monomers) were synthesized by low temperature polycondensation reaction of the corresponding diamines and isophthaloyl chloride as shown in **Figure 2-1**. The chemical compositions of the random copolyamides (**PA2-xx**) were precisely controlled by varying the feed molar ratio of 3,5-diaminobenzoic acid among the diamine comonomers and confirmed by their ^{1}H NMR spectra. **Figure 2-2** representatively shows the ^{1}H NMR spectrum of **PA2-20**. The ratio of integrals of the aromatic and amine protons of the 3,5-diaminobenzoic acid unit and the 4,4'-diaminodiphenyl ether unit was in accordance with the target chemical structure. The inherent viscosity η_{inh} measurement of the polyamides was carried out at a concentration of 0.5 g dL^{-1} in NMP at 30°C. The η_{inh} values listed in **Table 2-1** were consistent with high molecular weight polymers.

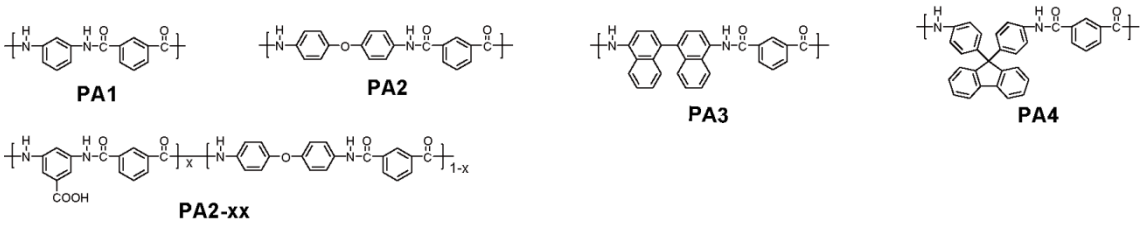

Figure 2-1 Chemical structure of **PA1**, **PA2**, **PA3**, **PA4**, and **PA2-xx**

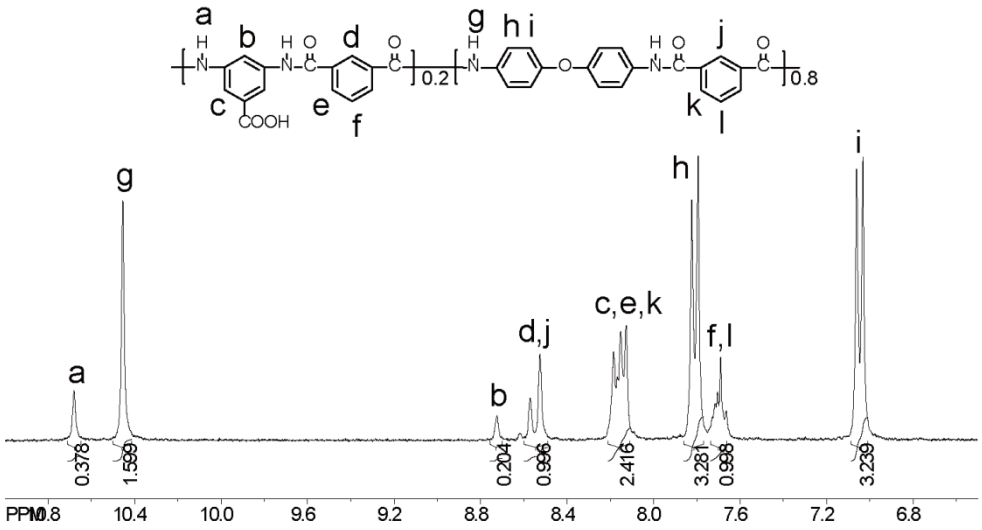

Figure 2-2 ^{1}H NMR spectrum of **PA2-20**.

Table 2-1 Inherent viscosities of PAs

		PA1	PA2	PA3	PA4	PA2-20	PA2-50	PA2-80	PA2-100
η_{inh} [a]	[g dL^{-1}]	1.32	1.65	1.04	1.48	0.94	1.26	0.84	1.56

[a]Evaluated at 30 °C in NMP at a concentration of 0.5 g dL^{-1}.

2.2.2 Water and NaCl transport properties

2.2.2.1 PA1, PA2, PA3, PA4, and PA2-xx

To evaluate the influence of the chemical structure of the polyamide membrane on semipermeability, the water transport properties were examined using the instruments in the RO mode at an operating pressure of 7.5 bar. The PA membranes (**PA1**, **PA2**, **PA3**, and **PA4**) with about 2 μm thickness were successfully prepared by a normal spin-coating method. In general, the increase in the free volume of the membranes leads to an enhancement of water permeability (A value) and salt permeability (B value).[7] **Table 2-2** shows the water permeation properties of these membranes. Unfortunately, **PA1**, **PA2**, **PA3**, and **PA4** did not show any water permeation phenomena. Therefore, it was obvious that the introduction of a flexible ether, bulky binaphtyl, or fluorene units with large free volume in the ultrathin membranes did not contribute to the water permeation behavior.

As shown in **Table 2-2**, the water permeation phenomenon was somewhat confirmed by introducing a carboxylic acid group into the polymer backbone. On the basis of the solution-diffusion model, water sorption coefficient (K_w), water diffusion coefficient (D_w), salt sorption coefficient (K_s), and salt diffusion coefficient (D_s) was calculated.[8] The introduction of hydrophilic group led to the increase in K_w value, water permeability (A), and water flux (J_w). Also, it was found that D_w value was not affected by the hydrophilicity. Meanwhile, K_s value was also slightly increased with maintaining D_s value by the introduction of the hydrophilic group. These observations imply that the introduction of the carboxylic acid groups selectively increase the water and salt sorption coefficients. Thus, the hydrophilicity in the membranes was an

important factor to enhance the water transport properties of the ultrathin membranes. This result is consistent with the previous reports, which described that water permeability of the membrane is proportional to the ratio of the hydrophilic unit in the polymer chains.[7,9–11] However, since the significant increase in K_w values by the increasing the ratio of the 3,5-diaminobenzoic acid unit per repeating unit could not be seen, A value of **PA2-xx** was still low and slightly improved. Therefore, it seems difficult to improve J_w value and salt rejection (R) only by modifying the primary structure of the PAs.

Table 2-2 Water transport properties of various PA membranes

Polymer	J_w[a] [L m^{-2} h^{-1}]	R[a] [%]	A[a] [L μm m^{-2} h^{-1} bar^{-1}]	B[a] [cm^2 s^{-1}]	K_w[b]	D_w[b] [cm^2 s^{-1}]	K_s[c]	D_s[c] [cm^2 s^{-1}]
PA1	ND	ND	ND	ND	ND	ND	ND	ND
PA2	ND	ND	ND	ND	ND	ND	ND	ND
PA3	ND	ND	ND	ND	ND	ND	ND	ND
PA4	ND	ND	ND	ND	ND	ND	ND	ND
PA2-20	0.50	24	0.141	0.88×10^{-10}	0.076	7.091×10^{-6}	0.055	1.61×10^{-9}
PA2-50	0.54	33	0.153	0.61×10^{-10}	0.079	7.438×10^{-6}	0.055	1.10×10^{-9}
PA2-80	1.04	21	0.294	2.18×10^{-10}	0.129	8.704×10^{-6}	0.103	2.10×10^{-9}
PA2-100	0.92	23	0.259	1.70×10^{-10}	0.171	5.783×10^{-6}	0.143	1.20×10^{-9}

[a]Measured at 25 °C using cross-flow filtration (ΔP =7.5 bar ; NaCl concentration = 500 mg L^{-1}) . [b]Estimated from water uptake and dry density. [c]Measured by NaCl desorption measurement.

2.2.2.2 PA2-20-additive

In order to enhance the water flux and salt rejection of ultrathin semipermeable membranes, non-solvent induced phase separation method has been used so far since the discovery of high flux cellulose acetate membranes by Loeb and Sourirajan. This method includes the addition of aqueous additives to the casting solution to provide a semipermeability by generating pores induced by phase inversion. Ikeda et al. also reported a similar approach based on aromatic PAs containing carboxylic groups, which showed higher water flux and salt rejection than that of the PAs without carboxylic groups.[12] **PA2-20** was selected as a representative material for the membrane preparation from the polymer solution containing aqueous additives, since Kuzumoto et al. reported that there was no clear relationship between the ratio of the carboxylic acid group in the polymer and the RO performance.[38] The composition of the casting solution was **PA2-20** (6.5 wt%), NMP (58.1 wt%), $MgCl_2$ (4.8 wt%), H_2O (17.7 wt%), and ethylene glycol (12.9 wt%). $MgCl_2$ is coordinated to the amide linkage and reduce the polymer interactions, which suppresses the aggregation of polymer chains and consequently increases the free volume in the polymer matrix. H_2O and ethylene glycol may be absorbed into the membrane through such free volume and functioned as templates for the formation of pores in the membranes.

The transport properties of **PA2-20** and **PA2-20-additives** were evaluated using the instruments in the RO mode at applied pressure 7.5 bar, and the results are summarized in Table 2-3. The diffusion and sorption coefficient are not evaluated, since **PA2-20-additive** is not dense but relatively porous membrane so that solution-diffusion mechanism cannot be applied (see section 0). In spite of using exactly the same polymer, there is a significant difference in the J_w and A values between them. In contrast, the B

value of **PA2-20-additive** was almost the same as that of **PA2-20**. Notably, **PA2-20-additive** showed more than a 10 times higher water flux (0.50 L m^{-2} h^{-1}) than **PA2-20** (14.2 L m^{-2} h^{-1}) along with a slightly improved salt rejection. These results indicated that this fabrication method for the membrane preparation significantly affects the water permeability of the membranes.

Table 2-3 Water transport properties

Polymer	$J_w{}^a$ [L m^{-2} h^{-1}]	R^a [%]	A^a [L μm m^{-2} h^{-1} bar^{-1}]	B^a [cm^2 s^{-1}]
PA2-20	0.50	24	0.141	0.0088×10^{-8}
PA2-20-additive	14.2	35	60.05	0.146×10^{-8}

[a]Measured at 25 °C using cross-flow filtration (ΔP =7.5 bar ; NaCl concentration = 50 0 mg L^{-1}) . [b]Estimated from water uptake and dry density.

2.2.3 Membrane structure

Apparently, the difference in the transport property between **PA2-20** and **PA2-20-additive** is owing to the modification of the membrane fabrication process. In this section, membrane structure was characterized to investigate the factors required for the improvement in the water transport properties of the ultrathin semipermeable membranes.

2.2.3.1 ATR-FTIR measurements

To analyze the degree of the hydrogen bonding between the amide linkages in the membrane, ATR-FTIR spectra of **PA2-20** and **PA2-20-additive** were measured. As shown in **Figure 2-3**(a), a peak at 1653 cm^{-1} indicates the C=O stretching of the secondary amide group for both membranes. Both membranes showed these two peaks at the same wavenumbers. However, the peak from the C=O stretching was shifted to a higher wavenumber (1667 cm^{-1}) in the difference spectra of **PA2-20** and **PA2-20-additive** as shown in **Figure 2-3**(b), indicating that hydrogen bonds between the amide linkages became weaker. This would be due to the aqueous additives, which suppress the aggregation of polymer chains by the formation of complex between carbonyl group and Mg^{2+}.

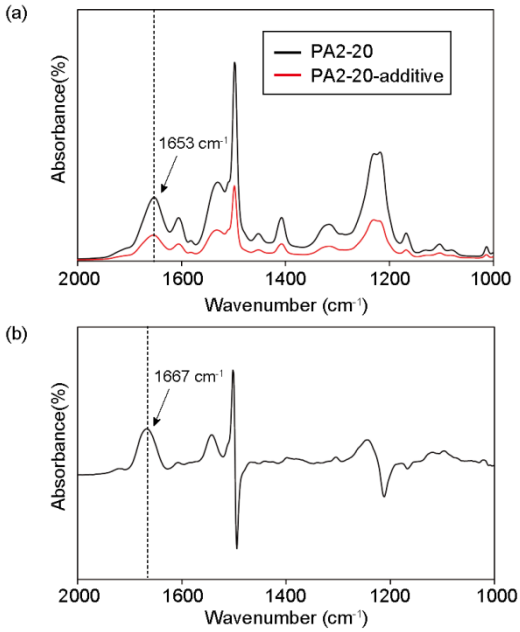

Figure 2-3 (a) ATR-FTIR spectra of **PA2-20** and **PA2-20-additive**, and (b) difference spectra of **PA2-20** and **PA2-20-additive**.

2.2.3.2 Solid-state ^{13}C CPMAS NMR measurements

Subsequently, solid-state ^{13}C CPMAS NMR measurements were carried out to characterize the mobility of polymer chains in the membrane, since the change in the hydrogen bonding behavior caused a change in the flexibility of the polymer chains.[13] It is well known that when the molecular mobility of the polymer is high, the peak intensities of the CPMAS spectra become strong.[7,13] The peak assignments are shown in **Figure 2-4**, where the intensities of the peaks were normalized at D. It can be seen that the intensities of the peaks (assigned to A, A', B and C) for **PA2-20-additive**, become stronger than those of **PA2-20**. The increase in these intensities indicates that the molecular mobility of **PA2-20-additive** is higher than that of **PA2-20** due to the suppression of the polymer interactions in the case of **PA2-20-additive**, which probably increases free volume and promotes the absorption of water and ethylene glycol via the coordination of Mg^{2+} to the amide linkage.[7] This result agrees with the ATR FT-IR spectra.

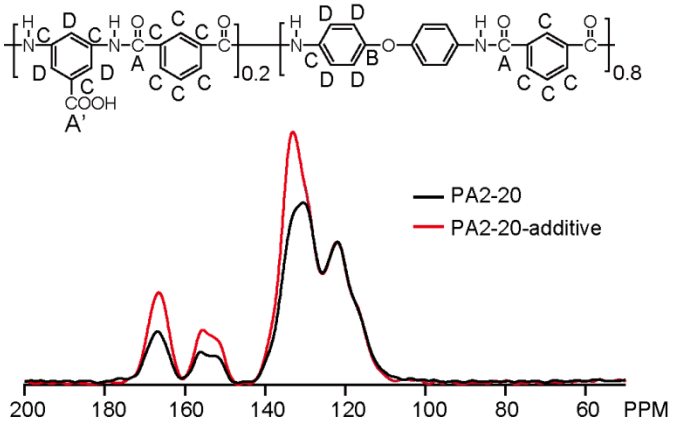

Figure 2-4 ^{13}C CPMAS NMR spectra of **PA2-20** and **PA2-20-additive**.

2.2.4 The state of water in the membrane

There are at least three states of water associated with hydrophilic region in a polymer, such as *non-freezing bound water*, *freezable bound water* and *free water*.[14] Thermal properties based on DSC allowed us to evaluate the state of water in polymer membranes. *Non-freezing bound water*, which is strongly bound with the polymer, does not show a melting endothermic peak by DSC. Broad melting peak at around 0°C is appeared in the case of *freezable bound water* weakly associated with the polymer. *Free water*, not intimately bound to polymer, displays a sharp melting peak at 0°C. McGrath et al. reported that the amount of *freezable bound water* and *free water* in the cross-linked sulfonated poly(ether sulfone) membrane increased when cross-linking reaction time is short. After the cross-linking reaction, mean pore size and pore size distribution decreased. In other words, an endothermic peak from *freezable bound water* is appeared when the pore formed. In **PA2-20-additive**, both the broad endothermic peak from *freezable bound water* around -0.2°C and the sharp endothermic peak from *free water* around 0.8°C were observed in Figure 6. On the other hand, **PA2-20** showed only an endothermic peak from *free water*. These results suggest that **PA2-20-additive** contained relatively larger pores enough to bind water than **PA2-20**. In addition, the endothermic peaks of *free water* were normalized to evaluate the water absorbability. **PA2-20-additive** showed a higher endothermic energy of 44.5 cal/g than **PA2-20** (35.5 cal/g), therefore the amount of water absorbed by **PA2-20-additive** is greater than that of PA2-20. These results support the superior water flux of **PA2-20-additive** compared to **PA2-20**. Moreover, Kesting et al. investigated the relationship between *freezable bound water* and water/salt transport property using a cellulose acetate asymmetric membrane.[27] Their studies revealed that water molecules can permeate the membrane by its

participation of the water molecules with *freezable bound water* in the membrane, which is strongly interacted with the active site, and that salt has a difficulty in permeating due to its inability to ligand with *freezable bound water*. From these results, it is probable that the increase in the *A* value while maintaining almost the same *B* value is resulted from the existence of *freezable bound water* in **PA2-20-additive** possessing pores to bind the water.

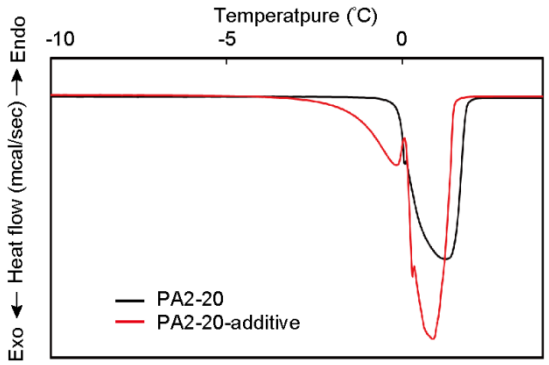

Figure 2-5 DSC thermograms of **PA2-20** and **PA2-20-additive**.

2.2.5 Membrane morphology

Finally, the cross-sectional microstructure and surface morphology of **PA2-20-additive** were observed by scanning electron microscopy (SEM). Figure 2-6 shows the SEM images of **PA2-20-additive**. Obviously, it is confirmed that the sponge-like pores were formed at the cross-section of membrane. Many pores with less than 50 nm diameter could be seen at the membrane surface, which is consistent with DSC analysis.

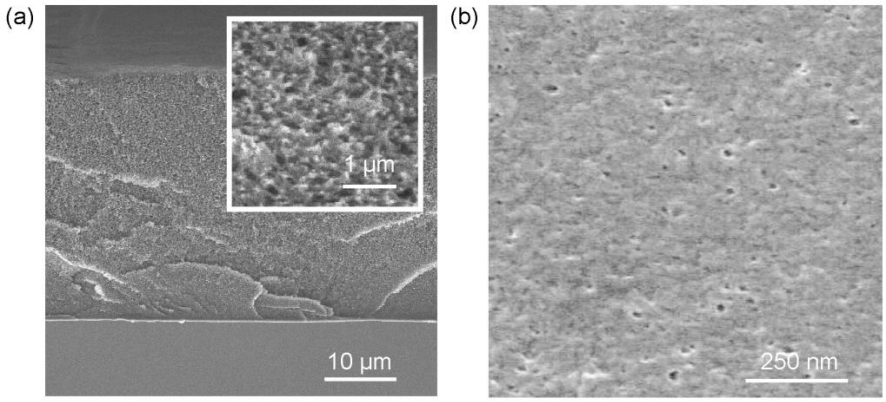

Figure 2-6 (a) Cross-section and (b) surface SEM images of **PA2-20-additive**.

2.3 Conclusions

Ultrathin semipermeable membranes based on various aromatic PAs were prepared and characterized. Although the effect of polymer backbone on water transport properties could not be observed, water permeability was slightly improved by the introduction of the hydrophilic carboxylic acid groups due to the increase in water sorption coefficient. Also, non-solvent induced phase separation method has been used for improving the performance of ultrathin self-standing wholly aromatic polyamide membranes. Water permeability was significantly improved using a membrane prepared from the casting solution containing aqueous additives with slightly increasing NaCl rejection. This could be resulted from the formation of pores filled with *freezable bound water* as confirmed by DSC analysis and SEM observation. Also, ATR-FTIR and ^{13}C CPMAS NMR spectroscopy demonstrated that the aggregation of polymer chains due to the hydrogen bonds among the amide linkages was suppressed probably due to the coordination of the aqueous additives to the amide linkage. Therefore, this clearly indicates that the suppression of the polymer/polymer interaction is one of the requirements for improving water transport properties of the ultrathin membranes.

2.4 Experimental

2.4.1 Materials

m-Phenylenediamine, 4,4'-diaminodiphenyl ether, 9,9'-bis(4-aminophenyl)-fluorene, isophthaloyl chloride, and 3,5-diaminobenzoic acid were purchased from TCI, Japan and purified by recrystallization before use. *N*-Methylpyrrolidone (NMP) purchased from Wako Pure Chemical Industries, Japan was dried over calcium hydride and distilled under nitrogen. 1,1'-Diamino-2,2'-binaphthyl was prepared according to previous report.[15]

2.4.2 Synthesis of polyamides having various repeating units

Various polyamides (**PA1**, **PA2**, **PA3** and **PA4**), which have different repeating units, were synthesized by the low temperature polycondensation reaction, between diamines including *m*-phenylenediamine, 4,4'-diaminodiphenyl ether, 1,1'-diamino-2,2'-binaphthyl, or 9,9'-bis(4-aminophenyl)fluorene and isophthaloyl chloride, which is described in detail for the case of polymer **PA1** as a typical procedure. To a two-necked flask, *m*-phenylenediamine (1.16 g, 10.8 mmol) and NMP (13.0 mL) were added under nitrogen atmosphere. After completely dissolution of *m*-phenylenediamine, the solution was frozen by cooling to -78°C. Isophthaloyl chloride (2.18 g, 10.8 mmol) was then added to the solution and the reaction temperature was raised to room temperature after isophthaloyl chloride was completely dissolved. The solution was stirred for 3 h and then poured into 400 mL methanol to obtain white fibrous precipitate. The obtained polymer was filtered, washed with methanol several times, and dried in a vacuum oven for 24 h at 120°C.

PA1: Yield 99 %. ^{1}H NMR(300 MHz, DMSO-d_6, δ, 25°C): 10.51 (s, -N*H*, 2H), 8.55 (s, Ar*H*, 1H), 8.40 (s, Ar*H*, 1H), 8.16 (d, *J*=9.0, Ar*H*, 2H), 7.69 (t, *J*=8.1, Ar*H*, 1H), 7.56-7.53 (m, Ar*H*, 2H), 7.35 (t, *J*=8.1, Ar*H*, 1H)

PA2: Yield 97 %. ^{1}H NMR(300 MHz, DMSO-d_6, δ, 25°C): 10.46 (s, -N*H*, 2H), 8.53 (s, Ar*H*, 1H), 8.15 (d, *J* = 9.0, Ar*H*, 2H), 7.82 (d, *J* = 9.0, Ar*H*, 2H), 7.70 (t, *J* = 7.5, Ar*H*, 1H), 7.07-7.04 (m, Ar*H*, 4H)

PA3: Yield 99 %. ^{1}H NMR(300 MHz, DMSO-d_6, δ, 25°C): 10.71 (s, -N*H*, 2H), 8.90 (s, Ar*H*, 1H), 8.40 (d, *J* = 9.0, Ar*H*, 2H), 8.26 (d, *J* = 9.0, Ar*H*, 2H), 7.88-7.83 (m, Ar*H*, 3H), 7.61 (t, *J* = 9.0, Ar*H*, 2), 7.33 (d, *J* = 9.0 Ar*H*, 2H).

PA4: Yield 98 %. ^{1}H NMR(300 MHz, DMSO-d_6, δ, 25°C): 10.31 (s, -N*H*, 2H), 8.46 (s, Ar*H*, 1H), 8.09 (dd, *J* = 3.0, 9.0, Ar*H*, 2H), 7.92 (t, *J* = 9.0, Ar*H*, 2H), 7.68-7.61 (m, Ar*H*, 2H), 7.40 (t, *J* = 9.0, Ar*H*, 2H), 7.32 (t, *J* = 9.0, Ar*H*, 2H), 7.13 (d, *J* = 9.0, Ar*H*, 4H).

2.4.3 Synthesis of polyamides with carboxylic acid

A series of polyamides with carboxylic acid (**PA2-xx**, where xx indicates the feed molar ratio of 3,5-diaminobenzoic acid among diamine comonomers) were synthesized by low temperature copolymerization from 3,5-diaminobenzoic acid, 4,4'-diaminodiphenyl ether and isophthaloyl chloride by controlling the molar ratio of diamine monomers. The typical procedure is described as follows using the copolymer **PA2-50** as an example. To a two-necked flask, 3,5-diaminobenzoic acid (0.725 g, 4.76 mmol), 4,4'-diaminodiphenyl ether (0.954 g, 4.76 mmol) and NMP (14.4 mL) were added under nitrogen atmosphere. After completely dissolution of diamine monomers, the solution was frozen by cooling to -78°C. Isophthaloyl chloride (1.93 g, 9.52 mmol)

was then added to the solution and the reaction temperature was raised to room temperature after isophthaloyl chloride was completely dissolved. The solution was stirred for 3 h and then poured into 400 mL methanol to obtain white fibrous precipitate. The obtained polymer was filtered, washed with methanol several times, and dried in a vacuum oven for 24 h at 120°C.

PA2-50 : Yield 2.86 g (98 %). ^{1}H NMR(300 MHz, DMSO-d_6, δ, 25°C): 10.60 (s, -N*H*, 1H), 10.34 (s, -N*H*, 1H), 8.70 (s, Ar*H*, 0.5H), 8.63 (s, Ar*H*, 0.5H), 8.55 (s, Ar*H*, 0.5H), 8.18-8.12 (m, Ar*H*, 3H), 7.81 (d, *J* = 9.0, Ar*H*, 2H), 7.72-7.65 (m, Ar*H*, 1H), 7.05 (d, *J* = 9.0, Ar*H*, 2H).

2.4.4 Preparation of PA membranes

10 wt% solutions of the obtained polyamides (**PA1**, **PA2**, **PA3**, **PA4**, and **PA2-xx**) were prepared in NMP and stirred by a magnetic stirrer at 70°C until the homogeneous polymer solutions were obtained. After cooling to the room temperature, the polymer solutions were filtered with a 0.45 μm poly(vinylidene fluoride) membrane filter. The filtered polymer solutions were then spin-coated onto a clean glass substrate to form as-cast membranes with < 2.0 μm thickness. Then, the as-cast membranes were heated at 70°C for 30 min and at 200°C for 1 h. The membranes were immersed into water to be peeled off from the glass substrate and stored in water. The obtained membranes were immersed into 10 wt% isopropanol aqueous solution for 15 min and into water for 15 min before evaluating their membrane intrinsic separation properties.

2.4.5 Preparation of PA membranes via non-solvent induced phase separation (PA2-20-additive)

A solution containing a polyamide (**PA2-20**) and aqueous additives was prepared by the addition of an appropriate amount of **PA2-20**, $MgCl_2$, H_2O, and ethylene glycol in NMP and stirred by a magnetic stirrer at 70°C until the homogeneous solution was obtained. The concentration of each components were finally as follows: **PA2-20** (6.5 wt%), NMP (58.1 wt%), $MgCl_2$ (4.8 wt%), H_2O (17.7 wt%), and ethylene glycol (12.9 wt%). After cooling to the room temperature, the solution was filtered with a 0.45 μm poly(vinylidene fluoride) membrane filter. The filtered solution was then spin-coated onto a clean glass substrate to form an as-cast membrane with < 2.0 μm thickness. Then, the as-cast membrane was immersed into cool water in order to remove the solvent and be peeled off from the glass substrate and stored in water. The obtained membrane was immersed into 10 wt% isopropanol aqueous solution for 15 min and into water for 15 min before evaluating its membrane intrinsic separation properties.

2.4.6 Evaluation of water and NaCl transport properties

Membrane disks of 7 cm diameter were placed in the cross-flow filtration cells of custom-made equipment. Under an operating pressure of 7.5 bar to perform membrane filtration, a 500 mg L^{-1} aqueous solution of NaCl was supplied to the membranes. The temperature and pH of the feed solution were kept at 25 °C and 6.5, respectively. Subsequently, the feed and permeate water were sampled after the operation had been continued for more than 3 h to stabilize the membrane performance. Salt rejection rate (*R* value) was calculated based on the electrical conductivities of the feed and permeate

water measured by a pH/EC meter (WM-50EG, DKK-TOA Corp.). The flow rate of the solution was 3.5 L/min. Water flux (J_w [L m^{-2} h^{-1}]), NaCl rejection (R [%]), hydraulic water permeability (A [L μm m^{-2} h^{-1} bar^{-1}]), and salt permeability (P_S [cm^2/s]) are calculated from the following equations.

$$J_w = \frac{\Delta V}{S\Delta t} \quad (2.1)$$

$$R = \left(1 - \frac{C2}{C1}\right) \times 100 \quad (2.2)$$

$$A = \frac{J_w l}{\Delta P - \Delta \pi} \quad (2.3)$$

$$B = \frac{10^{-7}}{3600} \times J_w l \times \frac{C_2}{(C_1 - C_2)} = \frac{10^{-7}}{3600} \times J_w l \times \frac{100 - R}{R} \quad (2.4)$$

where ΔV [L] is the volume of permeate water, S [m^2] is the effective membrane area, Δt [h] is time during water permeation, C_1 and C_2 are the salt concentrations in the feed and permeate water, l [μm] is the membrane thickness, ΔP [bar] is pressure difference across the membrane, and $\Delta \pi$ [bar] is osmotic pressure difference across the membrane. To clarify the relationships among *A*, *B*, and *R*, *R* is also expressed by the following equation: [16]

$$R = 100 \times \left(1 + \frac{B}{A(\Delta P - \Delta \pi)}\right)^{-1} \quad (2.5)$$

2.4.7 Determination of water sorption coefficient and water diffusion coefficient

Before the water uptake and dry density measurements, all of the PA

membranes were dried in vacuum oven at 120 °C for 2 days. Polymer densities (ρ_P [g cm^{-3}]) were determined using an Alfa Mirage SD-200L electronic densimeter at ambient temperature (24-25 °C) using the following equation:

$$\rho_P = \frac{m_A}{m_A - m_L}\rho_o \quad (2.6)$$

where m_A and m_L are weights of the membrane measured in air and non-solvent, respectively, and ρ_o is density of the non-solvent. Ethanol was selected as the non-solvent. To estimate water uptake (ω_w), the dried membranes were immersed in deionized water at ambient temperature (24-25 °C) for 3 days after weight of the dried membranes (m_d) were measured. Then, weight of hydrated membranes (m_h) were measured. ω_w was calculated as the following equation:

$$\omega_w = \frac{m_h - m_d}{m_d} \quad (2.7)$$

From ω_w value, equilibrium volume fraction of water in the hydrated membrane (ϕ_w) was evaluated as follows:

$$\phi_w = \frac{\rho_p \omega_w}{\rho_p \omega_w + \rho_w} \quad (2.8)$$

where ρ_w is density of water (1.0 g cm^{-3}). Using ϕ_w value, water sorption coefficient (K_w) can be estimated, which is defined as the ratio of water concentration in the membrane (C_w^m) to that in the solution (C_w) ([g water/cm^3 hydrated membrane]/[g water/ cm^3 solution]) as shown in the following equation.[17]

$$K_W = \frac{C_w^m}{C_w} = \frac{\phi_w M_w}{\rho_w V_w} \quad (2.9)$$

where C_w is equal to density of pure water (ρ_w), M_w is the molecular weight of water, and V_w is the molar volume of water (18 cm^3/mol).[9]

Diffusive water permeability (P_w [$cm^2\ s^{-1}$]) was related to water permeability (A [L μm $m^{-2}\ h^{-1}\ bar^{-1}$]) as follows:

$$P_w = A \times \frac{RT}{V_w} \times \frac{10^{-6}}{36} \quad (2.10)$$

where R is the ideal gas constant (8.314 J K^{-1} mol^{-1}) and T is the absolute temperature. Water diffusive coefficient (D_w, $cm^2\ s^{-1}$) estimated from P_w and K_w based on the following equation:

$$D_w = \frac{P_w}{K_w} \quad (2.11)$$

2.4.8 Determination of NaCl sorption coefficient and NaCl diffusion coefficient

Salt partition coefficient (K_s) was determined by salt desorption into deionized water from the membrane previously equilibrated with 50 mL of 1.0 M NaCl aqueous solution by immersing into that solution for at least 3 days. K_s is calculated by the ratio of the mass of the mass in the membrane per unit volume to the concentration of NaCl in the original solution as follows:

$$K_s = \frac{M_\infty \rho_p}{m} \times \frac{1}{58.44 \times 10^{-3}} \quad (2.12)$$

where M_∞ is the total weight of salt desorbed from membrane, m is weight of membrane, ρ_p is polymer density. Salt diffusion coefficient (D_S) is estimated from the measured salt permeability (B value):

$$D_s = \frac{B}{K_s} \quad (2.13)$$

2.4.9 Measurements

The nuclear magnetic resonance (NMR) spectra were recorded on a Bruker DPX-300S spectrometer at the resonant frequencies of 300 MHz for ^{1}H and 75 MHz for ^{13}C nuclei using $CDCl_3$ or DMSO-d_6 as the solvents and tetramethylsilane as an internal standard (δ_H 0.00). The FT-IR spectra were measured on a Horiba FT-720 spectrometer. The inherent viscosities were measured at 30 °C in NMP at a polymer concentration of 0.5 g dL^{-1}. Attenuated total reflectance Fourier transform infrared spectroscopy (ATR-FTIR) spectra were measured on Nicolet AVATAR 360. Solid-state ^{13}C cross polarization and magic angle spinning (CPMAS) NMR spectra were recorded on Chemagnetics CMX-300 Infinity spectrometer. Differential scanning calorimetry (DSC) thermograms were measured on TA Instruments DSC Q100 using Ishikiriyama's method.[18] The cross-sectional and surface morphologies of **PA2-20-additve** were characterized using a scanning electron microscope (SEM, JCM-5700, JEOL, Japan) operated at 15 kV and 5kV, respectively.

2.5 References

(1) Geise, G. M.; Lee, H.; Miller, D. J.; Freeman, B. D.; Mcgrath, J. E.; Paul, D. R. *J. Polym. Sci. Part B Polym. Phys.* **2010**, *48*, 1685–1718.

(2) Charcosset, C. *Desalination* **2009**, *245*, 214–231.

(3) Owen, G.; Bandi, M.; Howell, J. A. *J. Memb. Sci.* **1995**, *102*, 77–91.

(4) Lee, K. P.; Arnot, T. C.; Mattia, D. *J. Memb. Sci.* **2011**, *370*, 1–22.

(5) Greenlee, L. F.; Lawler, D. F.; Freeman, B. D.; Marrot, B.; Moulin, P. *Water Res.* **2009**, *43*, 2317–2348.

(6) Su, J.; Yang, Q.; Teo, J. F.; Chung, T. S. *J. Memb. Sci.* **2010**, *355*, 36–44.

(7) Lee, C. H.; Spano, J.; Mcgrath, J. E.; Cook, J.; Freeman, B. D.; Wi, S. *J. Phys. Chem. B* **2011**, *115*, 6876–6884.

(8) Geise, G. M.; Paul, D. R.; Freeman, B. D. *Prog. Polym. Sci.* **2014**, *39*, 1–42.

(9) Xie, W.; Cook, J.; Park, H. B.; Freeman, B. D.; Lee, C. H.; McGrath, J. E. *Polymer* **2011**, *52*, 2032–2043.

(10) Kim, Y. J.; Lee, K. S.; Jeong, M. H.; Lee, J. S. *J. Memb. Sci.* **2011**, *378*, 512–519.

(11) Park, H. B.; Freeman, B. D.; Zhang, Z. B.; Sankir, M.; McGrath, J. E. *Angew. Chem. Int. Ed. Engl.* **2008**, *47*, 6019–6024.

(12) Ikeda, K.; Endoh, R.; Tanaka, T.; Kurihara, M. *Desalination* **1977**, *21*, 35–44.

(13) Kwon, Y.; Leckie, J. *J. Memb. Sci.* **2006**, *282*, 456–464.

(14) Kim, Y. S.; Dong, L.; Hickner, M. A.; Glass, T. E.; Webb, V.; Mcgrath, J. E. *Macromolecules* **2003**, *36*, 6281–6285.

(15) Cited, L. *Ind. Eng. Chem. Anal. Ed.* **1936**, *8*, 306–307.

(16) Cath, T.; Childress, a; Elimelech, M. *J. Memb. Sci.* **2006**, *281*, 70–87.

(17) Geise, G. M.; Park, H. B.; Sagle, A. C.; Freeman, B. D.; McGrath, J. E. *J. Memb. Sci.* **2011**, *369*, 130–138.

(18) Ishikiriyama, K.; Sakamoto, A.; Todoki, M.; Tayama, T.; Tanaka, K.; Kobayashi, T. *Thermochim. Acta* **1995**, *267*, 169–180.

Chapter 3

Effect of *N*-Methyl Amide Linkage on Hydrogen Bonding Behavior and Water Transport Properties of Random Aromatic Copolyamide Membranes

3.1 Introduction

Hydrogen bonding is one of the principal molecular forces, which plays an important role in the self-assembly of biomacromolecules, such as proteins and deoxyribose nucleic acids (DNA), and provides high thermal and mechanical properties for synthetic polymers.[1] For example, the complementary hydrogen bondings of nucleobase pairs in DNA stabilize the double stranded helical structure.[2] Among the various hydrogen bondings, hydrogen bonding in the amide linkage acts as an especially important molecular force for oligopeptides, proteins, synthetic polymers, and so on.[3,4] In oligopeptides and proteins, hydrogen bonding of the amide linkages is the main driving force for the formation of tertiary and quaternary structures such as the α-helix, β-sheet, and foldings.[5] In the case of synthetic polymers, wholly aromatic polyamides (PA), such

as poly(*p*-phenylene isophthalamide) and poly(*m*-phenylene terephthalamide) known as typical super-engineering plastics, have been widely used as fibers due to their high tensile strength, high elastic modulus, and excellent flame resistance.[6,7] Their outstanding properties arise from their rigid aromatic backbone and secondary amide linkages in the *trans* conformation, which result in the extended rod-like polymer structure that interacts with each other via strong π-π stackings and hydrogen bondings, and produce a sheet structure.[8] On the other hand, aromatic oligoamides containing the three-center hydrogen bonding, in which the oxygen atom of the alkyloxy side chain disrupts the interrmolecular hydrogen bondings among the amide linkages due to the coordination of a lone pair on the oxygen atom to the amine proton in the amide linkage, provide a highly planar molecular backbone and fold into a specific secondary structure such as molecular crescents, helices, and macrocycles.[9–11] For the poly(*p*-benzamide), the attachment of triethylene glycol chains to the aromatic rings improved their organosolubility and produced a completely flat polymer backbone due to the disruption of hydrogen bonding by the three-center hydrogen bonding.[12] Thus, the control over the hydrogen bonding of the amide linkage is quite important to obtain the desirable molecular aggregation structures and mechanical properties.

Whereas the hydrogen bonding in the secondary amide linkage is considerably attractive, much attention has also been paid to the tertiary amide linkage, since the tertiary amide linkage prefers the *cis* conformation that suppresses the hydrogen bonding, resulting in a coil-like structure of the polymer chain.[13–16] The *N*-alkylated PAs were prepared via a post-polymerization reaction, in which the metalation of the proton of the amide linkage was carried out to produce the polyanion, followed by a substitution reaction with alkyl bromides. As have been reported by Shi et al., the solubility,

crystallization and melting behaviors, and interplanar spacing were influenced by the length of the alkyl side chain in the *N*-alkylated poly(*p*-benzamide).[17] Yokozawa et al. developed the remarkable synthetic procedure of the *N*-alkylated PAs with narrow polydispersities and well-controlled molecular weight using a chain-growth polycondensation reaction.[18] Furthermore, the well-defined poly(*p*-benzamide) containing a chiral alkyl side chain on the nitrogen atom could possess a flexible helical structure due to the *cis* conformation of the tertiary amide linkages and *syn* arrangement of the benzene rings.[19] Similar to the case of the three-center hydrogen bonding, the suppression of hydrogen bonding by the tertiary amide linkage affects the thermal properties and the packing mode of the polymer main chain, and folds into the specific polymer structure.[20,21]

As has been discussed in previous chapters, PAs have been considered as one of the membrane materials for water treatment,[22–24] and a state-of-the-art commercial reverse osmosis (RO) membrane is a thin film composite membrane composed of a densely crosslinked PA active layer on a microporous support, wherein the separation of water from salty water is effectively achieved through the dense PA active layer.[25] Hence, the effect of the chemical and morphological structures of the PA layer on permselectivity should be clarified in order to achieve a further improvement. To the best of our knowledge, the semipermeable membranes based on *N*-alkylated PAs have never been prepared, and the effect of the hydrogen bonding behavior of the amide linkage on the water transport properties still remains unclear. Furthermore, in chapter 2, we have revealed that it is important to suppress the hydrogen bonding for the improvement in water transport properties.

In this chapter, we report the synthesis of novel partially *N*-methylated random

aromatic coPAs (**PA-X-Y**, where **X** and **Y** indicate the feed molar percent of 3,5-diaminobenzoic acid (DABA) or *N*,*N*'-dimethyl-4,4'-diaminodiphenyl ether (MDAE) among the diamine comonomers, respectively) composed of three repeating units, such as the hydrophilic secondary amide unit containing a carboxylic acid group, the *N*-methylated tertiary amide unit, and the secondary amide unit (see **Figure 3-1**). Furthermore, the hydrogen bonding behavior of **PA-X-Y** in solutions and solid films, and its effect on the water and salt transport properties were investigated in detail.

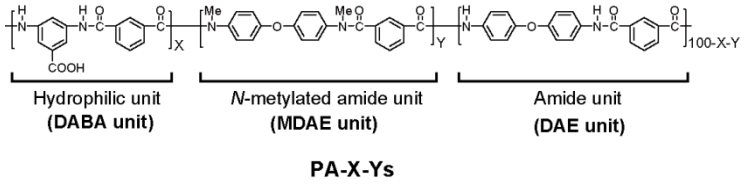

Figure 3-1 Chemical structure of partially *N*-methylated random aromatic coPAs (**PA-X-Y**).

3.2 Result and discussion

3.2.1 Synthesis and characterization

N,*N*'-Dimethyl-4,4'-diaminodiphenyl ether (MDAE) was prepared according to a previous report and characterized by ^{1}H NMR, ^{13}C NMR, and FT-IR spectra.[26] Subsequently, the **PA-X-Ys** were synthesized by the low temperature solution polycondensation of IPC with aromatic diamines, DABA, MDAE, and DAE, as shown in **Scheme 3-1**. The random copolymer structures of the **PA-X-Ys** were designed to decrease the crystallinity, which is favorable for increasing the water sorption.[27] MDAE was employed as a comonomer to produce the tertiary amide linkage for suppressing the hydrogen bonding, in which the *N*-methyl group was selected because rigid-rod polymers containing flexible long alkyl chains tend to crystallize into a layered structure.[28,29] Also, DABA with a hydrophilic carboxylic acid group was used as a comonomer to increase the water permeability of the resulting PAs.[30]

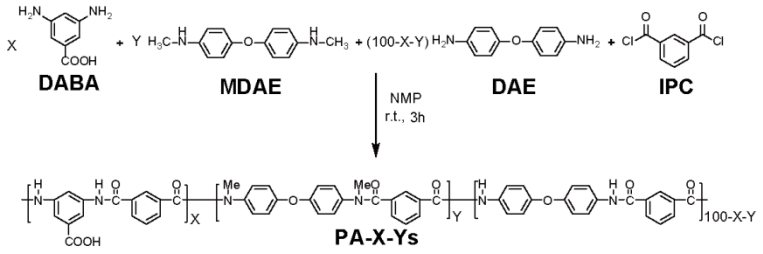

Scheme 3-1 Synthesis of **PA-X-Ys**.

The chemical compositions of **PA-X-Ys** (**PA-20-0**, **PA-0-20**, **PA-20-20**, **PA-20-40**, and **PA-20-60**) were precisely controlled by varying the feed molar ratio of DABA and MDAE among the diamine comonomers, and the chemical structures were fully characterized by their ^{1}H NMR and FTIR spectra (**Figure 3-2**). In the case of **PA-0-0**, the chemical composition was confirmed by its ^{1}H NMR, ^{13}C NMR, and FTIR spectra. On the other hand, the ^{1}H NMR spectrum of **PA-20-0** showed that the ratio of integrals of the aromatic and amide protons of the DABA and DAE units was in good accordance with the expected PA structure. For the **PA-0-20**, **PA-20-20**, **PA-20-40**, and **PA-20-60**, two characteristic signals are observed at 3.38 ppm and 3.28 ppm (denoted as G (*cis*) and G (*trans*), respectively), which correspond to the methyl protons of the tertiary amide linkage in the *cis* (*Z*) and *trans* (*E*) conformations. The peak of the methyl proton of the tertiary amide linkage in the *cis* conformation is observed at lower magnetic field than that in the *trans* conformation because the methyl group is closely located to the phenyl ring plane.[14] The desired chemical structures and molar compositions of these PAs were confirmed by the comparison of the integral values of the methyl peaks to all the ArH protons. The integral values of all the ArH peaks are totally calculated as 12.0 for **PA-0-20** and **PA-20-20**, and 11.0 for **PA-20-40** and **PA-20-60**, respectively. While, the integral values of the methyl peaks are 1.28 for **PA-0-20** and **PA-20-20**, 2.43 for **PA-20-40**, and 3.56 for **PA-20-60**, respectively, which are in good agreement with the calculated values of 1.20, 2.40, and 3.60, respectively. The resulting **PA-X-Ys** exhibited good solubilities in polar aprotic solvents, such as DMF, DMSO, DMAc and NMP, and all polymers possess high inherent viscosity (η_{inh}) values as listed in **Table 3-1**.

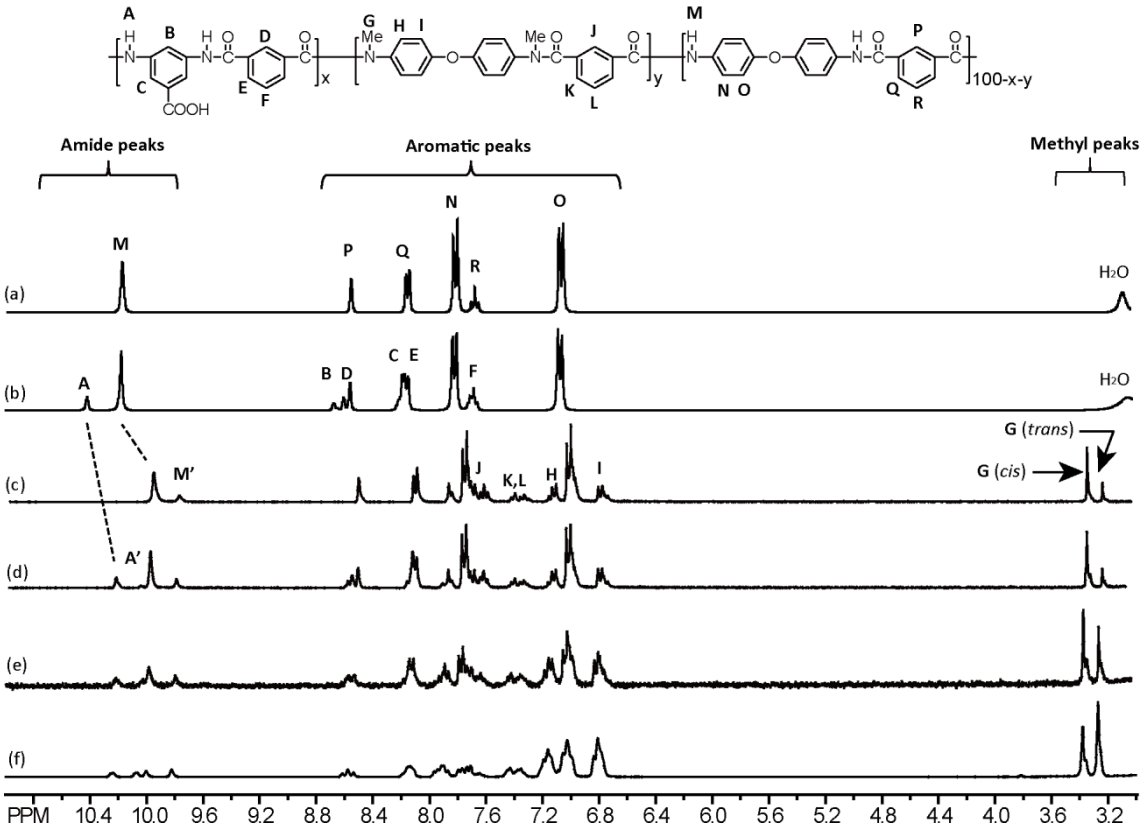

Figure 3-2 ^{1}H NMR spectra of (a) **PA-0-0**, (b) **PA-20-0**, (c) **PA-0-20**, (d) **PA-20-20**, (e) **PA-20-40**, and (f) **PA-20-60** in DMSO-d_6 at 100 °C.

3.2.2 Thermal properties

The thermal stabilities of the **PA-X-Ys** were evaluated by thermogravimetry (TG) analysis under a nitrogen atmosphere. All of the samples were preheated at 250 °C for 30 min to remove any moisture and residual solvents. As can be seen in **Figure 3-3**, **PA-0-0** and **PA-20-0** show a distinct single-step weight loss behavior attributed to the degradation of the polymer main chains. On the other hand, two-step thermal decomposition behaviors are observed from 300 to 350 °C and above 400 °C for **PA-20-0**, **PA-20-20**, **PA-20-40**, and **PA-20-60**. The first and second weight losses are attributed to the decomposition of the carboxylic acid groups and the polymer main chains, respectively. The 5 % weight loss temperatures ($T_{d5\%}$) of all the samples are found to be more than 350 °C, which indicates that the thermal stability is not significantly affected by the introduction of the *N*-methyl amide linkage into the polymer backbone. Furthermore, all PAs show no glass transition up to the decomposition temperature. This is probably due to the rigid aromatic polymer backbones.

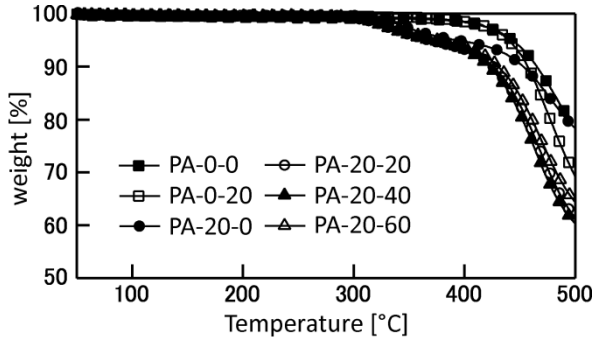

Figure 3-3 TG curves of **PA-X-Ys** under nitrogen atmosphere.

3.2.3 Conformational preference and hydrogen bonding behavior

The *cis* conformational preference in the *N*-methyl amide linkage was evaluated for **PA6-0-20** and **PA6-20-20**, **PA6-20-40,** and **PA6-20-60** using the following equation:

$$cis \text{ preferenece } [\%] = \frac{I_{cis}}{I_{cis} + I_{trans}} \times 100 \quad (3.1)$$

where I_{cis} and I_{trans} are the integral values of the methyl peaks at 3.38 ppm and 3.28 ppm, respectively (**Figure 3-2**). Although the *N*-alkylated amide compounds prefer *cis* to *trans* conformation in a solution and crystal, the calculated values of the *cis* preference reveal that the increase in the ratio of the MDAE unit in the polymer backbone leads to a decrease in the content of the *cis* conformation in the amide linkages as shown in **Table 3-1**.[14,16] As has been discussed in the previous report by Lorenzi et al., the relaxation of the steric interactions in the **PA-X-Ys** leads to the lower content of the *cis* conformation in the tertiary amide linkage than that in the low molecular compounds.[31] The total contents of the *cis* conformation, however, are maintained from 15 to 25 mol% for **PA-0-20**, **PA-20-20**, **PA-20-40**, and **PA-20-60**.

Table 3-1 *Cis* preferences and inherent viscosities of **PA-X-Ys**.

		PA-0-0	PA-0-20	PA-20-0	PA-20-20	PA-20-40	PA-20-60
cis preference[a]	[%]	ND	76.4	ND	76.2	59.7	40.9
η_{inh}	[g dL^{-1}]	1.78	1.21	1.61	1.29	1.03	0.93

[a]Determined by the ratio of integral values of peaks assigned as the methyl proton in the *trans* and *cis* conformations. [b]Evaluated at 30 °C in NMP at a concentration of 0.5 g dL^{-1}.

Besides, the chemical shift of the amide proton provides us the information about the hydrogen bonding.[32] In general, the chemical shift of the amide proton is moved to downfield when the hydrogen bonding becomes strong.[32] Thus, the effect of the introduction of the *N*-methyl amide linkage on the hydrogen bonding behavior in solution was investigated by comparing their chemical shifts at 40 °C and 100 °C. For **PA-0-0**, the chemical shifts of the amide protons denoted as **M** move from 10.41 ppm to 10.18 ppm with increasing the temperature. This result indicates that the hydrogen bonding between the amide linkages has become weak with increasing the temperature. **PA-20-0** also shows the same behavior. Meanwhile, for the other **PA-X-Ys**, two new peaks (**M'** and **A'**) are appeared. These peaks are assigned to the protons in the amide linkages of the DAE and DABA units next to the MDAE unit as shown in **Figure 3-4**. The *N*-methyl amide linkage acts as an electron-donating group to an adjacent benzene ring and increases the electron density. The amide peaks attributed to **M** of **PA-0-20**, **PA-20-20**, **PA-20-40**, and **PA-20-60** at 100 °C are observed at 9.88 ppm, 10.00 ppm, 9.99 ppm, and 10.00 ppm, respectively. Compared to **PA-0-0** or **PA-20-0**, these chemical shifts are observed at the higher magnetic field, indicating that the suppression of hydrogen bonding is promoted by the replacement of the hydrogen atom with the methyl group in the amide linkage. The peaks corresponding to **A** also show a similar behavior. In other words, the introduction of the *N*-methyl amide linkage will efficiently prohibit the aggregation of the polymer chains in solution. On the other hand, the peaks of **A** of **PA-20-20**, **PA-20-40**, and **PA-20-60** at 40 °C appear at 10.62 ppm, 10.59 ppm, and 10.59 ppm, respectively, which are slightly lower than that of **PA-20-0** (10.69 ppm). A similar trend is also observed for peak **M**. In the cases of **PA-0-0** and **PA-0-20**, the chemical shift values of peak **M** at 40 °C

are 10.41 ppm and 10.36 ppm, respectively. These results indicate that the hydrogen bonding is partially suppressed by the *N*-methyl amide linkage even at 40 °C.

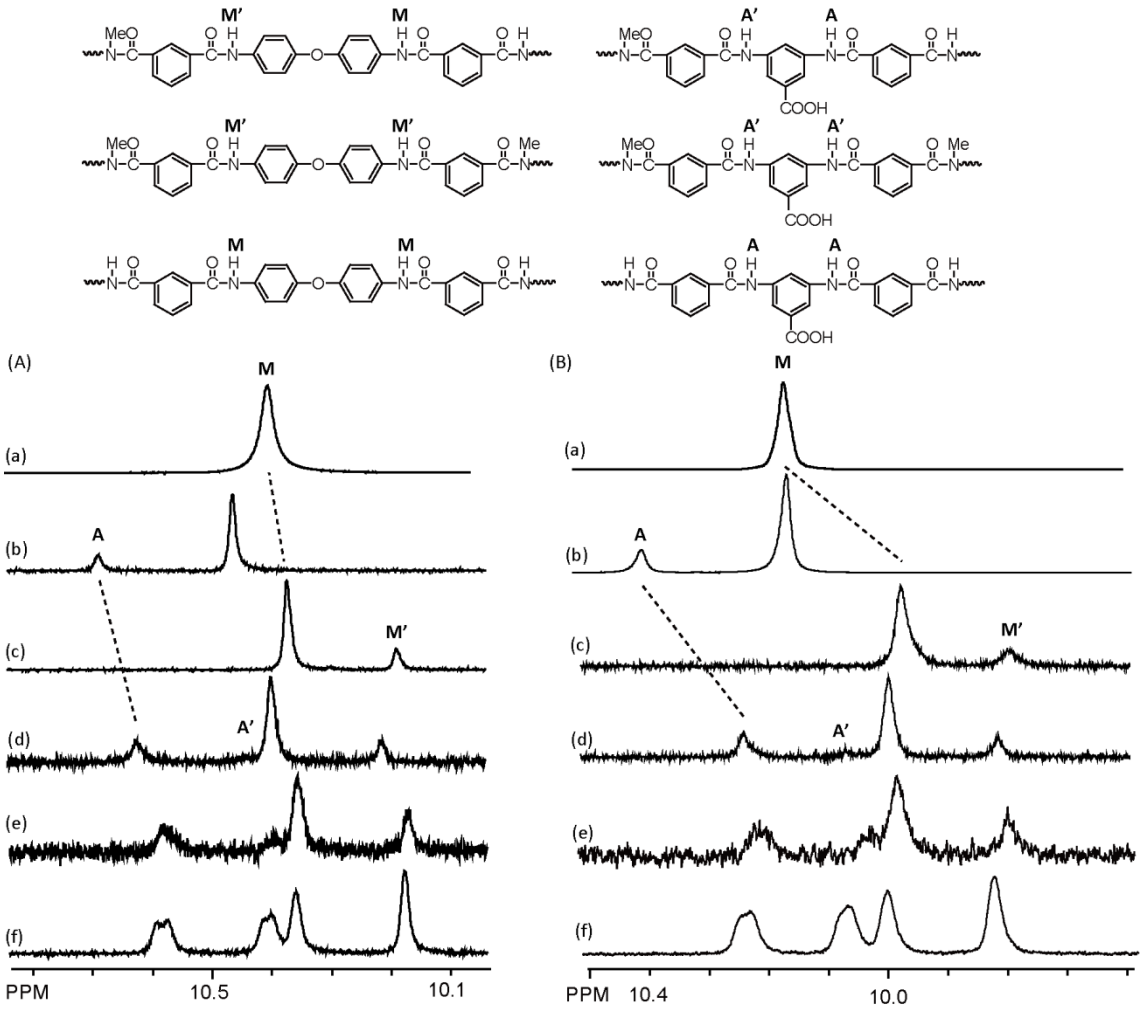

Figure 3-4 ^{1}H NMR spectra showing the region of the amide linkage signals of (a) **PA-0-0**, (b) **PA-20-0**, (c) **PA-0-20**, (d) **PA-20-20**, (e) **PA-20-40**, and (f) **PA-20-60** in DMSO-d_6 at (A) 40 and (B) 100 °C.

3.2.4 Membrane properties

3.2.4.1 Dry densities and water uptakes

All of the **PA-X-Ys** membranes with less than 2 μm thickness were successfully prepared by a spin-coating method. Densities of the dry membranes were measured for estimation of free volume which affects water and salt transport properties.[33, 34] With the increase in the ratio of the MDAE unit in the polymer backbone, dry density (ρ_p) clearly decreases relative to **PA-0-0** (1.316 g/cm^3) and **PA-0-20** (1.295 g/cm^3) (**Table 3-2**). These results indicate that the disruption of the polymer packing probably occurs because the *N*-methyl amide linkages suppress the hydrogen bonding. Moreover, the *cis* conformation in the *N*-methyl amide linkage leads to the configurational change in the polymer in solution from rigid-rod to random-coil chains.[15] The polymers having rigid-rod and random-coil units exhibited a low compatibility and miscibility between the rigid-rod and random-coil units.[35,36] Thus, the *cis* conformation of the *N*-methyl amide linkage in **PA-0-20**, **PA-20-20**, **PA20-40**, and **PA-20-60** would also affects the structure of polymer chains in solution and leads to a decrease in the dry density of the membranes. Water uptake (ω_w) values of the PA membranes possessing the hydrophilic carboxylic acid groups are summarized in **Table 3-2**. Any differences in ω_w values could not be seen even if the *N*-methyl amide linkages were introduced into the polymer backbone.

Table 3-2 Dry densities, and water uptake of **PA-X-Y** membranes

		PA-0-0	PA-0-20	PA-20-0	PA-20-20	PA-20-40	PA-20-60
ρ_p [a]	[g cm^{-3}]	1.316 ± 0.008	1.295 ± 0.009	1.284 ± 0.009	1.270 ± 0.001	1.262 ± 0.005	1.254 ± 0.002
ω_w [b]	[%]	ND	ND	4.2 ± 0.3	4.7 ± 1.3	4.9 ± 1.3	5.3 ± 1.3

[a]Dry density was measured at ambient temperature 24-25 °C in ethanol. [b]Water uptake was measured by immersing into water for 3 days.

3.2.4.2 FTIR spectra

Figure 3-5 shows the FTIR spectra of the **PA-X-Ys** to evaluate the hydrogen bonding behavior in the solid film state. Generally, the peak assigned as the C=O stretching shifts to the higher wavenumber, and the peak of the N-H in-plane bending shifts to the lower wavenumber when the hydrogen bonding becomes weak.[37] In the **Figure 3-5** (a), the peaks at 1654 cm^{-1} and at 1527 cm^{-1} are attributed to the C=O stretching and the N-H in-plane bending of the secondary amide linkage in **PA-0-0**, respectively. The peaks of the C=O stretching and N-H in-plane bending in **PA-0-20** are also observed at 1654 cm^{-1} and 1527 cm^{-1}, respectively. For **PA-20-0**, the peaks assigned as the C=O stretching are also observed at 1658 cm^{-1} and the peak for the N-H in-plane bending appears at 1535 cm^{-1}. **PA-20-20**, **PA-20-40**, and **PA-20-60** show peaks for the C=O stretching at the higher or lower wavenumbers (1659 cm^{-1}, 1650 cm^{-1}, and 1650 cm^{-1}, respectively) compared to **PA-20-0**. Since the peak for the C=O stretching in the tertiary amide linkage usually appears at lower wavenumber than that for the secondary amide linkage, and overlaps with the peak of the secondary amide linkage in **PA-20-40** and **PA-20-60**, thus becoming broad, it seems difficult to evaluate the hydrogen bonding behavior of these samples.[21] However, all the peaks corresponding to the N-H in-plane bending of **PA-20-20**, **PA-20-40**, and **PA-20-60** are confirmed at lower wavenumber (1531 cm^{-1}). Similar to the dry density measurements, these results also suggest that the hydrogen bondings between amide linkages are suppressed by the introduction of the tertiary amide linkage into the polymer backbone.

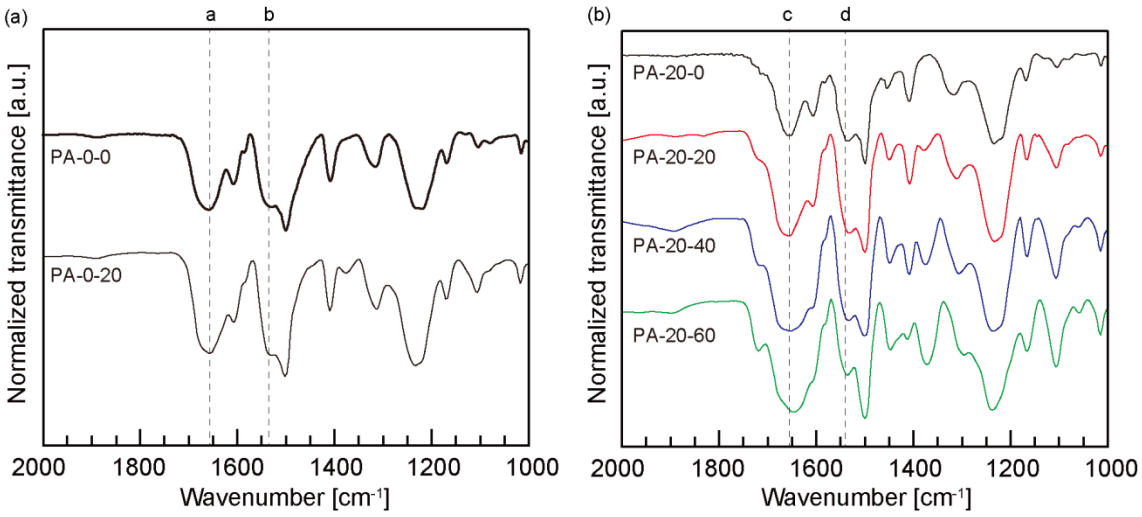

Figure 3-5 FTIR spectra of (a) **PA-0-0** and **PA-0-20** and (b) **PA-20-0**, **PA-20-20**, **PA-20-40**, and **PA-20-60** (Film). The dashed lines (labeled as a, b, c, and d) are corresponding to the wavenumbers at 1654, 1527, 1658, and 1535 cm^{-1}, respectively.

3.2.4.3 Time resolved contact angle measurement

The surface hydrophilicity and chain mobility is also considered as one of the most important factors in determining the water and salt transport properties.[38] Thus, the time-resolved contact angle measurements of the **PA-X-Y** membranes were carried out to evaluate the surface hydrophilicity and surface reorganization behavior. Since the contact angle value is mostly affected by the surface roughness, the root-mean-square roughness (R_{RMS}) of **PA-X-Ys** were determined by atomic force microscopy (AFM). The R_{RMS} values for all the films were ranged from 0.2 to 0.8 nm, which indicated that the contact angle values were independent of the surface roughness. The water contact angles of **PA-0-0** and **PA-0-20** linearly decreased with the increasing time. On the other hand, two regions (an initial exponential decay and the following linear line) can be seen in the **PA-20-0**, **PA-20-20**, **PA-20-40**, and **PA-20-60**. As has been discussed in the previous reports by Tanaka et al., the initial contact angle decay and a subsequent linear decrease reflect both the surface segregation induced by the water droplet and the change in the droplet shape due to water evaporation, respectively.[39,40]

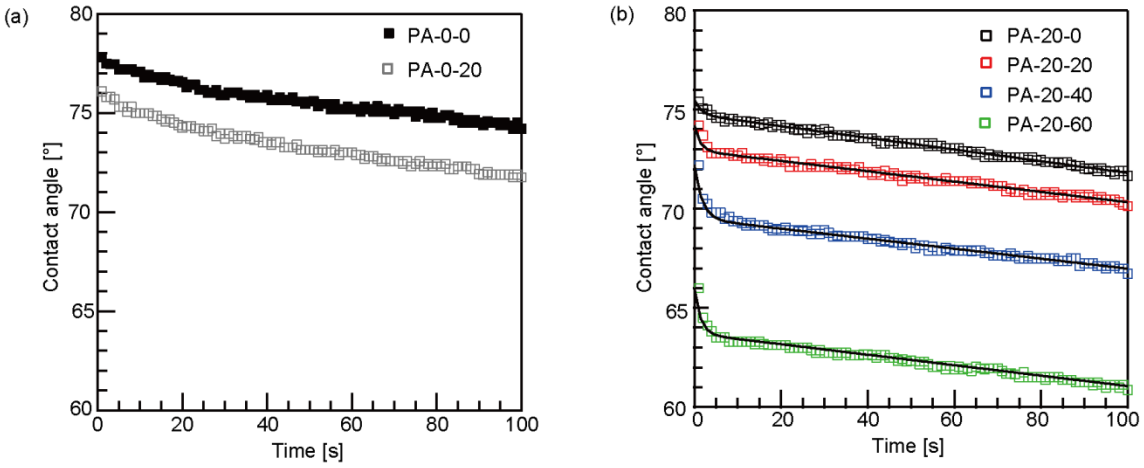

Figure 3-6 Time dependence of water contact angle for (a) **PA-0-0** and **PA-0-20** and (b) **PA-20-0**, **PA-20-20**, **PA-20-40**, and **PA-20-60**.

As the initial decay cannot be seen in **PA-0-0** and **PA-0-20**, the segregation would arise not from the amide linkages in the MDAE and DAE units but from the carboxylic acid group in the DABA unit. Additionally, the experimental plot for the time-resolved water contact angles were fitted by the following equation:[41]

$$\theta(t) = (\theta_{\mathrm{ini}} - \theta_{\mathrm{ter}})\exp\left(-\frac{t}{\tau}\right) - kt + \theta_{\mathrm{ter}} \quad (3.2)$$

where θ_{ini} and θ_{ter} are the initial and terminal values of the contact angles at t = 0 and in a quasi-equilibrium state, τ is the time constant of the contact angle decay in the initial stage, and k is the constant related to water evaporation, respectively. Especially, τ is correlated to the relaxation time of the interfacial mobility, and the difference in the θ_{ini} and θ_{ter} values means the degree of surface reorganization induced by the water.[39,41] Table 3-3 summarizes the θ_{ini}, θ_{ter}, and τ values of all **PA-X-Y** membranes. With the increase in the MADE units, the τ values decreased from 2.23 to 1.46. Taking into account the results from FTIR and dry density measurements, the decrease in the τ value is probably due to suppressing the aggregation of the polymer chains induced by the *N*-methyl amide linkage. Meanwhile, the differences in the θ_{ini} and θ_{ter} values increased from 1.4° to 4.4°, indicating that the number of carboxylic acid oriented toward the polymer/water interface increased.

Table 3-3 θ_{ini}, θ_{ter}, and τ values of **PA-X-Ys**.

		PA-0-0	PA-0-20	PA-20-0	PA-20-20	PA-20-40	PA-20-60
θ_{ini}[a]	[°]	77.8	76.2	76.2	74.2	73.7	68.1
θ_{ter}[a]	[°]	ND	ND	74.8	72.9	69.5	63.7
τ[a]	[s]	ND	ND	2.23	2.50	1.94	1.46

[a]Time-resolved contact angle measurement was carried out by using the sessile drop method with water droplt of 2.0 μL.

Also, it is noted that **PA-0-0** and **PA-0-20** show higher θ_{ini} value than those for **PA-20-0**, **PA-20-20**, **PA-20-40**, and **PA20-60** due to the absence of the hydrophilic **DABA** unit. The θ_{ini} value decreases from 76.2° to 68.1° with increasing the content of the *N*-methyl amide linkage in the polymer backbone, suggesting that more hydrophilic domains in **PA-X-Ys** are formed with the suppression of the hydrogen bonding and the aggregation of the polymer chains. Such an interfacial behavior will be discussed in detail after presenting the tapping mode phase image by AFM measurements.

3.2.4.4 AFM observation

To clarify the phase separation between the hydrophilic and hydrophobic domains, the tapping mode phase images of the surfaces of the **PA-0-20**, **PA-20-0**, **PA-20-20**, **PA-20-40**, and **PA-20-60** membranes were recorded under ambient conditions on 250 × 250 nm^2 size scales by AFM measurements (**Figure 3-7**). Even though all samples are random PAs**,** nanophase separations are clearly observed. The **PA-0-20** membrane shows the bright and dark regions derived from the hard segments corresponding to the DAE units and the soft segments corresponding to the MDAE units, respectively, which imply the low miscibility of secondary and tertiary amide linkages. In the **PA-20-0** membrane, the bright and dark regions derived from the hard segments corresponding to the DAE units and the soft segments corresponding to the hydrophilic DABA units, respectively, are clearly observed. Moreover, the dark regions seem to be connected and form hydrophilic channels. The domain sizes and distributions of the **PA-0-20** and **PA-20-0** membranes are apparently different probably due to the significant difference of their polarity. The **PA-20-60** membrane exhibits a clearer nanophase separation compared to the **PA-20-20** and **PA-20-40** membranes. The significant difference in their polarities between the DAB and MDAE units may induce the lower miscibility between two parts. Taking into account the comparison of the differences in the θ_{ini} and θ_{ter} values of **PA-20-0**, **PA-20-20**, **PA-20-40**, and **PA-20-60**, an increase in the size of the hydrophilic domains and the suppression of the hydrogen bonding would support the increase in the degree of surface reorganization induced by the water and the decrease in the θ_{ini} value.

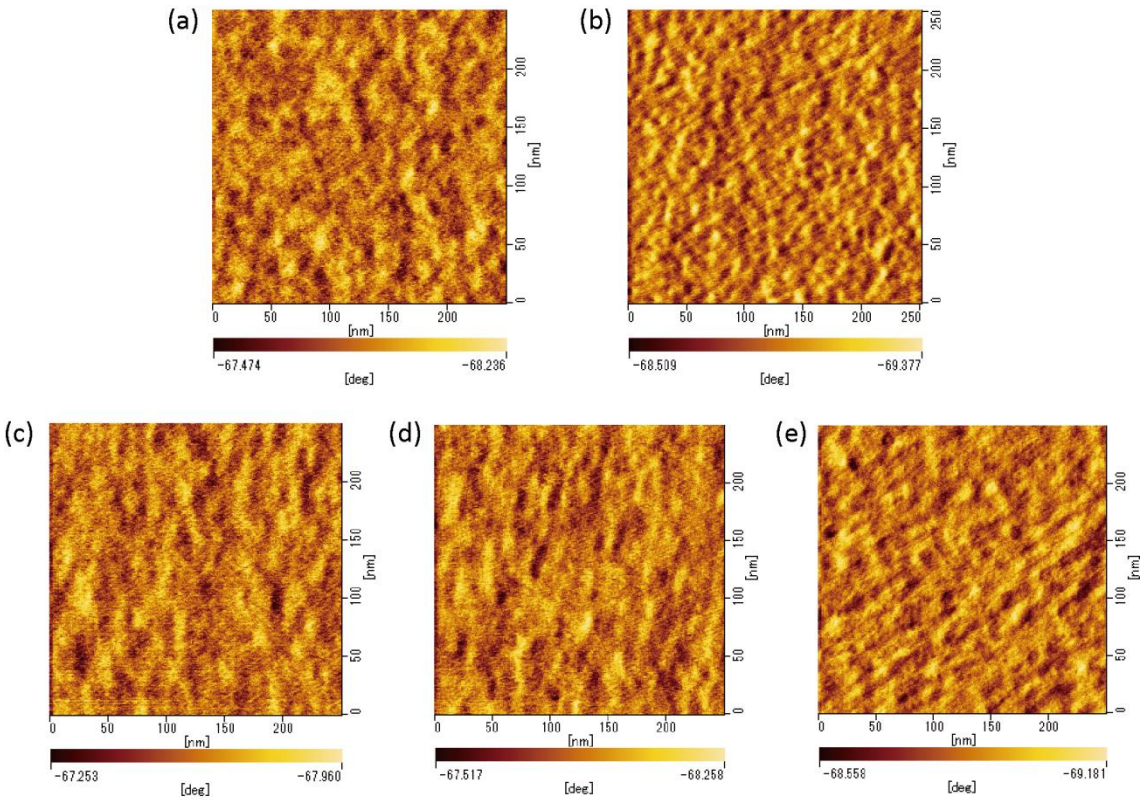

Figure 3-7 AFM tapping mode phase images of (a) **PA-0-20**, (c) **PA-20-0**, (d) **PA-20-20**, (e) **PA-20-40**, and (f) **PA-20-60** membranes. Scan sizes are 250 × 250 nm^2.

3.2.4.5 PALS

To assess the free volume of the **PA-20-Y** membranes, low-energy positron annihilation lifetime spectroscopy (PALS) was carried out at room temperature. The positron lifetime spectra (**Figure 3-8**), obtained at an incident positron energy of 7 keV, were analyzed on the basis of an exponential decay function with three lifetime components using the RESOLUTION code of the PATFIT package to attain the triplet *ortho*-positronium (*o*-Ps) lifetime (τ_3). The free-volume hole radii (r_3) were determined from τ_3 using the Tao-Eldrup model as follows:[42,43]

$$\tau_3^{-1} = 2\left\{1 - \frac{r_3}{r_3 + 0.166} + \frac{1}{2\pi}\sin\left(\frac{2\pi r_3}{r_3 + 0.166}\right)\right\} \quad (3.3)$$

The mean size of the sperical free volumes (V_3) were calculated according to the following equation:

$$V_3 = \frac{4}{3}\pi r_3^3 \quad (3.4)$$

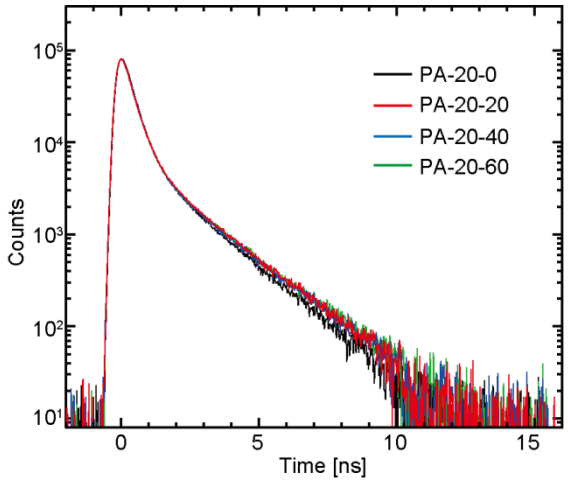

Figure 3-8 Positron lifetime spectra of **PA-20-Ys**.

Table 3-4 summarizes the PALS results for **PA-20-Y** membranes. **PA-20-0** has the values for τ_3 and r_3, apparently lower than the other membranes, **PA-20-20**, **PA-20-40**, and **PA-20-60**, implying that the introduction of the *N*-methyl amide linkage leads to the increase in the free volume size. Indeed, the V_3 value increased from 0.069 to 0.089 nm^3 with increasing in the MDAE unit content. This observation indicates that the suppression of the hydrogen bonding and the conformational change, induced by the introduction of the *N*-methyl amide linkage, lead to the increase in free volume size, in good accordance with the results from FTIR and dry density.

Table 3-4 PALS results for **PA-20-Ys**

		PA-20-0	PA-20-20	PA-20-40	PA-20-60
τ_3 [a]	[ns]	1.69±0.01	1.84±0.01	1.83±0.01	1.89±0.01
r_3 [b]	[nm]	0.256	0.271	0.271	0.277
V_3 [c]	[nm^3]	0.069	0.084	0.084	0.089

[a] τ_3 and I_3 were estimated by analyzing the PALS spectrum using the RESOLUTION fit. [b] r_3 was detemined by Tao-Endrup equation. [c] V_3 is calculated by $(4\pi/3)\times r_3^3$.

3.2.4.6 Proposed mechanism

The difference in the hydrogen bonding behavior and the configurational difference during the fabrication process would affect the aggregation behaviors in the obtained membranes. **PA-0-0** and **PA-20-0** act as rigid-rod polymers in the casting solution, whereas **PA-0-20**, **PA-20-20**, **PA-20-40**, and **PA-20-60** with the *N*-methyl amide linkage in the *cis* conformation behave as random-coil chains. During evaporation of the solvent, hydrogen bondings in the **PA-20-20**, **PA-20-40**, and **PA-20-60** are more suppressed than those of the PAs without the *N*-methyl amide linkage. Finally, the state of the polymers in the membranes obtained from **PA-0-0** and **PA-20-0** are more densely packed. On the other hand, the polymers in the membrane of **PA-0-20**, **PA-20-20**, **PA-20-40**, and **PA-20-60** are loosely packed because of the suppression of the hydrogen bonding and the low compatibility of the polymer chains.

3.2.5 Water and NaCl transport properties

Finally, the influence of introducing the *N*-methyl amide linkages into the polymer backbone on the water and NaCl transport properties was investigated. All measurements were carried out by the cross-flow instruments in the RO mode at an applied pressure of 7.5 bar, and the results are summarized in **Table 3-5**. **PA-0-0** shows no water permeation behavior. In spite of the introduction of the *N*-methyl amide linkage, the water permeation phenomenon cannot be observed for **PA-0-20**. These results agree with the results in chapter 2, which revealed that the ultrathin semipermeable membrane based on PAs without a carboxylic acid group could not show any water permeation even if a flexible or rigid molecular unit was incorporated into the polymer backbone. On the other hand, **PA-20-0**, **PA-20-20**, **PA-20-40**, and **PA-20-60** with a carboxylic acid group show a water permeation property. Moreover, **PA-20-60** with the higher contents of the *N*-methyl amide linkage leads to higher water flux (2.25 L m^{-2} h^{-1}) and water permeability (*A* value: 0.636 L μm m^{-2} h^{-1} bar^{-1}) than those

Table 3-5 Water and NaCl transport properties

Polymer	J_w^a [L m^{-2} h^{-1}]	R^a [%]	A^a [L μm m^{-2} h^{-1} bar^{-1}]	B^a [cm^2 s^{-1}]	K_w^b	D_w^b [cm^2 s^{-1}]	K_s^c	D_s^c [cm^2 s^{-1}]
PA-0-0	ND	ND	ND	ND	ND	ND	ND	ND
PA-0-20	ND	ND	ND	ND	ND	ND	ND	ND
PA-20-0	0.50	24	0.141	0.0088×10^{-8}	0.076	0.709×10^{-5}	0.055	1.61×10^{-9}
PA-20-20	1.88	10	0.530	0.093×10^{-8}	0.073	2.771×10^{-5}	0.064	1.45×10^{-8}
PA-20-40	1.75	12	0.495	0.071×10^{-8}	0.069	2.741×10^{-5}	0.060	1.20×10^{-8}
PA-20-60	2.25	8	0.636	0.144×10^{-8}	0.068	3.563×10^{-5}	0.041	3.44×10^{-8}

[a]Measured at 25 °C using cross-flow filtration (ΔP =7.5 bar ; NaCl concentration = 500 mg L^{-1}) . [b]Estimated from w ater uptake and dry density. [c]Measured by NaCl desorption measurement.

of **PA-20-0** (water flux (J_w) : 0.50 L m^{-2} h^{-1}, A value : 0.141 L μm m^{-2} h^{-1} bar^{-1}). The increases in the free volume and distinct hydrophilic domains in the membrane may allow the formation of an efficient pathway for water permeation. Indeed, the increase in water diffusive coefficient (D_w) value from 0.709 × 10^{-5} cm^2 s^{-1} to 3.563 × 10^{-5} cm^2 s^{-1} is observed. Meanwhile, salt diffusive coefficient (D_s) value of **PA-20-60** is about 20 times higher than that of **PA-20-0**. As a result, NaCl rejection (R) and salt permeability (B) decrease with increasing the molar ratio of the MDAE units in the polymer backbone.

According to the free volume theory, the small molecule diffusion coefficient is correlated to the free volume and the hydrated size of the molecule as the following equation.[45]

$$D_i = a_i \exp\left(-\frac{b_i}{\langle v_f \rangle}\right) \quad (3.6)$$

where a_i is the constant, b_i is the constant related to the hydrated size of the penetrant, and $\langle v_f \rangle$ is the polymer's average free volume. Thus, when the size of the penetrant is increased, the effect of the change of $\langle v_f \rangle$ value on the diffusion coefficient becomes higher. The larger effective radii of Na^+ (0.358 nm) and Cl^- (0.332 nm) than H_2O molecule (0.138 nm) indicates that D_w value is less influenced by the change of the free volume than D_s value.[33,46] This expectation is verified by plotting $\ln D_w$ and $\ln D_s$ versus V_3^{-1} estimated from the PALS measurement as shown in **Figure 3-9** (a). Over the range of the MDAE contents considered, D_w values are higher than those of D_s value. As indicated in the equation (3.6), the diffusion coefficients of larger penetrants (i.e. NaCl) vary more largely with changes in the free volume than those of smaller penetrants (i.e. water). Also, this phenomenon can be confirmed by fitting the plots using the equation (3.6), in which the slope of the line for the NaCl data is steeper

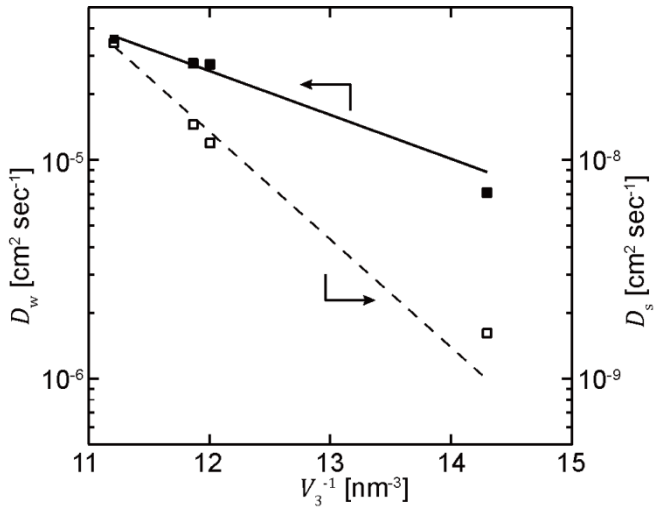

Figure 3-9 Correlation between water (■) or salt (□) diffusion coefficients, and free volume estimated by the PALS measurement. The solid and dotted lines were fitted for water and salt diffusivity, respectively, using the equations (3.6).

than that through the water data. The increase in $\langle v_f \rangle$ induced by the MDAE unit led to the larger enhancement of D_s than that of D_w. That is, the suppression of hydrogen bonding and incompatibility of the hydrophilic and hydrophobic polymer domain increase J_w, while lowering R of ultrathin membranes.

However, since it seems difficult to accurately control the free volume by designing the primary structure, it is necessary to develop another method for the adequate control over the free volume.

3.3 Conclusions

Partially *N*-methylated random aromatic coPAs (**PA-X-Ys**) composed of MDAE, DABA, and DAE units were successfully synthesized by the low temperature polycondensation. The **PA-X-Ys** showed the decrease in the *cis* conformation in the *N*-methyl amide linkage with increasing the MDAE unit in the polymer backbone. The total contents of the *cis* conformation, however, were maintained from 15 to 25 mol% for **PA-0-20**, **PA-20-20**, **PA-20-40**, and **PA-20-60**, promoting the formation of loosely-packed membranes. The incorporation of the *N*-methyl amide linkage into the polymer backbone affected the hydrogen bonding behavior of the amide linkage and the configurational behavior in solution, which led to suppressing the aggregation of the polymer chains during the membrane fabrication process. Since the polymers in the membranes were loosely packed, the obtained **PA-X-Y** membranes with the MDAE unit showed lower dry densities, higher free volume, and higher surface hydrophilicity than the PA membranes without the MDAE unit, resulting in an enhancement of water flux and depression of NaCl rejection due to a larger increase in salt diffusion coefficient than water one.

3.4 Experimental

3.4.1 Materials

4,4’-Diaminodiphenyl ether (DAE), isophthaloyl chloride (IPC), 3,5-diaminobenzoic acid (DABA), sodium methoxide (ca. 5M in CH_3OH), paraformaldehyde, and sodium borohydride were purchased from TCI, Japan. DAE was sublimed before use. IPC and DABA were purified by recrystallization before use. DAE was purified by sublimation prior to use. *N*-Methylpyrrolidone (NMP), triethylamine, potassium hydroxide, and methanol were purchased from Wako Pure Chemical Industries. NMP was dried over calcium hydride and distilled under nitrogen.

3.4.2 Synthesis of *N*,*N*’-dimethyl-4,4’-diaminodiphenyl ether (MDAE)

To a 500 mL two-necked round flask, DAE (8.01 g, 40.0 mmol), sodium methoxide (ca. 5 M in CH_3OH) (80.0 mL, 400 mL), and methanol (240 mL) were added under a nitrogen atmosphere. The solution was refluxed for 8 h. After cooling to room temperature, paraformaldehyde (3.36 g, 112 mmol) was added. The reaction mixture was refluxed for 12 h, sodium borohydride (3.0 g, 80.0 mmol) was added to this solution, and the reaction mixture was refluxed for 3 h. A 1 M NaOH aqueous solution (25.0 mL) was then added to the reaction mixture to hydrolyze the products in the solution and the reaction mixture was refluxed for 1 h. After evaporation of the solvent, the reaction mixture was extracted with chloroform. The organic layer was washed three times with brine, dried over $MgSO_4$, and the solvent was evaporated under vacuum. The residue was purified by silica gel column chromatography treated with triethylamine (eluent: ethyl acetate : hexane = 2 : 1) to give the crude product. Finally, the crude product was purified

by recrystallization from hexane and ethyl acetate to give MDAE as white crystals (2.92 g).

Yield: 32%. ^{1}H NMR (300 MHz, $CDCl_3$, δ, 25 °C): 6.87 (d, *J* = 8.9 Hz, Ar*H*, 4H), 6.57 (d, *J* = 8.9 Hz, Ar*H*, 4H), 3.52 (s, N*H*, 2H), 2.81 (s, N-CH_3, 6H). ^{13}C NMR (75 MHz, $CDCl_3$, δ, 25 °C): 150.32, 145.49, 119.91, 113.74, 31.79. IR (KBr) *v* (cm^{-1}): 3367 (N-H stretching), 2877 (C-H stretching), 1226 (C-O-C stretching).

3.4.3 Synthesis of a series of *N*-methylated PAs (PA-X-Ys)

A series of **PA-X-Y** were prepared by the low temperature solution polycondensation of IPC with DABA, MDAE, and DAE by controlling the feed molar ratio of the diamine monomers. The typical procedure (as an example for the PA6-20-60 copolymer) was as follows. Into a two-necked 50 mL flask, DABA (0.609 g, 4.00 mmol), MDAE (2.72 g, 12.0 mmol), DAE (0.801 g, 4.00 mmol), and NMP (31.8 mL) were added under a nitrogen atmosphere. After complete dissolution of the diamine monomers, the solvent was frozen by cooling to -78 °C. Subsequently, IPC (4.10 g, 20.0 mmol) was added to this solution and the reaction temperature was increased to room temperature after isophthaloyl chloride was completely dissolved. The solution was stirred for at least 8 h, and then precipitated with a large amount of methanol to give a white fibrous polymer. The obtained polymer was filtered off, washed several times with methanol, and dried in a vacuum oven for 24 h at 120 °C. (6.05 g)

PA-0-0: Yield 99 %. ^{1}H NMR (300 MHz, DMSO-d_6, δ, 40 °C): 10.41 (s, -N*H*, 2.0H), 8.54 (s, Ar*H*, 1.0H), 8.15 (d, *J* = 7.2 Hz, Ar*H*, 2.0H), 7.82 (d, *J* = 8.1 Hz Ar*H*, 4.0H), 7.69 (t, *J* = 6.6 Hz, Ar*H*, 1.0H), 7.05 (d, *J* = 7.2 Hz, Ar*H*, 4.0H). ^{13}C NMR (75 MHz, DMSO, δ,

40 °C): 165.0, 153.1, 136.3, 134.6, 130.7, 128.6, 127.0, 118.7. IR (Film) ν (cm^{-1}): 3065 (N-H stretching), 1654 (C=O stretching), 1533 (N-H in-plane bending).

PA-0-20: Yield 99 %. ^{1}H NMR (300 MHz, DMSO-d_6, δ, 100 °C): 9.88, 9.80 (s, -N*H*, 1.6H), 8.53 (s, Ar*H*, 0.8H), 8.13 (d, *J* = 7.7 Hz, Ar*H*, 1.6H), 7.90-7.62 (m, Ar*H*, 4.2H), 7.46-7.33 (m, Ar*H*, 0.6H), 7.19-6.99 (m, Ar*H*, 4.0H), 6.83 (d, *J* = 8.7 Hz, Ar*H*, 0.8H), 3.38, 3.28 (s, CH_3, 1.2H). IR (Film) ν (cm^{-1}): 3066 (N-H stretching), 2946 (aliphatic C-H stretching), 1655 (C=O stretching), 1527 (N-H in-plane bending).

PA-20-0: Yield 98 %. ^{1}H NMR (300 MHz, DMSO-d_6, δ, 40 °C): 10.69 (s, -N*H*, 0.4H), 10.48 (s, -N*H*, 1.6H), 8.70 (s, Ar*H*, 0.2H), 8.63-8.55 (m, Ar*H*, 1.0H), 8.18-8.12 (m, Ar*H*, 2.4H), 7.81 (d, *J* = 9.0 Hz, 3.2H), 7.72-7.65 (m, Ar*H*, 1.0H), 7.05 (d, *J* = 9.0 Hz, Ar*H*, 3.2H). IR (Film) ν (cm^{-1}): 1658 (C=O stretching), 1535 (N-H in-plane bending).

PA-20-20: Yield 99 %. ^{1}H NMR (300 MHz, DMSO-d_6, δ, 100 °C): 10.24, 10.00, 9.81 (s, -N*H*, 1.6H), 8.60-8.53 (s, Ar*H*, 1.0H), 8.19-8.12 (m, Ar*H*, 2.0H), 7.94-7.86 (m, Ar*H*, 0.6H), 7.80-7.62 (m, Ar*H*, 2.8H), 7.45-7.34 (m, Ar*H*, 0.6H), 7.16 (d, *J* = 8.8 Hz, Ar*H*, 0.8H), 7.06-6.99 (m, Ar*H*, 2.4H), 6.80 (d, *J* = 8.8 Hz, Ar*H*, 0.8H), 3.38, 3.28 (s, CH_3, 1.2H). IR (Film) ν (cm^{-1}): 3066 (N-H stretching), 2946 (aliphatic C-H stretching), 1659 (C=O stretching), 1531 (N-H in-plane bending).

PA-20-40: Yield 99 %. ^{1}H NMR (300 MHz, DMSO-d_6, δ, 100 °C): 10.22, 10.04, 9.99, 9.80 (s, -N*H*, 1.2H), 8.59-8.53 (s, Ar*H*, 0.8H), 8.19-8.12 (m, Ar*H*, 1.6H), 7.94-7.87 (m, Ar*H*, 0.4H), 7.80-7.64 (m, Ar*H*, 2.2H), 7.45-7.33 (m, Ar*H*, 1.2H), 7.17 (d, *J* = 8.8 Hz, Ar*H*, 1.6H), 7.06-6.99 (m, Ar*H*, 1.6H), 6.80 (d, *J* = 8.8 Hz, Ar*H*, 1.6H), 3.38, 3.28 (s, CH_3, 1.2H). IR (Film) ν (cm^{-1}): 3066 (N-H stretching), 2943 (aliphatic C-H stretching), 1650(C=O stretching), 1531 (N-H in-plane bending).

PA-20-60: Yield 90 %. ^{1}H NMR (300 MHz, DMSO-d_6, δ, 100 °C): 10.24, 10.08, 10.00, 9.82 (s, -N*H*, 0.8H), 8.62-8.54 (s, Ar*H*, 0.6H), 8.19-8.12 (m, Ar*H*, 1.2H), 7.97-7.87 (m, Ar*H*, 0.2H), 7.80-7.62 (m, Ar*H*, 1.6H), 7.45-7.33 (m, Ar*H*, 1.8H), 7.20-6.99 (m, Ar*H*, 3.2H), 6.84-6.77 (m, Ar*H*, 2.4H), 3.38, 3.28 (s, CH_3, 1.2H). IR (Film) v (cm^{-1}): 3066 (N-H stretching), 2931 (aliphatic C-H stretching), 1650 (C=O stretching), 1531 (N-H in-plane bending).

3.4.4 Preparation of ultrathin membranes

The 10 wt% solutions of the obtained **PA-X-Ys** were prepared in NMP. Subsequently, the polymer solutions were filtered through a 0.45 μm poly(vinylidene fluoride) membrane filter and coated onto a clean glass substrate by a spin-coating method to form the as-cast membranes with less than 2.0 μm thickness. The as-cast membranes were then heated at 70 °C for 30 min and at 200 °C for 1 h. The obtained membranes were peeled off from the glass substrate and stored in deionized water before use. Finally, the membranes were immersed in a 10 wt% isopropanol aqueous solution for 15 min and water for 15 min before evaluation of their membrane intrinsic properties.

3.4.5 Water permeation test

Membrane disks of 7 cm diameter were placed in the cross-flow filtration cells of custom-made equipment. Under an operating pressure of 7.5 bar to perform membrane filtration, a 500 mg L^{-1} aqueous solution of NaCl was supplied to the membranes. The temperature and pH of the feed solution were kept at 25 °C and 6.5, respectively. Subsequently, the feed and permeate water were sampled after the operation had been continued for more than 3 h to stabilize the membrane performance. Salt rejection rate (*R* value) was calculated based on the electrical conductivities of the feed and permeate water measured by a pH/EC meter WM-50EG (DKK-TOA Corp.). The flow rate of the solution was 3.5 L/min. Water flux (J_w, [L m^{-2} h^{-1}]), NaCl rejection (R, [%]), hydraulic water permeability (A, [L μm m^{-2} h^{-1} bar^{-1}]), and salt permeability (P_S, [cm^2/s]) are calculated from the following equations.

$$J_w = \frac{\Delta V}{S \Delta t} \quad (3.7)$$

$$R = \left(1 - \frac{C2}{C1}\right) \times 100 \quad (3.8)$$

$$A = \frac{J_w l}{\Delta P - \Delta \pi} \quad (3.9)$$

$$B = \frac{10^{-7}}{3600} \times J_w l \times \frac{C_2}{(C_1 - C_2)} = \frac{10^{-7}}{3600} \times J_w l \times \frac{100 - R}{R} \quad (3.10)$$

where ΔV [L] is the volume of permeate water, S [m^2] is the effective membrane area, Δt [h] is time during water permeation, C_1 and C_2 are the salt concentrations in the feed and permeate water, l [μm] is the membrane thickness, ΔP [bar] is pressure difference

across the membrane, and $\Delta\pi$ [bar] is osmotic pressure difference across the membrane. To clarify the relationships among *A*, *B*, and *R*, *R* is also expressed by the following equation: [49]

$$R = 100 \times \left(1 + \frac{B}{A(\Delta P - \Delta\pi)}\right)^{-1} \quad (3.11)$$

3.4.6 Determination of water sorption coefficient and water diffusion coefficient

Before the water uptake and dry density measurements, all of the **PA-X-Y** membranes were dried in vacuum oven at 120 °C for 2 days. Polymer densities (ρ_P, g cm^{-3}) were determined using an Alfa Mirage SD-200L electronic densimeter at ambient temperature (24-25 °C) using the following equation:

$$\rho_P = \frac{m_A}{m_A - m_L}\rho_o \quad (3.12)$$

where m_A and m_L are weights of the membrane measured in air and non-solvent, respectively, and ρ_o is density of the non-solvent. Ethanol was selected as the non-solvent. To estimate water uptake (ω_w), the dried membranes were immersed in deionized water at ambient temperature (24-25 °C) for 3 days after weight of the dried membranes (m_d) were measured. Then, weight of hydrated membranes (m_h) were measured. ω_w was calculated by the following equation:

$$\omega_w = \frac{m_h - m_d}{m_d} \quad (3.13)$$

From ω_w value, equilibrium volume fraction of water in the hydrated membrane (ϕ_w) was evaluated as follows:

$$\phi_w = \frac{\rho_p \omega_w}{\rho_p \omega_w + \rho_w} \quad (3.14)$$

where ρ_w is density of water (1.0 g cm^{-3}). Using ϕ_w value, water sorption coefficient (K_w) can be estimated, which is defined as the ratio of water concentration in the membrane (C_w^m) to that in the solution (C_w) ([g water/cm^3 hydrated membrane]/[g water/ cm^3 solution]) as shown in the following equation.[50]

$$K_W = \frac{C_w^m}{C_w} = \frac{\phi_w M_w}{\rho_w V_w} \quad (3.15)$$

where C_w is equal to density of pure water (ρ_w), M_w is the molecular weight of water, and V_w is the molar volume of water (18 cm^3/mol).[51]

Diffusive water permeability (P_w, [cm^2 s^{-1}]) was related to water permeability (A, [L μm m^{-2} h^{-1} bar^{-1}]) as follows:

$$P_w = A \times \frac{RT}{V_w} \times \frac{10^{-6}}{36} \quad (3.16)$$

where R is the ideal gas constant (8.314 J K^{-1} mol^{-1}) and T is the absolute temperature. Water diffusive coefficient (D_w, cm^2 s^{-1}) estimated from P_w and K_w based on the following equation:

$$D_w = \frac{P_w}{K_w} \quad (3.17)$$

3.4.7 Determination of NaCl sorption coefficient and NaCl diffusion coefficient

Salt partition coefficient (K_s) was determined by salt desorption into deionized water from the membrane previously equilibrated with 50 mL of 1.0 M NaCl aqueous solution by immersing into that solution for at least 3 days. K_s is calculated by the ratio of the mass in the membrane per unit volume to the concentration of NaCl in the original solution as follows:

$$K_S = \frac{M_\infty \rho_p}{m} \times \frac{1}{58.44 \times 10^{-3}} \quad (3.18)$$

where M_∞ is the total weight of salt desorbed from membrane, m is weight of membrane, ρ_p is polymer density. Salt diffusion coefficient (D_S) is estimated from the measured salt permeability (B value):

$$D_s = \frac{B}{K_s} \quad (3.19)$$

3.4.8 Measurements

The nuclear magnetic resonance (NMR) spectra were recorded on a Bruker DPX-300S spectrometer at the resonant frequencies of 300 MHz for ^{1}H and 75 MHz for ^{13}C nuclei using $CDCl_3$ or DMSO-d_6 as the solvents and tetramethylsilane as an internal standard (δ_H 0.00). The FT-IR spectra were measured on a Horiba FT-720 spectrometer. The inherent viscosities were measured at 30 °C in NMP at a polymer concentration of 0.5 g/dL. The thermal analysis (TGA) was performed on a Seiko TG/DTA 6300 thermal analysis system under a nitrogen atmosphere for thermogravimetry (TG) and differential thermal analysis (DTA). Before the evaluation, all the samples were preheated at 250 °C for 30 min to remove any moisture and residual solvents in the TG/DTA furnace. The samples were then cooled to 30 °C and heated to 500 °C at the heating rate of 10 °C/min. Time resolved water contact angles of water droplets on the prepared membranes were measured by the sessile drop method using a contact angle measurement system (DropMaster 500, Kyowa Interface Science). The volume of the water droplets for the measurements was 2.0 μL. All measurements were carried out at ambient temperature (24-25 °C). The dry densities of the dried membranes were determined using an Alfa

Mirage SD-200L electronic densimeter at ambient temperature (24-25 °C). The surface morphology was characterized using an atomic force microscopic (AFM, SPA400, SII Nanotechnology) in the phase contrast mode. Low-energy positron annihilation lifetime spectroscopy (PALS) was performed using a Fuji-imvac PALS-200A system at an incident positron energy of 7.0 keV. A multi-exponential analysis using the RESOLUTION code was applied to the obtained positron annihilation lifetime spectra to attain the average lifetime of the third component (τ_3) for the triplet *ortho*-positronium (*o*-Ps).

3.5 Reference

(1) Lawrence, D. S.; Jiang, T.; Levett, M. *Chem. Rev.* **1995**, *95*, 2229–2260.

(2) Germann, M. W.; Kalisch, B. W.; van de Sande, J. H. *Biochemistry* **1988**, *27*, 8302–8306.

(3) Hu, X.; Kaplan, D.; Cebe, P. *Macromolecules* **2006**, *39*, 6161–6170.

(4) Ishioka, Y.; Minakuchi, N.; Mizuhata, M.; Maruyama, T. *Soft Matter* **2014**, *10*, 965–971.

(5) Karle, I. L.; Balarams, P. *Biochemistry* **1990**, *29*, 6747–6756.

(6) García, J. M.; García, F. C.; Serna, F.; de la Peña, J. L. *Prog. Polym. Sci.* **2010**, *35*, 623–686.

(7) Espeso, J. F.; Lozano, A. E.; de la Campa, J. G.; Garcia-Yoldi, I.; de Abajo, J. *J. Polym. Sci. Part A Polym. Chem.* **2010**, *48*, 1743–1751.

(8) Tashiro, K.; Kobayashi, M.; Tadokoro, H. *Macromolecules* **1977**, *10*, 413–420.

(9) Yuan, L.; Zeng, H.; Yamato, K.; Sanford, A. R.; Feng, W.; Atreya, H. S.; Sukumaran, D. K.; Szyperski, T.; Gong, B. *J. Am. Chem. Soc.* **2004**, *126*, 16528–16537.

(10) Banavar, J. R.; Cieplak, M.; Hoang, T. X.; Maritan, A. *Proc. Natl. Acad. Sci. U. S. A.* **2009**, *106*, 6900–6903.

(11) Chen, Y. Y.; Wang, L.; Zhang, L.; Zhu, J.; Wang, H.; Zhang, D. W.; Li, Z. T. *Tetrahedron* **2014**, *4*, 4–8.

(12) Schulze, M.; Michen, B.; Fink, A.; Kilbinger, A. F. M. *Macromolecules* **2013**, *46*, 5520–5530.

(13) Seyler, H.; Berger-Nicoletti, E.; Kilbinger, A. F. M. *J. Mater. Chem.* **2007**, *17*, 1954–1957.

(14) Itai, A.; Toriumi, Y.; Saito, S.; Kagechika, H.; Shudo, K. *J. Am. Chem. Soc.* **1992**, *114*, 10649–10650.

(15) Burch, R. R.; Manring, L. E. *Macromolecules* **1991**, *24*, 1731–1735.

(16) Azumaya, I.; Kagechika, H.; Yamaguchi, K.; Shudo, K. *Tetrahedron* **1995**, *51*, 5277–5290.

(17) Shi, H.; Zhao, Y.; Zhang, X.; Zhou, Y.; Xu, Y.; Zhou, S.; Wang, D.; Han, C. C.; Xu, D. *Polymer* **2004**, *45*, 6299–6307.

(18) Yokozawa, T.; Asai, T.; Sugi, R. **2000**, 8313–8314.

(19) Tanatani, A.; Yokoyama, A.; Azumaya, I.; Takakura, Y.; Mitsui, C.; Shiro, M.; Uchiyama, M.; Muranaka, A.; Kobayashi, N.; Yokozawa, T. *J. Am. Chem. Soc.* **2005**, *127*, 8553–8561.

(20) Fujimori, A.; Chiba, S.; Sato, N.; Abe, Y.; Shibasaki, Y. *J. Phys. Chem. B* **2010**, *114*, 1822–1835.

(21) Shibasaki, Y.; Abe, Y.; Sato, N.; Fujimori, A.; Oishi, Y. *Polym. J.* **2010**, *42*, 72–80.

(22) McKinney, R.; Rhodes, J. H. *Macromolecules* **1971**, *4*, 633–637.

(23) Mohamed, N. A. *Polymer* **1997**, *38*, 4705–4713.

(24) Lee, K. P.; Arnot, T. C.; Mattia, D. *J. Memb. Sci.* **2011**, *370*, 1–22.

(25) Gin, D. L.; Noble, R. D. *Science* **2011**, *332*, 674–676.

(26) Ikeda, A.; Tsubata, A.; Kameyama, A.; Nishikubo, T. *J. Polym. Sci. Part A Polym. Chem.* **1999**, *37*, 917–926.

(27) Hodge, R. M.; Edward, G. H.; Simon, G. P. *Polymer* **1996**, *37*, 1371–1376.

(28) Park, S. B.; Kim, H.; Zin, W. C.; Jung, J. C. *Macromolecules* **1993**, *26*, 1627–1632.

(29) Kim, H.; Park, S. B.; Jung, J. C.; Zin, W. C. *Polymer* **1996**, *37*, 2845–2852.

(30) Geise, G. M.; Lee, H.; Miller, D. J.; Freeman, B. D.; Mcgrath, J. E.; Paul, D. R. *J. Polym. Sci. Part B Polym. Phys.* **2010**, *48*, 1685–1718.

(31) Xie, G.; Pino, P.; Lorenzil, G. P. *Macromolecules* **1990**, *23*, 2583–2588.

(32) Yamauchi, K.; Kuroki, S.; Fujii, K.; Ando, I. *Chem. Phys. Lett.* **2000**, *324*, 435–439.

(33) Xie, W.; Ju, H.; Geise, G. M.; Freeman, B. D.; Mardel, J. I.; Hill, A. J.; McGrath, J. E. *Macromolecules* **2011**, *44*, 4428–4438.

(34) Lee, C. H.; VanHouten, D.; Lane, O.; McGrath, J. E.; Hou, J.; Madsen, L. a.; Spano, J.; Wi, S.; Cook, J.; Xie, W.; Oh, H. J.; Geise, G. M.; Freeman, B. D. *Chem. Mater.* **2011**, *23*, 1039–1049.

(35) Eisenbach, C. D.; Hofmann, J.; Goldel, A.; Noolandi, J.; Shi, A. C. *Macromolecules* **1999**, *32*, 1463–1470.

(36) Flory, J. *Macromolecules* **1978**, *11*, 1138–1141.

(37) Skrovanek, D. J.; Howe, S. E.; Painter, P. C.; Coleman, M. M. *Macromolecules* **1985**, *18*, 1676–1683.

(38) Kim, Y. J.; Lee, K. S.; Jeong, M. H.; Lee, J. S. *J. Memb. Sci.* **2011**, *378*, 512–519.

(39) Horinouchi, A.; Tanaka, K. *RSC Adv.* **2013**, *3*, 9446–9452.

(40) Oda, Y.; Horinouchi, A.; Kawaguchi, D.; Matsuno, H.; Kanaoka, S.; Aoshima, S.; Tanaka, K. *Langmuir* **2014**, *30*, 1215–1219.

(41) Horinouchi, A.; Atarashi, H.; Fujii, Y.; Tanaka, K. *Macromolecules* **2012**, *45*, 4638–4642.

(42) Eldrup, M.; Lightbody, D.; Sherwood, J. N. *Chem. Phys.* **1981**, *63*, 51–58.

(43) Tao, S. J. *J. Chem. Phys.* **1972**, *56*, 5499.

(44) Sodaye, H. S.; Pujari, P. K.; Goswami, A.; Manohar, S. B. *J. Polym. Sci. Part A Polym. Chem.* **1997**, *35*, 771–776.

(45) Cohen, M. H.; Turnbull, D. *J. Chem. Phys.* **1959**, *31*, 1164.

(46) Nightingale, E. R. *J. Phys. Chem.* **1959**, *63*, 1381–1387.

(47) Shi, G. M.; Chen, H.; Jean, Y. C.; Chung, T. S. *Polymer* **2013**, *54*, 774–783.

(48) Lue, S. J.; Tsai, C. L.; Lee, D. T.; Mahesh, K. P. O.; Hua, M. Y.; Hu, C. C.; Jean, Y. C.; Lee, K. R.; Lai, J. Y. *J. Memb. Sci.* **2010**, *349*, 321–332.

(49) Cath, T.; Childress, a; Elimelech, M. *J. Memb. Sci.* **2006**, *281*, 70–87.

(50) Geise, G. M.; Park, H. B.; Sagle, A. C.; Freeman, B. D.; McGrath, J. E. *J. Memb. Sci.* **2011**, *369*, 130–138.

(51) Xie, W.; Cook, J.; Park, H. B.; Freeman, B. D.; Lee, C. H.; McGrath, J. E. *Polymer* **2011**, *52*, 2032–2043.

Chapter 4

Effect of Cross-linking Reaction of *N*-Substituted Polybenzimidazole Membranes on Water Transport Properties

4.1 Introduction

Polybenzimidazole (PBI) is expected to be one of the alternative membrane materials because of its high water absorbability, mechanical properties, thermal stability, and chemical stability over a wide range of pH. Additionally, PBIs having a strong base dissociation constant (pK_b = 5.5) become self-charged in an aqueous environment, because an adjacent benzene ring delocalizes the proton of the imidazole group.[1] Meanwhile, the hydrogen bonding between the imidazole rings is so strong that the PBI membranes become dense and show low water transport properties.[2] Therefore, it is necessary to suppress the polymer/polymer interaction and to disrupt the polymer chain packing for the enhancement in water permeability of PBI.[3] It is well known that the suppression of the hydrogen bonding in the amide linkage of aromatic condensation

polymers affects the interplanar spacing, the crystallinity, the solubility, and the transport properties.[4–7] In chapter 3, it was revealed that the incorporation of the *N*-methyl amide linkage into the aromatic PA membranes suppress hydrogen bonding, prevented the polymer chain packing, and increased water flux while it decreased salt rejection. In the case of PBI, Kharul et al. have reported that the *N*-substitution of the PBI designed for suppressing the hydrogen bonding and for inhibiting the polymer chain packing enhanced the permeability for various gases because of an increase in the diffusivity.[8] Therefore, the *N*-substitution of PBI would be an effective way to increase water permeability.

In addition, it is generally accepted that the chemical cross-linking usually induces an enhancement of the selectivity and a decrease in the permeability.[9,10] For example, Wang et al. reported the cross-linking of PBI membranes by *p*-xylylene dichloride improved the NaCl rejection while decreasing the water flux due to the formation of smaller pores induced by the high cross-linking density.[11] However, this expectation is not always acceptable and there would be the improvement of the selectivity without the depression of permeability. Indeed, the cross-linking of some polyimides applied for the gas permeable membranes can increase in the permeability without sacrificing the selectivity.[12,13] As discussed in the previous report by Lee et al., the improvement of the gas permeability with maintaining the gas selectivity was achieved in the cross-linked and thermally-rearranged polybenzoxazole-*co*-imide membranes, wherein the increase in the pore radius (from 0.82 to 0.97 nm) was induced by the suppression of the hydrogen bonding among cross-linked polymer chains.[14] Besides, we have concluded in chapter 3 that it seems difficult to obtain the effective pathway for water molecules just by the *N*-substitution. Thus, we expected that the

introduction of the cross-linked structure into PBI membranes during the desolvation process of membrane fabrication would improve the water permeability without decreasing the selectivity by formation of appropriate water channel with reduction of hydrogen bonding. On the basis of these previous reports, 50% of the -NH- groups in the imidazole rings of PBI were substituted to butyl or butylsulfonate groups to suppress the hydrogen bonding and to compare the effects of the hydrophilicity on water and NaCl transport properties with pristine PBI. Furthermore, the PBI was cross-linked with divinyl sulfone during the desolvation process of membrane fabrication, which is expected to make polymer/polymer interaction weaker.

In this chapter, we report the development of ultrathin membrane based on cross-linked PBI. In addition, the effects of the *N*-substitution as well as cross-linking of PBI on water and NaCl transport properties are described in detail. The cross-linking reaction of the *N*-substituted PBI led to the change of the pore size distribution from unimodal (0.25-0.33 nm) to bimodal (0.15-0.24 nm and 0.25-0.37 nm), where the selective permeation of water molecule was successfully achieved.

4.2 Result and discussion

4.2.1 Synthesis and characterization

N-butylsufonated and *N*-butylated PBIs (**BSPBI** and **BPBI**) were synthesized by the two steps, that is, deprotonation of PBI using lithium hydride, followed by treatment with 1,4-butanesultone or 1-bromobutane (**Scheme 4-1**). The ^{1}H NMR spectra of **PBI**, **BSPBI**, and **BPBI** along with the assignments are shown in **Figure 4-1**. After the *N*-substitution reaction of **PBI**, the peaks of the imidazole protons in **BSPBI** and **BPBI** become smaller compared to that of **PBI**, indicating the progress of *N*-substitution in the polymer main chain. The peaks due to the characteristic aromatic protons appear in the range of 7.6 to 9.2 ppm. Whereas, the signals at 4.3 and 4.4 ppm are assigned to the methylene protons attached to imidazole nitrogen atoms in **BSPBI** and **BPBI** (denoted as A and A'). The signals of the other protons for butyl and butyl sulfonate chains appear at 1.9, 1.8, 1.4, 1.7, and 0.8 ppm for B, D, C, B', C', and D', respectively. As the aromatic peak patterns of **BSPBI** and **BPBI** are too complicated to identify the ratio of the disubstituted unit (x) and the monosubstituted unit (y) in the repeating unit, the degree of substitution was estimated as the total of *N*-substitution. The degree of substitution (x + y) was calculated based on the integral ratio of the aromatic and the methylene proton peaks are denoted as A and A'. Both of **BSPBI** and **BPBI** possess about 50 % degree of *N*-substitution. The inherent viscosity (η_{inh}) measurements of BSPBI and BPBI were carried out at a concentration of 0.5 g dL^{-1} in DMSO at 30 °C and the results are summarized in **Table 4-1**. All of the η_{inh} values indicate the formation of high molecular weight polymers.

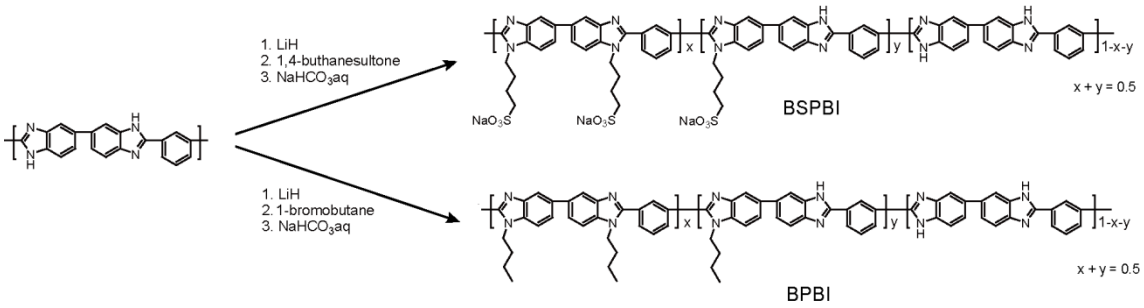

Scheme 4-1 Synthesis of **BSPBI** and **BPBI** by the post-functionalization reaction.

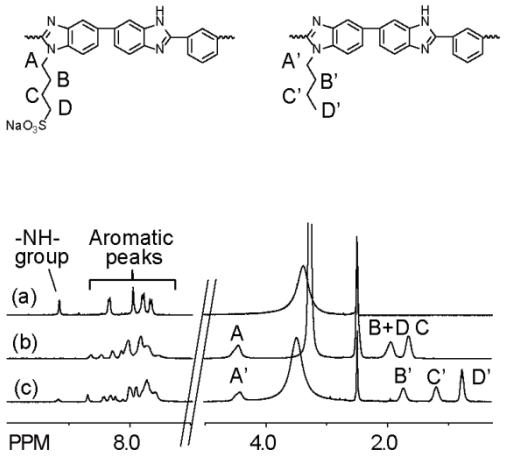

Figure 4-1 The ^{1}H NMR spectra of the (a) **PBI**, (b) **BSPBI**, and (c) **BPBI** in DMSO-d_6 at 40 °C.

4.2.2 Preparation of the uncross-linked and cross-linked PBI membranes.

All of the ultrathin membranes with about 2.0 μm thickness were prepared by the spin-coating method. The cross-linked membranes (**CL-BSPBI** and **CL-BPBI**) were successfully prepared by the reaction between divinyl sulfone and the -NH- groups of the imidazole rings as shown in Scheme 4-2. The obtained **CL-BSPBI** and **CL-BPBI** were insoluble in DMSO, indicating that the cross-linking reaction was successfully occurred. **Table 4-1** summarizes the properties of PBI membranes. Dry densities (ρ_P) of the PBI membranes were measured for the estimation of the free volume which affects the water and NaCl transport properties. By the *N*-butylation of PBI, the ρ_P value apparently decreases from 1.294 (g cm^{-3}) to 1.209 (g cm^{-3}). On the other hand, the ρ_P value of BSPBI increases, which would be due to the high molecular weight of the sulfonate group. The **BSPBI** possessing the hydrophilic sulfonate groups shows higher water uptake (ω_w) than **PBI**. The decrease in the hydrophilicity of **BPBI** would be due to its hydrophobic nature of the butyl group and the loss of the self-charged property. All the PBIs show high thermal stabilities with the high 5 % weight loss temperatures ($T_{d5\%}$) over 400 °C.

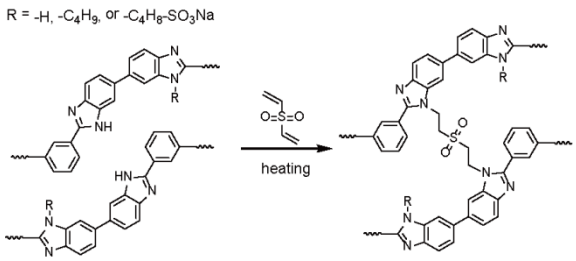

Scheme 4-2 The cross-linked reaction between the imidazole rings by divinyl sulfone.

Table 4-1 Inherent viscosities, dry densities, and water uptake of PBIs

		PBI	BPBI	CL-BPBI	BSPBI	CL-BSPBI
η_{inh} [a]	[g dL^{-1}]	1.00	0.96	-	1.78	-
ρ_p [b]	[g cm^{-3}]	1.294 ± 0.007	1.209 ± 0.006	1.218± 0.007	1.368 ± 0.003	1.378 ± 0.009
ω_w [c]	[%]	11.5	8.8	10.5	49.4	50.0

[a]Evaluated at 30 °C in NMP at a concentration of 0.5 g dL^{-1}. [b]Measured at ambient temperature 24-25 °C in ethanol. [c]Measured by immersing into deinonized water for 3 days.

4.2.3 The molecular aggregation structure of PBI membranes

4.2.3.1 FTIR spectra

In order to evaluate the hydrogen bonding behavior in the membrane, FTIR spectra of all samples were measured (**Figure 4-2**). The strong and broad peaks from 3000 cm^{-1} to 3500 cm^{-1} are attributed to two kinds of stretching vibrations of the N-H groups of the imidazole rings, such as the hydrogen bonded N-H groups around 3200 cm^{-1} and the isolated non-hydrogen bonded N-H groups around 3415 cm^{-1} (denoted as *v*(h-NH) and *v*(i-NH)). For example, the peaks at 3387 cm^{-1} and 3145 cm^{-1} of **PBI** are corresponding to *v*(i-NH) and *v*(h-NH), respectively.[11] Among the uncross-linked PBI membranes, a strong peak of *v*(h-NH) is exceptionally observed for **PBI**, indicating that the *N*-substitution of **PBI** suppresses the hydrogen bonding among the imidazole rings. Both of **BSPBI** and **BPBI** show the strong peaks of *v*(i-NH) at 3388 cm^{-1} and 3387 cm^{-1}, respectively. On the other hand, in **CL-BSPBI** and **CL-BPBI** membranes, the strong peaks of *v*(i-NH) are shifted to higher wave numbers than those of **BSPBI** and **BPBI**. This observation indicates that the introduction of the cross-linked structure suppresses the hydrogen bonding formation in PBI.

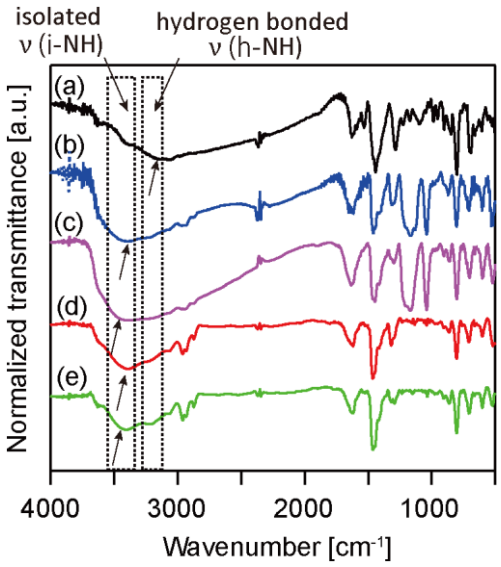

Figure 4-2 FTIR spectra of the PBI membranes: (a) **PBI**, (b) **BSPBI**, (c) **CL-BSPBI**, (d) **BPBI**, and (e) **CL-BPBI**.

4.2.3.2 WAXD analysis

Next, the *d*-spcaings (d_{sp}) were determined by WAXD analysis to evaluate the molecular aggregation structure in the membranes. As shown in **Figure 4-3**, WAXD analysis indicates the amorphous nature of all PBIs. Before cross-linking, the *N*-substitution increases the mean d_{sp} values in the order of **BSPBI** (0.407 nm) > **BPBI** (0.384 nm) > **PBI** (0.367 nm). This result indicates that the bulky butyl sulfonate group effectively reduces the intermolecular interaction. Additionally, the increase in the mean d_{sp} values of **CL-BSPBI** and **CL-BPBI** are also confirmed compared to non-cross-linked PBIs, which are in good accordance with the FTIR measurements. From these observations, it is confirmed that the suppression of the hydrogen bonding induced by the *N*-substitution and the cross-linked structure led to the polymer packing disruption.

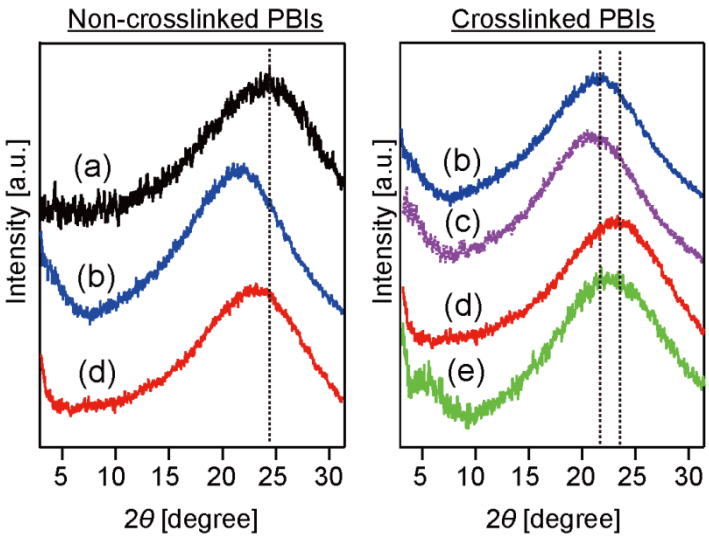

Figure 4-3 WAXD patterns of the PBI membranes: (a) **PBI**, (b) **BSPBI**, (c) **CL-BSPBI**, (d) **BPBI**, and (e) **CL-BPBI**.

4.2.3.3 Time-resolved water contact angle measurements

Prior to the measurements, the root-mean-square roughness (R_{RMS}) of all PBIs were measured by atomic force microscopy (AFM). The R_{RMS} values for all the membranes were ranged from 0.1 to 0.8 nm, indicating that the contact angle values were not mainly affected by the surface roughness. Time-resolved water contact angle measurements of all PBI membranes were carried out to evaluate the surface hydrophilicity and surface reorientation behavior (**Figure 4-4**). All membranes showed two regions (i.e. an initial exponential decay and the following linear line). On the basis of the previous report, the experimental plot for the time-resolved water contact angles were fitted by the following equation:[15]

$$\theta(t) = (\theta_{ini} - \theta_{ter})\exp\left(-\frac{t}{\tau}\right) - kt + \theta_{ter} \quad (4.1)$$

where θ_{ini} and θ_{ter} are the initial and terminal values of the contact angles at t=0 and in a quasi-equilibrium state, τ is the time constant of the contact angle decay in the initial stage, and k is the constant related to water evaporation, respectively.

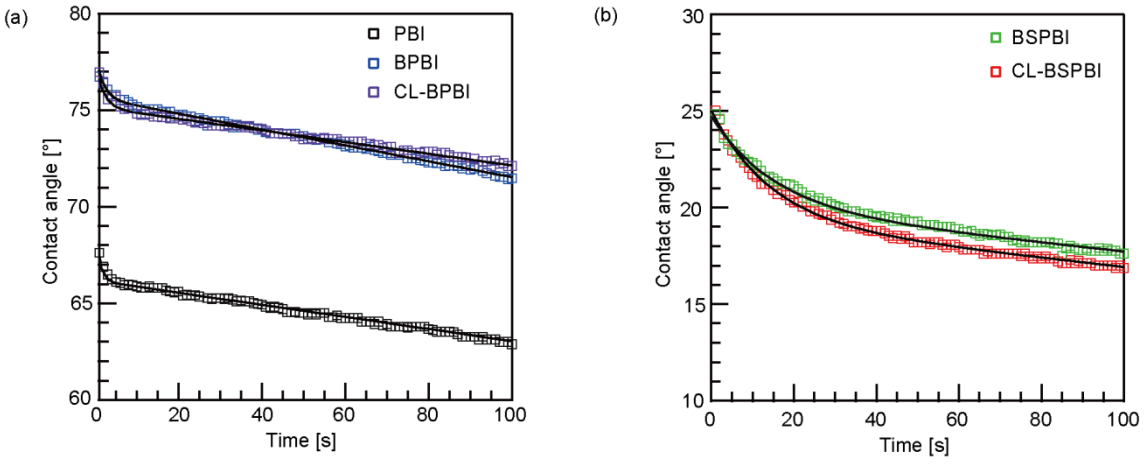

Figure 4-4 Time-resolved static water contact angle measurement of (a) **PBI**, **BPBI**, and **CL-BPBI**, and (b) **BSPBI** and **CL-BSPBI**.

The θ_{ini}, θ_{ter}, and τ values are summarized in Table 4-2. Especially, small surface reorganization with the difference in the θ_{ini} and θ_{ter} (i.e. the degree of surface reorganization induced by the water) values from 2.3 to 2.7 and τ values (i.e. the relaxation time of the interfacial mobility) from 1.07 to 1.89 were observed, although there is no hydrophilic groups in **PBI**, **BPBI**, and **CL-BPBI**. This reorganization behavior would be attributed to the active proton in the imidazole rings. Meanwhile, **BSPBI** and **CL-BSPBI** with hydrophilic sulfonate groups showed a larger difference in the θ_{ini} and θ_{ter} values (4.7°) and relatively longer τ values (14.4 and 15.1 s) than those of **PBI**, **BPBI**, and **CLBPBI**, indicating that large numbers of sulfonate groups were oriented toward the polymer/water interface. Also, it is noted that the θ_{ter} and τ values of **CL-BSPBI** are smaller than those of **BSPBI**, in spite of almost the same θ_{ini} values. Similar to the observation of FTIR spectra and WAXD measurement, this observation also implies that the cross-linking reaction induced the suppression of the polymer/polymer interaction even at the membrane surface.

Table 4-2 θ_{ini}, θ_{ter}, and τ values of all PBI membranes.

		PBI	BPBI	CL-BPBI	BSPBI	CL-BSPBI
θ_{ini}[a]	[°]	68.9	77.5	77.9	24.7	25.0
θ_{ter}[a]	[°]	66.2	75.2	75.6	20.0	19.3
τ[a]	[s]	1.07	1.88	1.89	15.1	14.4

[a]Time-resolved contact angle measurement was carried out by using the sessile drop method with water droplt of 2.0 μL.

4.2.3.4 AFM observations

Figure 4-5 represents the tapping mode phase images of the surface of the **BPBI**, **CL-BPBI**, **BSPBI**, and **CL-BSPBI** recorded under ambient conditions on 250 × 250 nm^2 size scales by AFM measurements. Nanoscaeld phase separations are clearly observed for all PBI membranes. In **BPBI** and **CL-BPBI** membranes, the dark and bright regions are attributed to the soft segments corresponding to the *N*-butylated PBI units and the hard segments corresponding to the nonsubstituted PBI units, respectively, indicating the low miscibility of the *N*-butylated and nonsubstituted PBI units. The **BSPBI** and **CL-BSPBI** membranes showed the dark and bright regions derived from the soft segments corresponding to the *N*-butyl sulfonated PBI units and the hard segments corresponding to the nonsubstituted PBI units, respectively. However, there could not be seen in any differences between cross-linked and uncross-linked membranes.

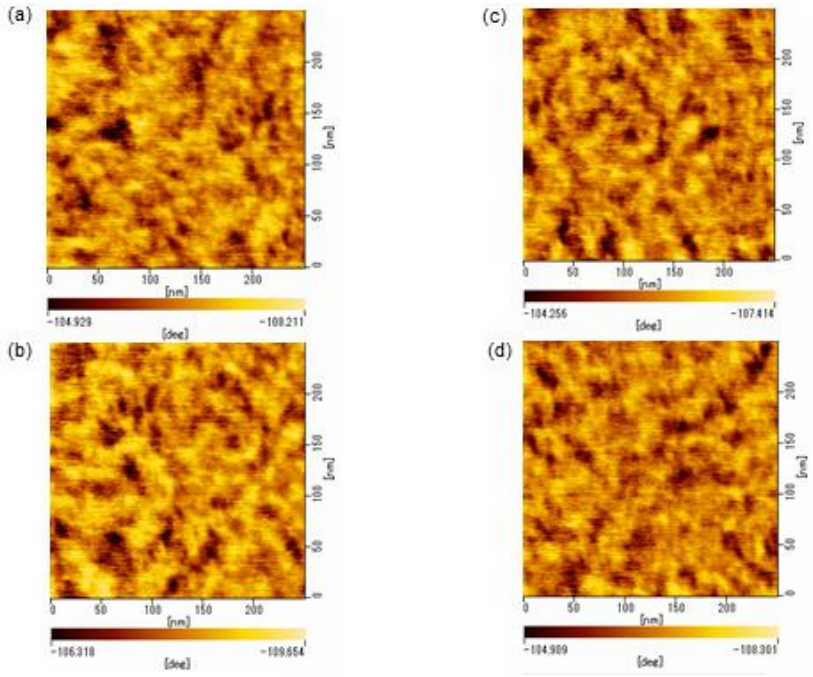

Figure 4-5 AFM tapping mode phase images of (a) **BPBI**, (b) **CL-BPBI**, (c) **BSPBI**, and (d) **CL-BSPBI** membranes. Scan sizes are 250 × 250 nm^2.

4.2.3.5 PALS

Since it was difficult to evaluate free volume from the WAXD patterns due to the amorphous nature of all PBI membranes, free-volume hole radii (r_3) distribution for the PBI membranes were estimated using the PALS and the results were shown in **Figure 4-6**. By the calculation of the *ortho* positronium (o-Ps) lifetime (τ_3) using the RESOLUTION code of the PATFIT package to obtain the positron lifetime spectra, r_3 was determined by the Tao-Eldrup model;[16,17]

$$\tau_3^{-1} = 2\left\{1 - \frac{r_3}{r_3 + 0.166} + \frac{1}{2\pi}\sin\left(\frac{2\pi r_3}{r_3 + 0.166}\right)\right\} \quad (4.2)$$

The r_3 distribution was calculated by the MELT anlysis.[18] However, since the sulfonate groups as electron withdrawing moieties prevent the formation of o-Ps,[19] the relative intensity value in **Figure 4-6** would be not correlated with the density of the r_3. The r_3 distribution increases in the order of **PBI** < **BPBI** < **BSPBI**, which is consistent with the WAXD results. By cross-linking, the pore radius distributions of **BSPBI** and **BPBI** membranes change from unimomodal (pore radius: 0.25-0.33 nm) to bimodal (pore radius: 0.14-0.24 nm and 0.26-0.38 nm).

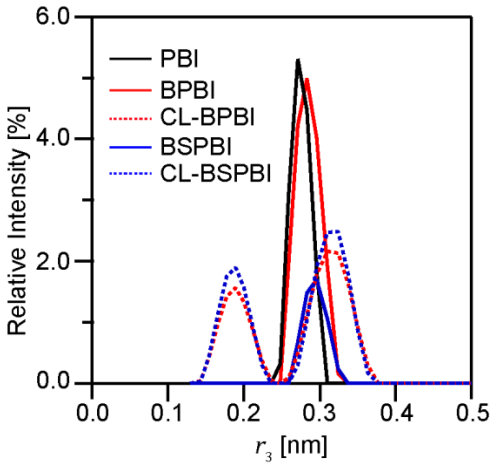

Figure 4-6 The r_3 distributions of the PBI membranes using the PALS measurements.

4.2.4 Proposed mechanism for the formation of bimodal free-volume hole distribution

A low-molecular-weight model system reaction as shown in Scheme 4-3 was conducted in order to study the cross-linking reaction of benzimidazole groups with divinyl sulfone in detail. To quantify the reaction rate constant ratio ($\kappa = k_2/k_1$), where k_1 and k_2 are the reaction rate constants for the first and second reaction steps, respectively, the kinetics was examined according to a previously reported method.[20] The ^{1}H NMR spectra of the crude product obtained by the model reaction are representatively shown in Figure 4-7, where it can be seen that the mono- and di-substituted compounds (**3** and **4**) are formed after heating at 70 °C for 2 h.

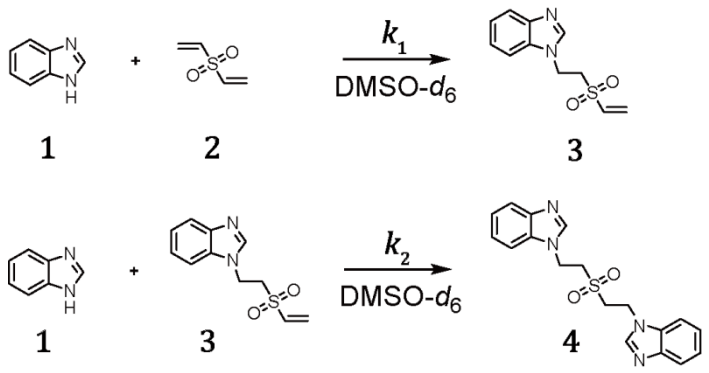

1 2 3 1 3 4

Scheme 4-3 1:1 model reaction between benzimidazole (**1**) and divinyl sulfone (**2**)

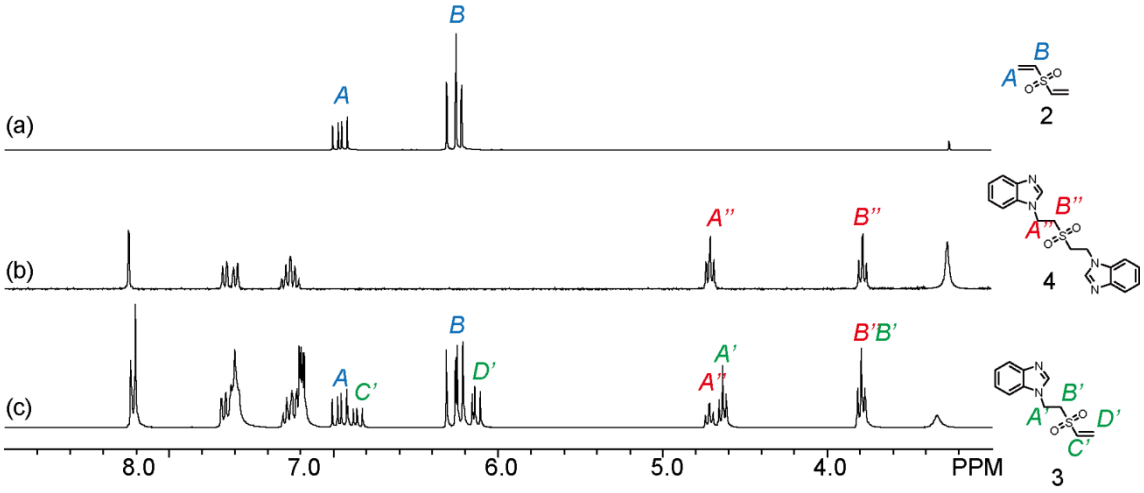

Figure 4-7 ^{1}H NMR spectra of (a) 2, (b) 4, and (c) the crude products obtained by the model reaction of **1** and **2** in DMSO-d_6 at 70 °C for 2 h.

As a result, κ was estimated to be 1.3, indicating that there is almost no difference in the rate constant between the first and second reaction steps. On the basis of previous reports, k_1 and k_2 values at 70 and 200 °C were calculated and summarized in **Table 4-3**.[21] Also, k_1 and k_2 values at 200 °C were about double digit higher than those at 70 °C.

Table 4-3 The reaction rate constants of the model reaction at 70 and 200 °C.

Temperature [°C]	k_1 [L mol^{-1}]	k_2 [L mol^{-1}]
70	1.63×10^{-3}	2.12×10^{-3}
200	4.10×10^{-1}	5.33×10^{-1}

To investigate the effect of the thermal treatment during the desolvation stage of membrane fabrication process on r_3 and the distribution of free volumes, PALS measurements were carried out for **CL-BSPBI** membranes fabricated via three kinds of different thermal treatments: (1) 70 °C for 30 min and 200 °C for 1h (**CL-BSPBI-70-200**), (2) 70 °C for 30 min (**CL-BSPBI-70**), and (3) 200 °C for 1h (**CL-BSPBI-200**). After the respective heating process, the membranes were dried under vacuum at room temperature for 2 days. **Table 4-4** summarizes the PALS results of these membranes. Although the reaction rate constants for the first (k_1) and the second (k_2) reaction steps at 200 °C are two orders of magnitude higher than those at 70 °C, there could not be seen significant differences in the r_3 values of the **CL-BSPBI-70** and **CL-BSPBI-200**. This can be explained by the assumption that the formation of larger pores is determined not only by kinetics of cross-linking reaction but also by kinetics of heat-induced aggregation of polymer chains during the solvation process.

Table 4-4 PALS results for **CL-BSPBIs** prepared via different thermal treatments.

Samples	Thermal treatment	Distribution	τ_3[a] [ns]	r_3[b] [nm]
CL-BSPBI-70	70 °C for 30 min	Monomodal	2.16±0.01	0.303±0.01
CL-BSPBI-200	200 °C for 1 h	Monomodal	2.25±0.01	0.311±0.01
CL-BSPBI-70-200	70 °C for 30 min, 200 °C for 1 h	Bimodal	1.00±0.01 2.17±0.01	0.187±0.01 0.304±0.01

[a]τ_3 was estimated by analyzing the PALS spectrum using the POSITRON fit. [b]r_3 was detemined by Tao-Endrup equation.

Also, it should be noted that the r_3 distributions of **CL-BSPBI-70** and **CL-BSPBI-200** are monomodal curves, as shown in Figure 4-8. We hypothesize that the competition between the cross-linking and the evaporation rate of the casting solvent would play an important role in determining the r_3 distribution. **Figure 4-9** represents the overall schematic image of the polymer chain and cross-linker behaviors over the membrane fabrication process.

For **CL-BSPBI-200** and **CL-BSPBI-70**, the cross-linking reaction would proceeds during the heat-induced desolvation process. Then, the desolvated mebranes are completely dried under vacuum for 24 h and only larger r_3 elements were formed due to the competitive effect of cross-liking reaction and heat-induced aggregation of polymer chains. On the other hand, for **CL-BSPBI-70-200**, a large part of the cross-linker still remains after the desolvation at 70 °C for 30 min and the smaller r_3 elements are constructed due to the partial shrinkage by cross-linking in the successive heating treatment at 200 °C for 1 h.

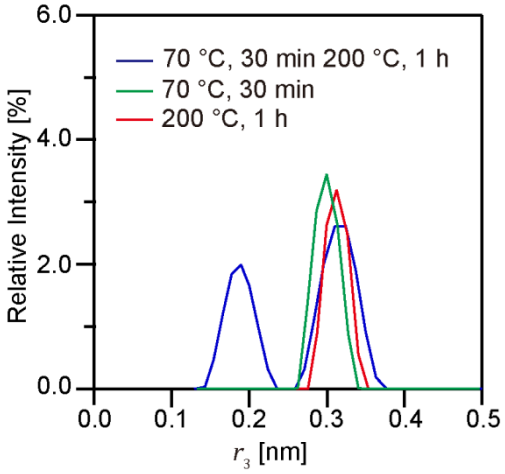

Figure 4-8 The r_3 distributions of the CL-BSPBI membranes fabricated via different thermal treatments using the PALS measurements.

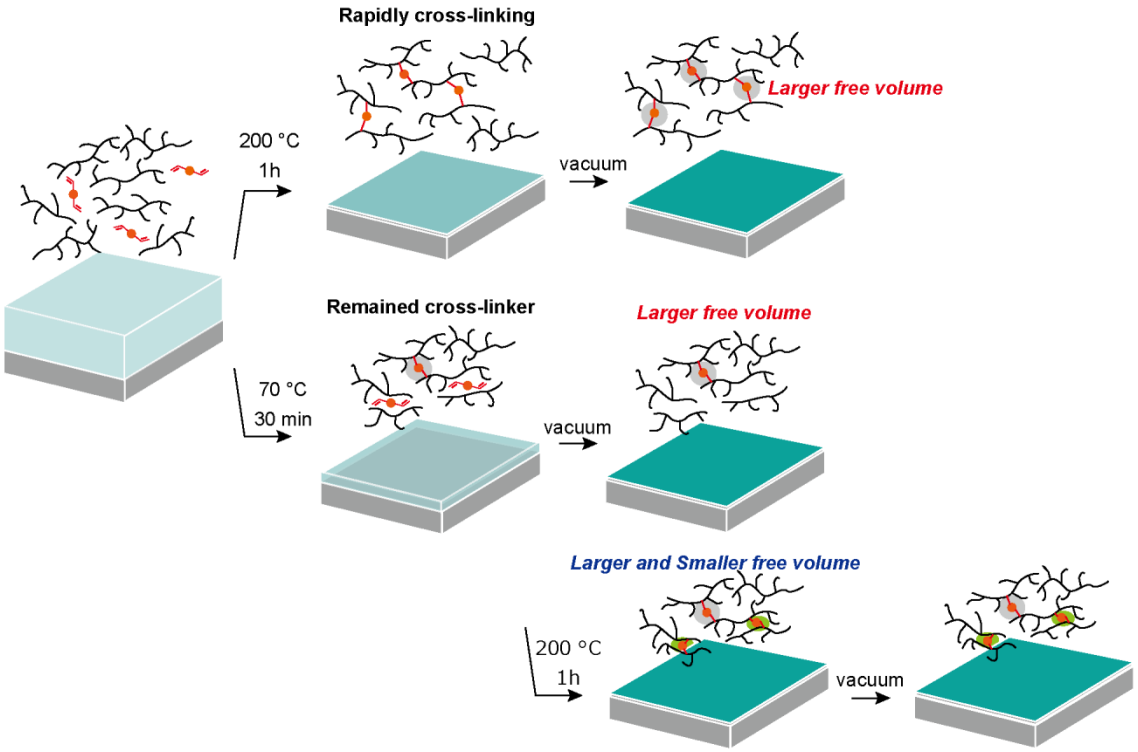

Figure 4-9 Schematic image of the polymer chain and cross-linker behaviors during the membrane fabrication process.

4.2.5 Water and NaCl transport properties

The effects of the *N*-substitution of PBI and the crosslinking on transport properties were evaluated using the instruments in the RO mode at an applied pressure of 7.5 bars, and the results are summarized in **Table 4-5**. Unlike the wholly aromatic polyamides, water permeation of **PBI** and **BPBI** was occurred without introducing the hydrophilic groups. Although the replacement of 50% of the active -NH- protons of the imidazole rings leads to the suppression of polymer/polymer interactions and increase in the D_w value, **BPBI** shows the same J_w and the A values, and low R value due to the loss of the charged property. In the case of **BSPBI**, the J_w and A values increase because the introduction of the hydrophilic sulfonate group enhances the K_w value. On the other hand, the introduction of the cross-linked structure of **BPBI** and **BSPBI** enhances both of J_w and R values. Especially, **CL-BSPBI** significantly improved the J_w (22.1 L m^{-2} h^{-1}), A (6.24 L μm m^{-2} h^{-1} bar^{-1}), and R values (46 %) compared to **BSPBI** (J_w : 1.88 L m^{-2} h^{-1}, A : 0.530 L μm m^{-2} h^{-1} bar^{-1}, R : 11 %) with suppressing the increase in the B value. Although **CL-BSPBI** and **BSPBI**, and **CL-BPBI** and **BPBI** show almost the same K_w values, there is a large difference in the D_w values between the cross-linked and uncross-linked PBI membranes because the cross-linking induces a lower packing density and a change of the pore radius distribution. According to the free volume theory, the small molecule diffusion coefficient is correlated to the free volume and the hydrated size of the molecule as the following equation.[22]

$$D_i = a_i \exp\left(-\frac{b_i}{\langle v_f \rangle}\right) \quad (4.3)$$

where a_i is the constant, b_i is the constant related to the hydrated size of the penetrant, and the $\langle v_f \rangle$ is the polymer's average free volume. Thus, when the size of the penetrant

molecule is increased, the effect of the change of the $\langle v_f \rangle$ value on the diffusion coefficient becomes more substantial. The effective radius of Na^+ (0.358 nm) and Cl^- (0.332 nm) are larger than that of H_2O molecule (0.138 nm).[23] Therefore, the D_w value is less influenced by the change of the free volume than the diffusion coefficient of NaCl.[24] The partial formation of larger pores in the membrane (0.26 – 0.38 nm) would increase the diffusion coefficients of the water and NaCl. However, since the difference of the radius of larger pores between the uncross-linked and the cross-linked PBI membranes is small, it would not substantially affect the diffusion coefficients of water and NaCl. Whereas, the smaller pores in the membrane (0.14 – 0.24 nm) would selectively permeate water molecule and repel the Na^+ and Cl^- ions, which result in the improvement of the selectivity. Although the numbers of the smaller and larger pores could not be estimated from the PALS measurements, the significant improvement of the D_w value and the suppression of the increase in the B value of **CL-BSPBI** imply that the different free volume elements, especially smaller pores, led to the formation of the channels for the selective and effective permeation of the water molecules in the cross-linked membrane.

As the J_w and R values are functions of the applied pressure from outside and salt concentration, A and B values should be used as the intrinsic transport properties of the membrane materials.[25] Moreover, it is difficult to determine the intrinsic transport properties of the cross-linked PA and various asymmetric membrane materials, since the transport properties of these membranes depend not only on the membrane materials but also on the membrane fabrication process and membrane structure.[26–31] Compared to the symmetric semipermeable membranes based on various polymeric materials such as CA (A : 0.07 L μm m^{-2} h^{-1} bar^{-1}, B : 0.12×10^{-8} cm^2 s^{-1}),[32] aromatic PAs (A : 0.19 L μm m^{-2}

h^{-1} bar^{-1}, B : 0.004×10^{-8} cm^2 s^{-1}),[32] and sulfonated poly(arylene ether sulfone) (PESf) random copolymer (A : 0.03-4.21 L μm m^{-2} h^{-1} bar^{-1}, B : 0.004×10^{-8}-9.4×10^{-8} cm^2 s^{-1}),[10,33] **CL-BSPBI** shows an excellent high A and low B values, as shown in **Figure 4-10**. Furthermore, the improvement by cross-linking does not follow the general trade-off relationship between A and low B values, indicating the present work opens an effective direction of simultaneous improvement in the water permeability and selectivity.

Table 4-5 Water and NaCl transport properties of all PBI membranes.

Polymer	J_w[a] [L m^{-2} h^{-1}]	R[a] [%]	A[a] [L μm m^{-2} h^{-1} bar^{-1}]	B[a] [cm^2 s^{-1}]	K_w[b]	D_w[b] [cm^2 s^{-1}]	K_s[c]	D_s[c] [cm^2 s^{-1}]
PBI	1.25	13	0.353	0.046×10^{-8}	0.130	1.042×10^{-5}	0.081	5.71×10^{-9}
BPBI	1.25	4	0.353	0.167×10^{-8}	0.096	1.405×10^{-5}	0.059	2.84×10^{-8}
CL-BPBI	2.63	25	0.742	0.044×10^{-8}	0.113	2.501×10^{-5}	0.058	7.56×10^{-9}
BSPBI	1.88	11	0.530	0.084×10^{-8}	0.403	0.502×10^{-5}	0.323	2.61×10^{-9}
CL-BSPBI	22.1	46	6.241	0.144×10^{-8}	0.407	5.849×10^{-5}	0.356	4.05×10^{-9}

[a]Measured at 25°C using cross-flow filtration (ΔP =7.5 bar ; NaCl concentration = 500 mg L^{-1}) . [b]Estimated from water uptake and dry density measurements. [c]Measured by NaCl desorption measurement.

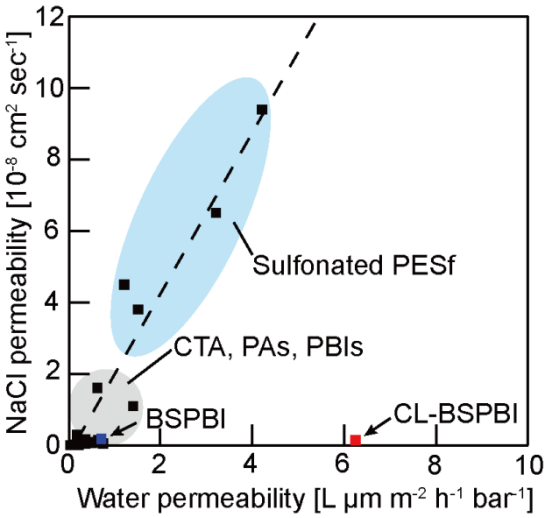

Figure 4-10 Relationship between water and NaCl permeability of symmetric single membranes based on PBIs, sulfonated PESf random copolymers, aromatic PAs, and CAs with the general trade-off relationship.

4.3 Conclusions

The improvement in water permeability while maintaining NaCl permeability has been demonstrated by cross-linking reaction of the *N*-butyl sulfonated polybenzimidazole (**BSPBI**) with divinyl sulfone. From WAXD and FTIR observations, it is confirmed that the suppression of the hydrogen bonding induced by the *N*-substitution and the cross-linked structure led to the polymer packing disruption. The cross-linking reaction changed the pore radius distribution, wherein the selective improvement of hydraulic water permeability with maintaining the NaCl permeability of the membrane was achieved. Especially, **CL-BSPBI** showed high hydraulic water permeability (6.24 L μm m^{-2} h^{-1} bar^{-1}) and relatively low NaCl permeability (0.144×10^{-8} cm^2 s^{-1}), among conventional polymeric membrane materials.

4.4 Experimental

4.4.1 Materials

Isophthalic acid, 1,4-propanesultone, 1-bromobutane, benzimidazole, and divinyl sulfone were purchased from TCI, Japan. *N*,*N*-Dimethylacetamide (DMAc), dimethyl sulfoxide (DMSO), acetone, hydrochloric acid, sodium bicarbonate, and lithium hydride were purchased from Wako Pure Chemical Industries. Polyphosphoric acid (PPA) was purchased from Sigma-Aldrich. Poly(*p*-phenylenebenzimidazole) (PBI) was synthesized by the polycondensation of 3,3'-diaminobenzidine and isophthalic acid in PPA. [34]

4.4.2 Synthesis of *N*-butylsulfonated PBI (BSPBI)

A 200 mL two-necked flask equipped with a magnetic stirring bar and a reflux condenser was charged with PBI (5.05 g, 16.4 mmol unit) and DMAc (80.0 mL) under a nitrogen atmosphere. The flask was immersed into an oil bath and the mixture was heated at 85 °C. After dissolution of the PBI, lithium hydride (1.29 g, 163 mmol) was added and the solution was stirred for 3 h. 1,4-Butanesultone (2.23 g, 16.4 mmol) was added to this solution and the solution was stirred for 24 h at 85 °C. Then, the solution was poured into a large amount of acetone to yield the brown fibrous polymer. The obtained polymer was filtered off, washed thoroughly with acetone, and dipped in a 10 wt% $NaHCO_3$ aqueous solution for 24 h. Then, the polymer was filtered off, washed with water, and dried in vacuum oven for 24 h at 120 °C.

Yield: 7.32 g (96 %). ^{1}H NMR (300 MHz, DMSO-d_6, δ, 40 °C): 9.13-7.72 (m, 10H), 4.46 (s, 2H), 1.95 (s, 4H), 1.68 (s, 2H). IR (Film), ν (cm^{-1}): 1631 (C=N stretching), 1182

(-SO_3Na asymmetric stretching), 1043 (-SO_3Na symmetric stretching).

4.4.3 Synthesis of *N*-butylated PBI (BPBI)

The title compound, BPBI, was synthesized by the same procedure as the BSPBI performed with lithium hydride (1.29 g, 163 mmol), DMAc (80 mL), 1-bromobutane (2.23 g, 16.3 mmol). Yield: 5.91 g (99 %). ^{1}H NMR (300 MHz, DMSO-d_6, δ, 40 °C): 9.18-7.58 (m, 10H), 4.32 (s, 2H), 1.74 (s, 2H), 1.20 (s, 2H), 0.78 (s, 3H). IR (Film), v (cm^{-1}): 2959 (alkyl C-H stretching), 1620 (C=N stretching).

4.4.4 Model reaction and calculation for the reaction rate constant

The model reaction was conducted as follows. To two-necked 50 mL flask, benzimidazole (**1**) (708.8 mg, 6.0 mmol), divinyl sulfone (**2**) (354.5 mg, 3.0 mmol) and DMSO-d_6 (16 mL) were added under argon atmosphere. After complete dissolution, the solution was stirred at 70 °C. Periodically, 0.4 mL of the reaction solution was sampled and immediately cooled down to stop the reaction. Then, the ^{1}H NMR measurements were conducted to reveal the molar ratio of the reactants and products (**3**, **4**).

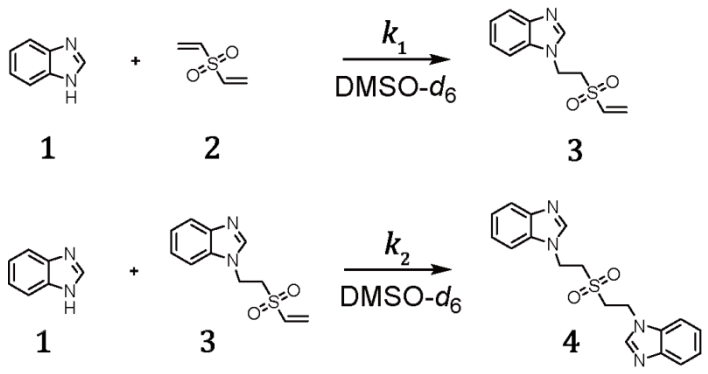

Figure 4-11 1:1 model reaction between benzimidazole (**1**) and divinyl sulfone (**2**)

Since the model reaction between **1** and **2** proceeds as shown in the reaction kinetics can be expressed as the following equations:

$$-\frac{d}{dt}[\mathbf{2}] = k_1[\mathbf{1}][\mathbf{2}] \quad (4.4)$$

$$-\frac{d}{dt}[\mathbf{1}] = k_1[\mathbf{1}][\mathbf{2}] + k_2[\mathbf{1}][\mathbf{3}] \quad (4.5)$$

$$-\frac{d}{dt}[\mathbf{3}] = -k_1[\mathbf{1}][\mathbf{2}] + k_2[\mathbf{1}][\mathbf{3}] \quad (4.6)$$

The initial concentration of each compound is defined as: $[\mathbf{1}]_0$, $[\mathbf{2}]_0$, $[\mathbf{3}]_0$, and $[\mathbf{4}]_0$, where $[\mathbf{3}]_0$=0, $[\mathbf{4}]_0$=0. Furthermore, dimensionless variables (α, β, γ, and δ) are introduced as:

$$\alpha = \frac{[\mathbf{1}]}{[\mathbf{1}]_0}, \qquad \beta = \frac{[\mathbf{2}]}{[\mathbf{2}]_0}, \qquad \gamma = \frac{[\mathbf{3}] + [\mathbf{4}]}{[\mathbf{2}]_0}, \text{and } \delta = \frac{[\mathbf{3}]}{[\mathbf{2}]_0} \quad (4.7) - (4.10)$$

and the parameters κ and S are defined by

$$\kappa = \frac{k_2}{k_1} \quad (4.11)$$

$$S = 2\frac{[\mathbf{2}]_0}{[\mathbf{1}]_0} \quad (4.12)$$

where κ is the ratio of the two rate constants and S is the parameter of stoichiometric imbalance.

From the relationships, $[\mathbf{2}]_0 = [\mathbf{2}] + [\mathbf{3}] + [\mathbf{4}]$ and $[\mathbf{1}]_0 = [\mathbf{1}] + [\mathbf{3}] + 2[\mathbf{4}]$, γ and δ can be expressed as:

$$\gamma = 1 - \beta \qquad (4.13)$$

and

$$\delta = \alpha - 1 + S(1 - \beta) \qquad (4.14)$$

Additionally, the normalized dimensionless time τ is defined as:

$$\tau = k_1[\mathbf{2}]_0 t \quad (4.15)$$

By solving the coupled equations (4.4) and (4.6), α can be expressed by β, S, and κ as:

$$\alpha = 1 - S + \frac{S\beta}{2(\kappa - 1)}(2\kappa - a - \beta^{\kappa - 1}) \quad (4.16)$$

By using this equation, α value is calculated at the specific β value.

The equation (4.4) is rewritten by

$$-\frac{d}{dt}\beta = \frac{2[\mathbf{1}]_0 k_1}{S}(2\kappa - 1 - \beta^{\kappa - 1}) \quad (4.17)$$

The equation (4.17) can be solved to obtain

$$\tau = \int_1^{\frac{1}{\beta}} \frac{dw}{\left(\frac{2}{S} - 2\right)w + \frac{1}{\kappa - 1}(2\kappa - 1 - w^{1-\kappa})} \quad (4.18)$$

The right-hand side of the equation (4.18) can be calculated using Romberg's method by Igor Pro (ver. 6.3.4.0, HULINKS).

From the relationship between β values and t obtained from the experiment (**Figure 4-12**), the τ values corresponding to reaction times t were calculated using equation (4.18) by assuming certain κ value.

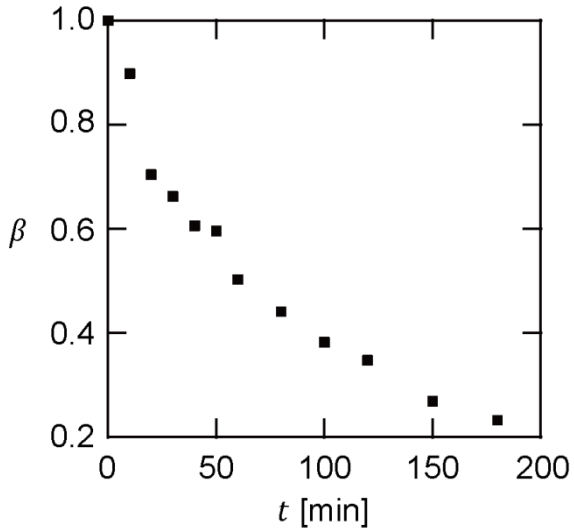

Figure 4-12 The relationship between the residual ratio β (= $[2]/[2]_0$) and the reaction time (t) values.

Since the τ value should be proportional to t as expressed in the calculated τ values were plotted versus t for a series of κ values. The correlation coefficients (R^2) obtained from the fitting of the linear equations using the least square method were evaluated. **Figure 4-13** indicates the calculated R^2 values plotted versus κ value, and the maximum R^2 value (0.9930) was obtained when κ = 1.3. From the equation (4.15) and (4.11), the k_1 and k_2 values at 70 °C were calculated to be 1.63×10^{-3} L mol^{-1} min^{-1} and 2.12×10^{-3} L mol^{-1} min^{-1}, respectively. Also, the k_1 and k_2 values at 200 °C were similarly determined to be 4.09×10^{-1} and 5.33×10^{-1}, respectively.

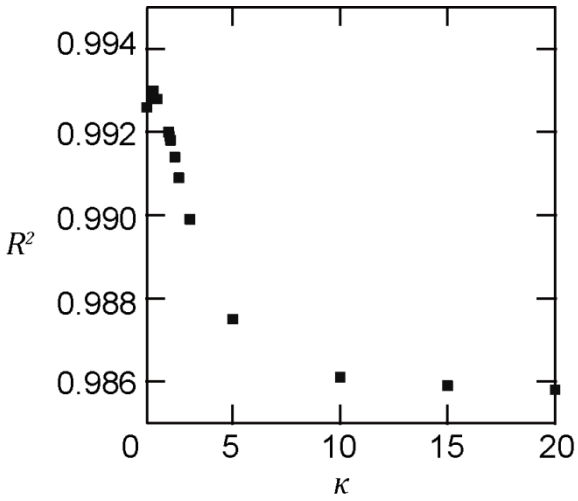

Figure 4-13 The relationship between the κ and the correlation values (R^2).

4.4.5 Preparation of ultrathin PBI membranes

10 wt% solutions of the PBIs were prepared in DMSO by heating. Then, the polymer solutions were filtered with a 0.45 μm poly(vinylidene fluoride) membrane filter. Subsequently, the polymer solutions were spin-coated onto a clean glass substrate to obtain the as-cast membrane with < 2.0 μm thickness. The as-cast membranes were then heated at 70 °C for 30 min and at 200 °C for 1 h. After cooling to room temperature, the obtained membranes were immersed into water, peeled off from the glass substrate, and stored in water. Finally, the membranes were immersed into 10 wt% isopropanol aqueous solution for 15 min and into water for 15 min just before measuring their membrane intrinsic separation properties.

4.4.6 Preparation of cross-linked PBI membranes

10 wt% solutions of the PBIs were prepared in DMSO by heating. After cooling to room temperature, divinyl sulfone (1.0 mol% to –NH-group in each imidazole ring) was added to the polymer solutions as a cross-linker and the obtained polymer solutions were filtered with a 0.45 μm poly(vinylidene fluoride) membrane filter. Subsequently, the polymer solutions were spin-coated onto a clean glass substrate to obtain the as-cast membranes with < 2.0 μm thickness. For the desolvation and cross-linked reaction, the as-cast membranes were then heated at 70 °C for 30 min and at 200 °C for 1 h. After cooling to room temperature, the obtained membranes were immersed into water, peeled off from the glass substrate, and stored in water. Finally, the membranes were immersed into 10 wt% isopropanol aqueous solution for 15 min and into water for 15 min just before measuring their membrane intrinsic separation properties.

4.4.7 Evaluation of water and NaCl transport properties

Membrane disks of 7 cm diameter were placed in the cross-flow filtration cells of custom-made equipment. Under an operating pressure of 7.5 bar to perform membrane filtration, a 500 mg L^{-1} aqueous solution of NaCl was supplied to the membranes. The temperature and pH of the feed solution were kept at 25 °C and 6.5, respectively. Subsequently, the feed and permeate water were sampled after the operation had been continued for more than 3 h to stabilize the membrane performance. Salt rejection rate (R value) was calculated based on the electrical conductivities of the feed and permeate water measured by a pH/EC meter WM-50EG (DKK-TOA Corp.). The flow rate of the solution was 3.5 L/min. Water flux (J_w, [L m^{-2} h^{-1}]), NaCl rejection (R, [%]), hydraulic

water permeability (A, [L μm m^{-2} h^{-1} bar^{-1}]), and salt permeability (P_S, [cm^2/s]) are calculated from the following equations.

$$J_w = \frac{\Delta V}{S\Delta t} \quad (4.19)$$

$$R = \left(1 - \frac{C2}{C1}\right) \times 100 \quad (4.20)$$

$$A = \frac{J_w l}{\Delta P - \Delta \pi} \quad (4.21)$$

$$B = \frac{10^{-7}}{3600} \times J_w l \times \frac{C_2}{(C_1 - C_2)} = \frac{10^{-7}}{3600} \times J_w l \times \frac{100 - R}{R} \quad (4.22)$$

where ΔV [L] is the volume of permeate water, S [m^2] is the effective membrane area, Δt [h] is time during water permeation, C_1 and C_2 are the salt concentrations in the feed and permeate water, l [μm] is the membrane thickness, ΔP [bar] is pressure difference across the membrane, and $\Delta \pi$ [bar] is osmotic pressure difference across the membrane. To clarify the relationships among *A*, *B*, and *R*, *R* is also expressed by the following equation: [35]

$$R = 100 \times \left(1 + \frac{B}{A(\Delta P - \Delta \pi)}\right)^{-1} \quad (4.23)$$

4.4.8 Determination of water sorption coefficient and water diffusion coefficient

Before the water uptake and dry density measurements, all of the PBI membranes were dried in vacuum oven at 120 °C for 2 days. Polymer densities (ρ_P, g cm^{-3}) were determined using an Alfa Mirage SD-200L electronic densimeter at ambient temperature (24-25 °C) using the following equation:

$$\rho_P = \frac{m_A}{m_A - m_L} \rho_o \quad (4.24)$$

where m_A and m_L are weights of the membrane measured in air and non-solvent, respectively, and ρ_o is density of the non-solvent. Ethanol was selected as the non-solvent. To estimate the water uptake (ω_w), the dried membranes were immersed in deionized water at ambient temperature (24-25 °C) for 3 days after the weight of the dried membranes (m_d) was measured. Then, the weight of hydrated membranes (m_h) was measured. ω_w was calculated as the following equation:

$$\omega_w = \frac{m_h - m_d}{m_d} \quad (4.25)$$

From the ω_w value, the equilibrium volume fraction of water in the hydrated membrane (ϕ_w) was evaluated as follows:

$$\phi_w = \frac{\rho_p \omega_w}{\rho_p \omega_w + \rho_w} \quad (4.26)$$

where ρ_w is the density of water (1.0 g cm^{-3}). Using the ϕ_w value, water sorption coefficient (K_w) can be estimated, which is defined as the ratio of water concentration in the membrane (C_w^m) to that in the solution (C_w) ([g water/cm^3 hydrated membrane]/[g water/ cm^3 solution]) as shown in the following equation.[25]

$$K_W = \frac{C_w^m}{C_w} = \frac{\phi_w M_w}{\rho_w V_w} \quad (4.27)$$

where C_w is equal to the density of pure water (ρ_w), M_w is the molecular weight of water, and V_w is the molar volume of water (18 cm^3/mol).[36]

The diffusive water permeability (P_w, [cm^2 s^{-1}]) is related to water permeability (A, [L μm m^{-2} h^{-1} bar^{-1}]) as follows:

$$P_w = A \times \frac{RT}{V_w} \times \frac{10^{-6}}{36} \quad (4.28)$$

where R is the ideal gas constant (8.314 J K^{-1} mol^{-1}) and T is the absolute temperature.

Water diffusive coefficient (D_w, cm^2 s^{-1}) estimated from P_w and K_w based on the following equation:

$$D_w = \frac{P_w}{K_w} \quad (4.29)$$

4.4.9 Determination of NaCl sorption coefficient and NaCl diffusion coefficient

The salt partition coefficient (K_s) was determined by salt desorption into deionized water from the membrane previously equilibrated with 50 mL of 1.0 M NaCl aqueous solution by immersing into that solution for at least 3 days. K_s is calculated by the ratio of the mass in the membrane per unit volume to the concentration of NaCl in the original solution as follows:

$$K_s = \frac{M_\infty \rho_p}{m} \times \frac{1}{58.44 \times 10^{-3}} \quad (4.30)$$

Where M_∞ is the total weight of salt desorbed from the membrane, m is the weight of the membrane, ρ_p is the polymer density. The salt diffusion coefficient (D_S) is estimated from the measured salt permeability (B value) as follows:

$$D_s = \frac{B}{K_s} \quad (4.31)$$

4.4.10 Measurements

The nuclear magnetic resonance (NMR) spectra were recorded on a Bruker DPX-300S spectrometer at the resonant frequencies of 300 MHz for ^{1}H and 75 MHz for ^{13}C nuclei using $CDCl_3$ or DMSO-d_6 as the solvents and tetramethylsilane as an internal standard (δ_H 0.00). The FT-IR spectra were measured on a Horiba FT-720 spectrometer. The inherent viscosities were measured at 30 °C in NMP at a polymer concentration of 0.5 g/dL. The thermal analysis (TGA) was performed on a Seiko TG/DTA 6300 thermal analysis system under a nitrogen atmosphere for thermogravimetry (TG) and differential thermal analysis (DTA). Before the evaluation, all the samples were preheated at 250 °C for 30 min to remove any moisture and residual solvents in the TG/DTA furnace. The samples were then cooled to 30 °C and heated to 500 °C at the heating rate of 10 °C/min. The contact angles of water droplets on the prepared membranes were measured by the sessile drop method using a contact angle measurement system (DropMaster 500, Kyowa Interface Science). The volume of the water droplets for the measurements was 2.0 μL. All measurements were carried out at five or more different points for each sample at ambient temperature (24-25 °C) and were reproducible within 2°. The dry densities of the dried membranes were determined using an Alfa Mirage SD-200L electronic densimeter at ambient temperature (24-25 °C). The surface morphology was characterized using an atomic force microscopic (AFM, SPA400, SII Nanotechnology) in the phase contrast mode. Low-energy positron annihilation lifetime spectroscopy (PALS) was measured on a Fuji-imvac PALS-200A at an incident positron energy of 7.0 keV. A multi-exponential analysis using the RESOLUTION code was applied to the obtained positron annihilation lifetime spectra to attain the average lifetime of the third component (τ_3) for the triplet *ortho*-positronium (*o*-Ps). The pore size distributions were calculated by

MELT analyses.[18]

4.5 Reference

(1) Glipa, X.; Bonnet, B.; Mula, B. *J. Mater. Chem.* **1999**, 3045–3049.

(2) Aiba, M.; Tokuyama, T.; Matsumoto, H.; Tomioka, H.; Higashihara, T.; Ueda, M. *J. Appl. Polym. Sci.* **2014**, *132*, 41531/1 – 41531/7.

(3) Lee, C. H.; VanHouten, D.; Lane, O.; McGrath, J. E.; Hou, J.; Madsen, L. a.; Spano, J.; Wi, S.; Cook, J.; Xie, W.; Oh, H. J.; Geise, G. M.; Freeman, B. D. *Chem. Mater.* **2011**, *23*, 1039–1049.

(4) Aiba, M.; Tokuyama, T.; Matsumoto, H.; Tomioka, H.; Higashihara, T.; Ueda, M. *J. Polym. Sci. Part A Polym. Chem.* **2014**, *52*, 3453–3462.

(5) Shibasaki, Y.; Abe, Y.; Sato, N.; Fujimori, A.; Oishi, Y. *Polym. J.* **2010**, *42*, 72–80.

(6) Shi, H.; Zhao, Y.; Zhang, X.; Zhou, Y.; Xu, Y.; Zhou, S.; Wang, D.; Han, C. C.; Xu, D. *Polymer.* **2004**, *45*, 6299–6307.

(7) Aiba, M.; Tokuyama, T.; Baba, S.; Matsumoto, H.; Tomioka, H.; Higashihara, T.; Ueda, M. *J. Polym. Sci. Part A Polym. Chem.* **2014**, *52*, 1275–1281.

(8) Kumbharkar, S. C.; Kharul, U. K. *J. Memb. Sci.* **2010**, *357*, 134–142.

(9) Wang, K. Y.; Yang, Q.; Chung, T. S. *Chem. Eng. Sci.* **2009**, *64*, 1577–1584.

(10) Paul, M.; Park, H. B.; Freeman, B. D.; Roy, A.; McGrath, J. E.; Riffle, J. S. *Polymer.* **2008**, *49*, 2243–2252.

(11) Wang, K. Y.; Xiao, Y.; Chung, T. S. *Chem. Eng. Sci.* **2006**, *61*, 5807–5817.

(12) Staudt-bickel, C.; Koros, W. J. *J. Memb. Sci.* **1999**, *155*, 145–154.

(13) Wind, J.; Staudt-Bickel, C. *Ind. Eng. Chem. Res.* **2002**, *41*, 6139–6148.

(14) Calle, M.; Doherty, C. M.; Hill, A. J.; Lee, Y. M. *Macromolecules* **2013**, *46*, 8179–8189.

(15) Horinouchi, A.; Atarashi, H.; Fujii, Y.; Tanaka, K. *Macromolecules* **2012**, *45*, 4638–4642.

(16) Eldrup, M.; Lightbody, D.; Sherwood, J. N. *Chem. Phys.* **1981**, *63*, 51–58.

(17) Tao, S. J. *J. Chem. Phys.* **1972**, *56*, 5499.

(18) Shukla, A.; Hoffmann, L.; Manuel, A. a.; Peter, M. *Mater. Sci. Forum* **1997**, *255-257*, 233–237.

(19) Pethrick, R. *Prog. Polym. Sci.* **1997**, *22*.

(20) Kihara, N.; Komatsu, S.; Takata, T.; Endo, T. *Macromolecules* **1999**, *32*, 4776–4783.

(21) Goto, E.; Ando, S.; Ueda, M.; Higashihara, T. *ACS Macro Lett.* **2015**, *4*, 1004–1007.

(22) Cohen, M. H.; Turnbull, D. *J. Chem. Phys.* **1959**, *31*, 1164.

(23) Nightingale, E. R. *J. Phys. Chem.* **1959**, *63*, 1381–1387.

(24) Xie, W.; Ju, H.; Geise, G. M.; Freeman, B. D.; Mardel, J. I.; Hill, A. J.; McGrath, J. E. *Macromolecules* **2011**, *44*, 4428–4438.

(25) Geise, G. M.; Park, H. B.; Sagle, A. C.; Freeman, B. D.; McGrath, J. E. *J. Memb. Sci.* **2011**, *369*, 130–138.

(26) Natalia Widjojo, Tai-Shung Chung, Martin Weber, Christian Maletzko, V. W. *J. Memb. Sci.* **2011**, *383*, 214–223.

(27) Ong, R. C.; Chung, T. S. *J. Memb. Sci.* **2012**, *394-395*, 230–240.

(28) Ikeda, K.; Endoh, R.; Tanaka, T.; Kurihara, M. *Desalination* **1977**, *21*, 35–44.

(29) Yong, Z.; Sanchuan, Y.; Meihong, L.; Congjie, G. *J. Memb. Sci.* **2006**, *270*, 162–168.

(30) Xie, W.; Geise, G. M.; Freeman, B. D.; Lee, H. S.; Byun, G.; McGrath, J. E. *J. Memb. Sci.* **2012**, *403-404*, 152–161.

(31) Gu, J. E.; Lee, S.; Stafford, C. M.; Lee, J. S.; Choi, W.; Kim, B. Y.; Baek, K. Y.; Chan, E. P.; Chung, J. Y.; Bang, J.; Lee, J. H. *Adv. Mater.* **2013**, *25*, 4778–4782.

(32) Frommer, M. a.; Murday, J. S.; Messalem, R. M. *Eur. Polym. J.* **1973**, *9*, 367–373.

(33) Park, H. B.; Freeman, B. D.; Zhang, Z. B.; Sankir, M.; McGrath, J. E. *Angew. Chem. Int. Ed. Engl.* **2008**, *47*, 6019–6024.

(34) Ueda, M.; Sato, M.; Mochizuki, A. *Macromolecules* **1985**, *18*, 2723–2726.

(35) Cath, T.; Childress, A; Elimelech, M. *J. Memb. Sci.* **2006**, *281*, 70–87.

(36) Xie, W.; Cook, J.; Park, H. B.; Freeman, B. D.; Lee, C. H.; McGrath, J. E. *Polymer* **2011**, *52*, 2032–2043.

Chapter 5

Solution and Solid-state Structures of Dynamic Covalent Aromatic Polyamides: Effect of Thermal Reorganization Behaviors

5.1 Introduction

In chapter 4, the improvement in water flux and NaCl rejection owing to the selective enhancement of water diffusion coefficient has been achieved by the formation of the smaller free-volume elements with 0.14-0.24 nm radius where water molecule can permeate while hydrated ions are repelled. Ideally, the formation of the free-volume elements with an appropriate radius and narrow size distribution is preferable for further improvement. However, to precisely control the free volume by crossliking rection during the heat-induced desolvation process (*i.e.*, the formation of free volume with an appropriate radius and narrow size disutribution) is still challenging. Therefore, we need to develop another approach to construct small free-volume elements.

Dynamic covalent polymers have become one of the attractive materials

because their primary structures and properties can be controlled by external stimulus even after the polymerization, and have been used in various fields.[1–3] Otsuka et al. reported that the molecular weight distribution of dynamic covalent polymers reached the theoretical value of about ~2.0 through the reversible dissociation and association of 2,2,6,6-tetramethylpiperidinyloxy (TEMPO) units in the main chain.[4] Moreover, they have revealed that the radical crossover reaction between two different dynamic polymers, polyester and polyurethane, induced their hybridization via ‘‘polymer scrambling’’ at the main chain level.[5]

Among the various polymeric materials, wholly aromatic polyamides (PAs), such as poly(*m*-phenyleneisophthalamide) and poly(*p*-phenyleneterephthalamide), are widely used as typical engineering plastic due to their high mechanical strength and high flame resistance.[6,7] Their outstanding physical properties and chemical stabilities are arise from their rigid aromatic backbone and secondary amide linkages, which result in an extended rod-like structure interacting with each other via hydrogen bondings and strong π-π stackings. On the other hand, disruption of the hydrogen bondings between the secondary amide linkages by *N*-alkylation or three-center-hydrogen bonding to suppress the hydrogen bondings affects the thermal/mechanical properties and the packing mode of the polymer main chain.[8–11] Moreover, the control over the state of PA also plays a critical role in determining the physical properties in the solid state. For example, the transport properties of small molecules through polymer thin films/membranes are mostly dependent on free volume. Especially, in chapter 4, we have revealed that the crosslinking reaction during the desolvation process induced the change in the pore-size distribution from monomodal to bimodal curves so that the significant improvement in the water transport properties is achieved. Therefore, it is

important to control the molecular aggregation structure in solution and films to afford desirable properties (e.g., mechanical properties, transparency, and permselectivity).[12–15] Although the dynamic covalent polymer in the main chain drastically changes the molecular state via dissociation and association reactions, to the best of our knowledge, the effect of thermal reorganization on the solution- and solid-state structures still remains unclear.

In chapter 5, we report the synthesis of a new aromatic PA (**TEMPO-PA**) with TEMPO units in the main chain and random coPA (**TEMPO-PA-COOH**) composed of a hydrophilic TEMPO unit and hydrophilic 3,5-diaminobenzoic acid (DABA) unit (see **Figure 5-1**), then the fundamental properties and the effect of radical crossover reaction on the polymer aggregation behavior were investigated in detail. Furthermore, the effect of the thermal reorganization process on the phase separation behavior of **TEMPO-PA-COOH** was carefully examined by time-resolved water contact angle measurements and atomic force microscopy observations.

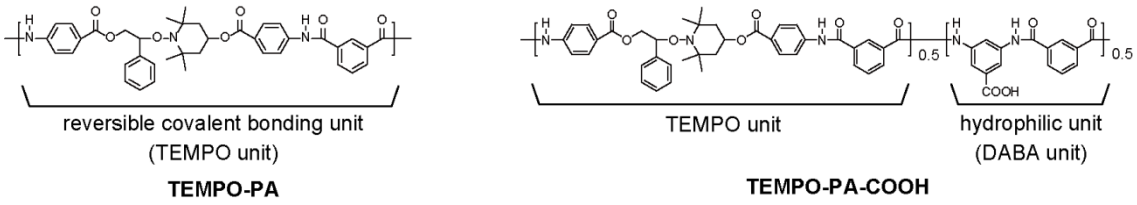

Figure 5-1 Chemical structures of **TEMPO-PA** and **TEMPO-PA-COOH**.

5.2 Result and discussion

5.2.1 Preparation, cleavage behavior, and thermal and mechanical properties

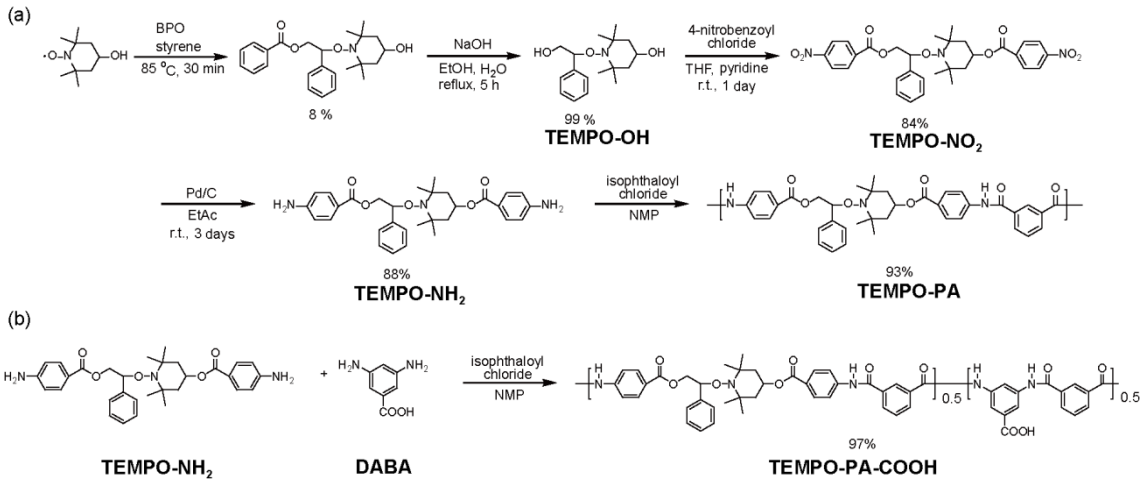

Scheme 5-1 Synthesis of (a) **TEMPO-PA** and (b) **TEMPO-PA-COOH**.

The diamine monomer, TEMPO-NH_2, was prepared in four steps according to **Scheme 5-1** and its molecular structure was confirmed by its ^{1}H NMR, ^{13}C NMR, and FTIR spectra (see experimental section). Subsequently, **TEMPO-PA** was synthesized by the low temperature polycondensation of isophthaloyl chloride with TEMPO-NH_2. Also, a random copolyamide (**TEMPO-PA-COOH**) composed of the TEMPO and hydrophilic DABA units was synthesized by the polycondensation reaction between TEMPO-NH_2, DABA, and isophthaloyl chloride. The chemical structures of the obtained **TEMPO-PA** and **TEMPO-PA-COOH** were fully characterized by their ^{1}H NMR, ^{13}C NMR, and FTIR spectra (**Figure 5-2**). For **TEMPO-PA**, the characteristic peak from the amide linkage is observed at 10.71 ppm (denoted as A) in the ^{1}H NMR spectrum and the integral values for each peak are consistent with the expected structure.

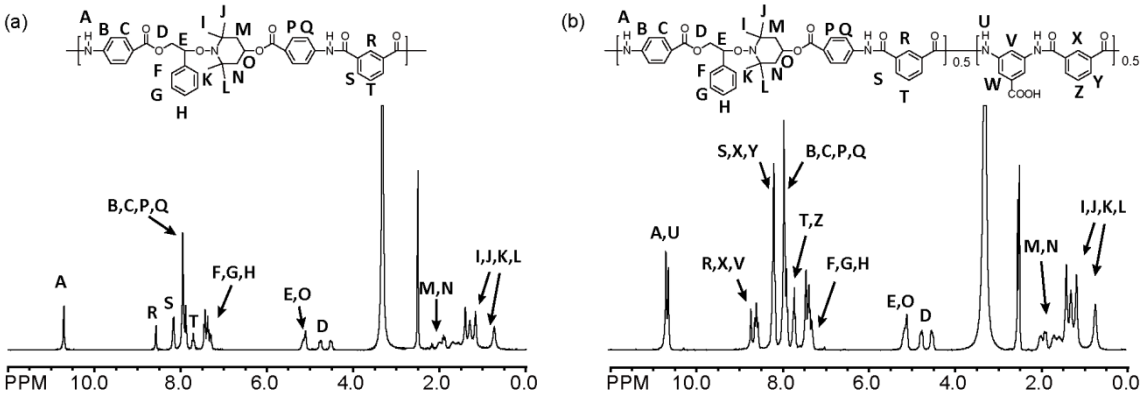

Figure 5-2 ^{1}H NMR spectra of (a) **TEMPO-PA** and (b) **TEMPO-PA-COOH** in DMSO-d_6 at 40 °C.

Although the different ordered structures (head to head/head to tail) could be formed by the polycondensation because of the asymmetric structure of TEMPO-NH_2, the splitting pattern of the isophthaloyl chloride moiety (labeled as R, S, and T) could not be observed in the ^{1}H NMR spectra. In the case of **TEMPO-PA-COOH**, the characteristic peaks of the amide proton (labeled as U) and of the aromatic protons corresponding to the DABA unit (labeled as V, W, X, Y, and Z) were confirmed. The **TEMPO-PA** and **TEMPO-PA-COOH** exhibited good solubilities in polar aromatic solvents (such as DMF, DMSO, DMAc, and NMP). The molecular weight of **TEMPO-PA** was estimated to be M_n = 46400 and M_w = 152900 by gel permeation chromatography. For **TEMPO-PA-COOH**, inherent viscosity (η_{inh}) measured at a concentration of 0.5 g dL^{-1} in DMSO at 30 °C was calculated to be 0.91, being consistent with high-molecular weight polymers.

First of all, ESR spectroscopy measurement of **TEMPO-PA** was carried out at different temperatures in order to determine the hemolytic cleavage behavior of the

C-ON bonds in the TEMPO units. **Figure 5-3** shows the ESR spectra of **TEMPO-PA** at different temperatures and the relative intensities of the radical signal estimated from the area are summarized in **Table 5-1**. According to the increase in the temperature from room temperature to 130 °C, the ESR signal intensity increased, indicating that the equilibrium of the alkoxyamine units shifted to the dissociated state. Although the relative intensities gradually increased from 25 °C to 100 °C, the drastic increase from 100 °C to 130 °C can be observed. Additionally, the equilibrium constant of the alkoxyamine unit at 130 °C was about five times higher than that at 100 °C by comparison of the intensities at each temperature.

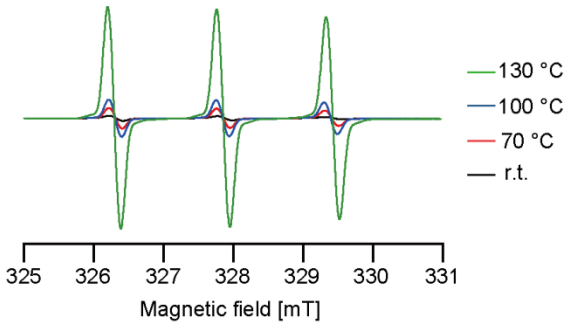

Figure 5-3 ESR spectra of the **TEMPO-PA** measured at different temperatures (r.t., 70, 100, and 130 °C) in DMSO.

Table 5-1 Relative ESR intensities calculated from the integral areas.

Temperature	[°C]	25	70	100	130
Intensity	[a.u.]	2.10	5.88	10.01	55.16

Subsequently, the thermal stability of the **TEMPO-PA** and **TEMPO-PA-COOH** were evaluated by a thermogravimetry (TG) analysis under a nitrogen atmosphere. As can be seen in **Figure 5-4**, **TEMPO-PA** and **TEMPO-PA-COOH** shows two-step weight loss behaviors from 250 to 400 and from 500 to 700 °C, respectively. Although the reversible reaction of the alkoxyamine moiety was confirmed from 70 °C, the 5 % weight loss temperatures ($T_{d5\%}$) for **TEMPO-PA** and **TEMPO-PA-COOH** were determined to be 259 °C and 275 °C, respectively.

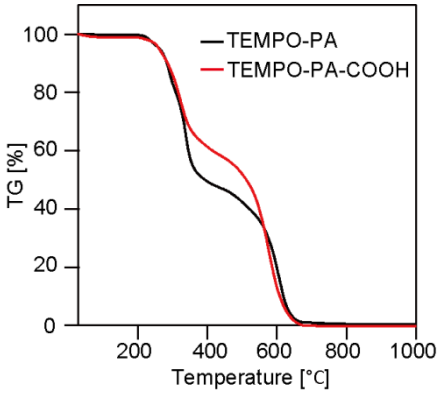

Figure 5-4 TG curves of **TEMPO-PA** and **TEMPO-PA-COOH**.

5.2.2 Radical stability and thermal reorganization behavior

In order to investigate the stability of the TEMPO unit, two polymer solutions in DMSO-d_6 at a concentration of 6 mg mL^{-1} were separately heated at 130 °C under air and argon atmospheres, and examined by ^1H NMR spectra monitoring (**Figure 5-5**). Under an argon atmosphere, no other peaks could be seen even after 24 h, indicating that the side reactions instead of the recombination of nitroxide with the styryl radicals had not occurred. On the other hand, the side reactions had obviously occurred after 16 h under an air atmosphere, since there could be seen other characteristic peaks in addition to those of **TEMPO-PA**. As has been reported by Matyjaszewski et al., the side reaction was due to the irreversible reaction of the styryl radical with oxygen and the following oxidation of nitroxide by peroxyl radicals.[16] Therefore, the **TEMPO-PA** and **TEMPO-PA-COOH** should be treated under an argon atmosphere.

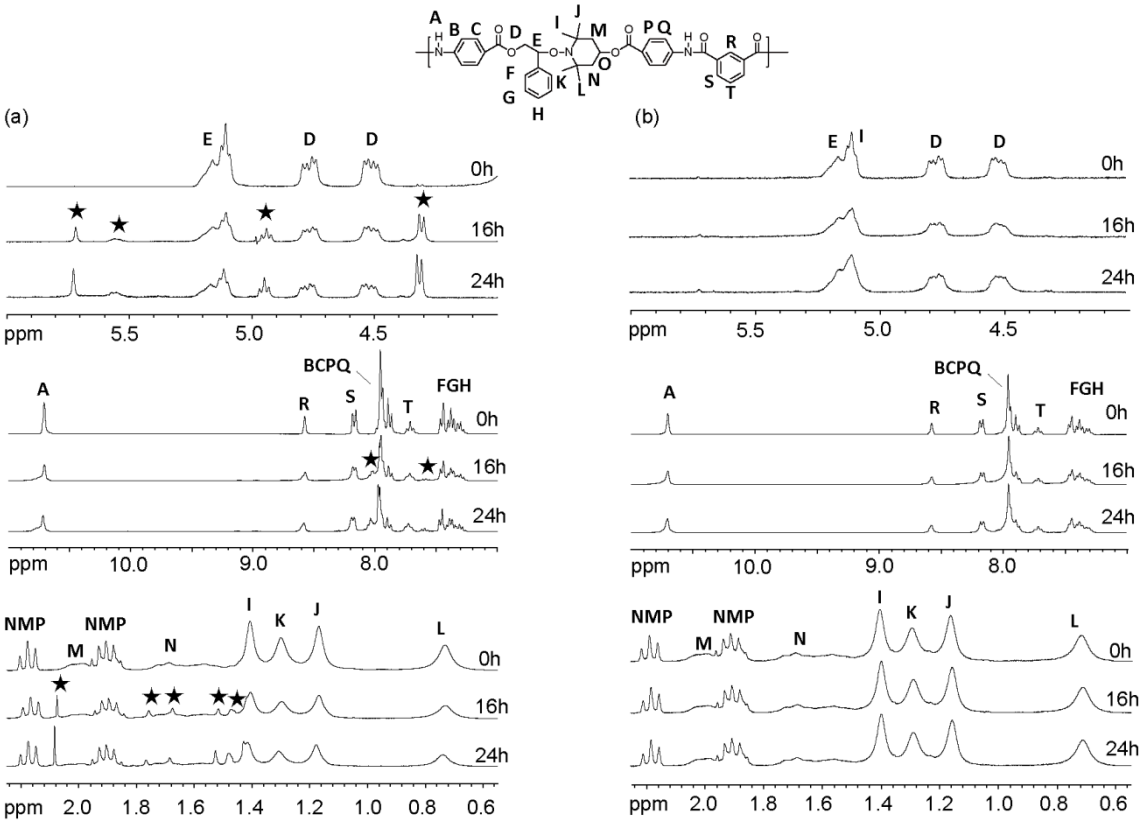

Figure 5-5 ^{1}H NMR spectra of **TEMPO-PA** heated at 130 °C for 0, 16, and 24 h under (a) an air and (b) argon atmosphere. The asterisked peaks cannot be assigned to the peaks corresponding to **TEMPO-PA**, indicating that side reactions occurred in the presence of oxygen in addition to the reversible recombination reaction between the nitroxide and styryl radicals.

Furthermore, to evaluate the effects of the thermal reorganization behavior of the alkoxyamine unit on M_n and M_w/M_n, **TEMPO-P**A ($M_n = 46400$, $M_w/M_n = 3.30$) was heated at 130 °C in the DMF solution under an argon atmosphere. A noticeable color change was not observed during the reaction, although the nitroxide radical shows a red color. As has been reported by Otsuka et al., M_w/M_n value reached ~2.0 as the theoretically expected value of step-growth polymerization within 1 h and no more changes were observed after 1 h due to the equilibrium state.[4] On the other hands, M_n values after thermal rearrangement reaction have become higher than the original one, probably because the molecular distribution from broad to narrow led to the formation of the middle-weight polymer. Indeed, **Figure 5-6** (a) shows that the molecular distribution has become narrower with the shift of the peak tops from higher to lower molecular weights. As can be seen in **Figure 5-6** (b), M_n, M_w, and M_w/M_n values seemed to attain equilibrium state after 1-24 h.

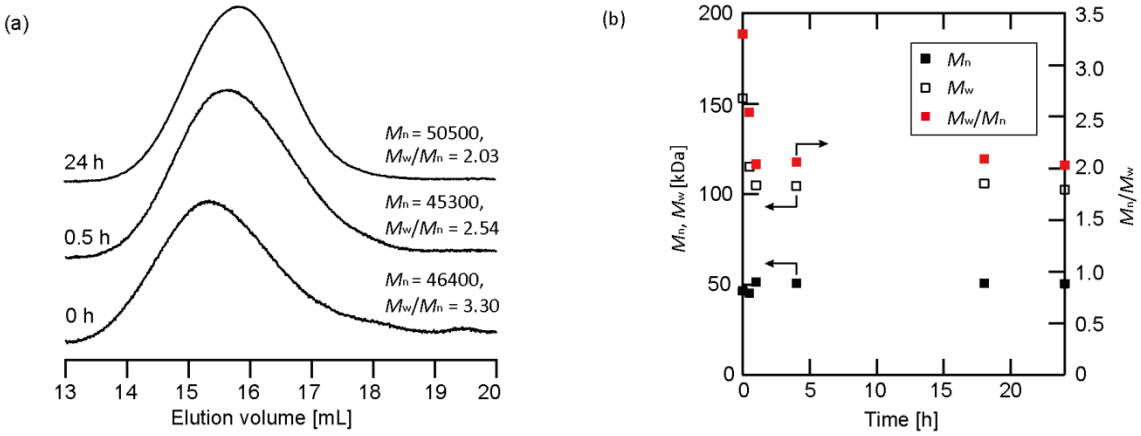

Figure 5-6 (a) GPC RI curves for TEMPO-PAs with heat treatment in DMF at 130 °C for 0, 0.5, 24 h. (b) Plots of M_n, M_w, and M_w/M_n as a function of time for **TEMPO-PAs** with heat treatment in DMF at 130 °C for 0, 0.5, 24 h.

In the case of **TEMPO-PA-COOH**, the TEMPO unit sequence in polymer main chain would be distributed again and it is probably possible to change the alignment of the TEMPO and DABA units along the polymer chain once thermal reorganization reaction of **TEMPO-PA-COOH** occurred. In general, the sequence of the random polymer can be identified by the peaks of the carbon nuclei in the amide linkages in the ^{13}C NMR spectra.[17] However, it was found that the sequential rearrangement of **TEMPO-PA-COOH** could not be traced by ^{13}C NMR spectra, since no changes in all amide peaks were observed after **TEMPO-PA-COOH** was heated in DMSO-d_6 at a concentration of 100 mg mL^{-1} for 2 h (**Figure 5-7**). This observation is probably because the reversible reaction of the nitroxide with the styryl radical is only limited to the TEMPO unit and there always exists a TEMPO unit next to the DABA unit.

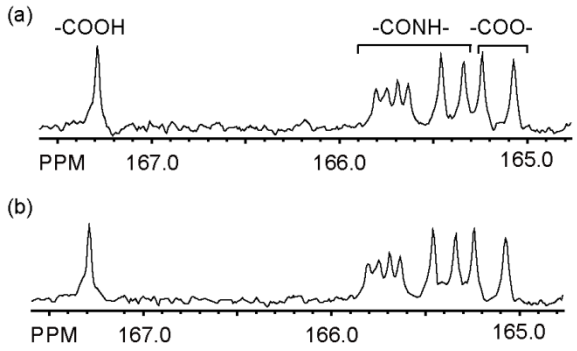

Figure 5-7 ^{13}C NMR spectra (carbonyl region) of **TEMPO-PA-COOH** in DMSO-d_6 at 40 °C (a) before and (b) after heating at 120 °C for 2 h. Any changes in the intensity of all the peaks could not be seen, indicating that it seems difficult to evaluate the sequential rearrangement of **TEMPO-PA-COOH** using ^{13}C NMR spectra.

5.2.3 Solution structures

5.2.3.1 ^{1}H NMR spectra

The chemical shift provides us with information about the hydrogen bonding behavior. Generally, the shift of the amide proton to low magnetic field is induced when the hydrogen bonding becomes strong.[18] Thus, the chemical shifts of the peaks assigned to the protons in the amide linkages of **TEMPO-PA** and **TEMPO-PA-COOH** at different temperatures were measured to evaluate the hydrogen bonding behavior. **Figure 5-8** shows the ^{1}H NMR spectra of **TEMPO-PA** and **TEMPO-PA-COOH** at different temperatures. The chemical shifts of the amide protons move to lower magnetic field with a rise in the temperature. This result indicates that the hydrogen bonding between the amide linkages has become weak with the increasing temperature.

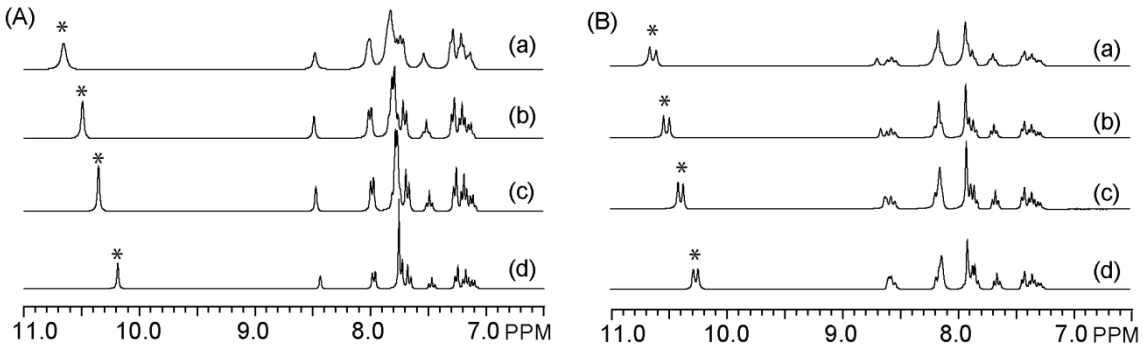

Figure 5-8 ^{1}H NMR spectra of (A) **TEMPO-PA** and (B) **TEMPO-PA-COOH** at (a) 25 °C, (b) 70 °C, (c) 100 °C, and (d) 130 °C in DMSO-d_6. The asterisked peaks are attributed to the amide ptrotons.

5.2.3.2 DLS measurements

Subsequently, DLS measurements of the **TEMPO-PA** and **TEMPO-PA-COOH** in DMSO at a concentration of 2.0 wt% were performed in order to evaluate the polymer solution structures at different temperatures. The correlation functions are shown in **Figure 5-9**. Hydrodynamic diameter, R_H, and diffusion coefficient, D, were assessed by CONTIN analysis, which are summarized in **Table 5-2**. These values were calculated assuming that the polymer possesses the shape of a hard sphere. The R_H values of **TEMPO-PA** and **TEMPO-PA-COOH** decreased with an increase in the membrane preparation temperature. Meanwhile, increases in the D values were observed. Therefore, it was suggested that both **TEMPO-PA** and **TEMPO-PA-COOH** in solution at high temperature are smaller than those at low temperature probably because a large amount of the alkoxyamine moieties in the main chain are dissociated in addition to the suppression of the hydrogen bondings between the amide linkages.

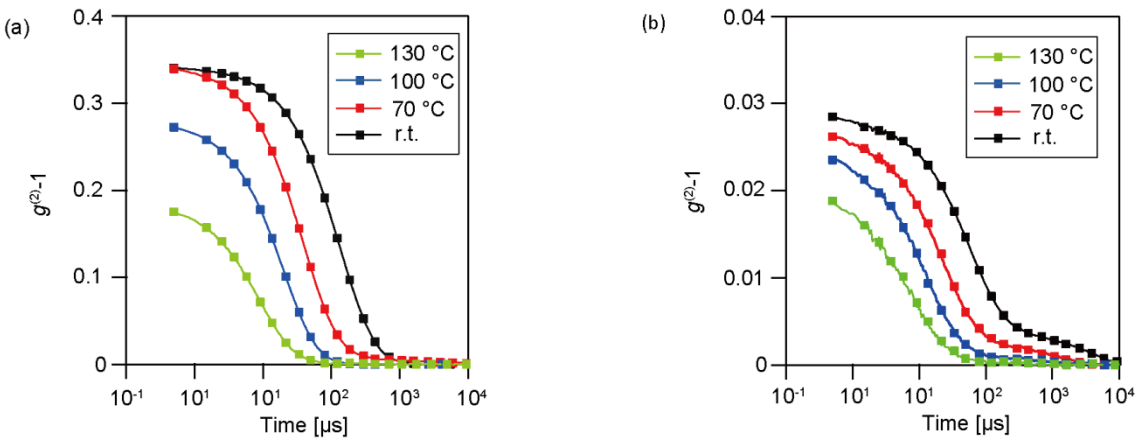

Figure 5-9 Correlation function corresponding to (a) **TEMPO-PA** and (b) **TEMPO-PA-COOH** at r.t., 70, 100, and 130 °C in DMSO.

Table 5-2 Hydrodynamic diameters and diffusion coefficients of **TEMPO-PA** and **TEMPO-PA-COOH** at different temperatures.

Polymer		TEMPO-PA				TEMPO-PA-COOH			
Temperature	[°C]	25	70	100	130	25	70	100	130
R_H[a]	[nm]	10.15	7.62	4.13	1.83	5.93	4.46	3.10	1.35
D[a]	[10^{-8} m^2 s^{-1}]	1.04	2.91	9.64	53.6	1.77	4.33	10.3	55.1

[a]Hydrodynamic diameters and diffusion coefficients were calculated using Einstein-Stokes equation.

5.2.4 Solid-state structures

In order to investigate the effect of the radical crossover reaction on the molecular aggregation structure, both **TEMPO-PA** and **TEMPO-PA-COOH** thin films were prepared at the three different temperatures of 70, 100, and 130 °C. Since the unexpected reaction of the alkoxyamine moiety easily occurred in the presence of oxygen, the membrane preparation process was conducted in a glove box after the polymer solutions were degassed by four cycles of freeze-pump-thaw. In this section, the state of polymer in films was described.

5.2.4.1 FTIR spectra

Figure 5-10 shows the FTIR spectra of the **TEMPO-PA** and **TEMPO-PA-COOH** in order to evaluate the hydrogen bonding behavior in the thin film. Generally, two characteristic peaks of the amide linkage, such as the C=O stretching and the N-H in-plane bending, are shifted to the higher and lower wavenumbers, respectively, when the hydrogen bonding between the amide linkage becomes weak.[19] For **TEMPO-PA**, the peak corresponding to the C=O stretching is shifted from 1682 cm^{-1} to 1685 cm^{-1} with the increase in the thin-film preparation temperature, whereas the peak assigned to the N-H in-plane bending is shifted from 1536 cm^{-1} to 1530 cm^{-1}. This result indicates that the hydrogen bondings between the amide linkages are suppressed when the thin film is prepared at high temperature. In the case of the **TEMPO-PA-COOH**, similar shifts of the peaks attributed to the C=O stretching and N-H in-plane bending are also confirmed.

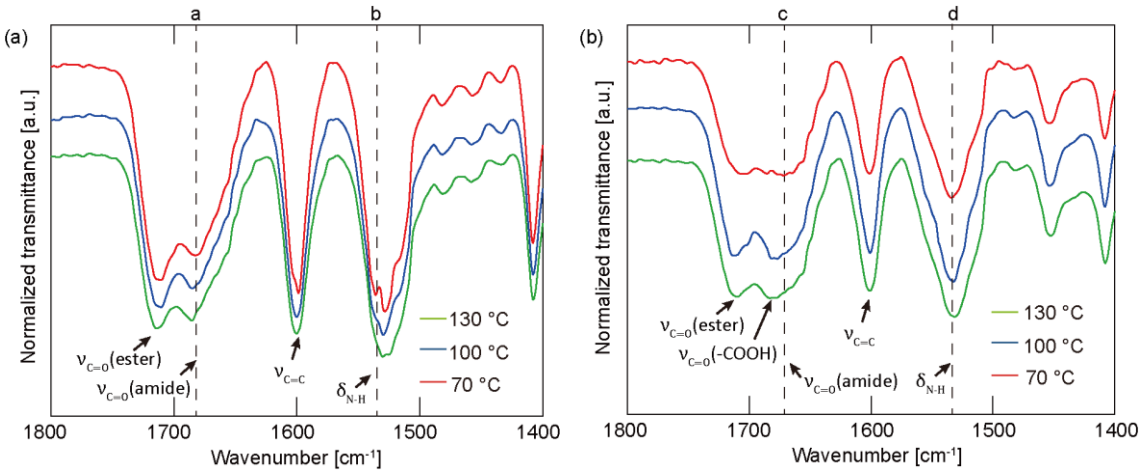

Figure 5-10 FTIR spectra of (a) **TEMPO-PA** and (b) **TEMPO-PA-COOH** films fabricated at different temperatures. The dotted lines (a, b, c, and, d) indicate wavenumbers at 1682, 1536, 1672, and 1534 cm^{-1}, respectively.

5.2.4.2 Dry densities

Subsequently, the dry densities were measured for estimation of the free volume and summarized in **Figure 5-11**.[12] With an increase in the thin film preparation temperature, the dry densities of both **TEMPO-PA** and **TEMPO-PA-COOH** clearly decreased from 1.248 to 1.229 and from 1.301 to 1.282, respectively, indicating that free volume of the polymer thin film can be controlled by the fabrication temperature. This result is in good accordance with the FTIR spectra and implies that the disruption of the polymer packing mainly occurs due to the suppression of the hydrogen bonding. Although there is no experimental evidence, the aggregation behavior in the thin film would also be affected by the thermal reorganization behavior.

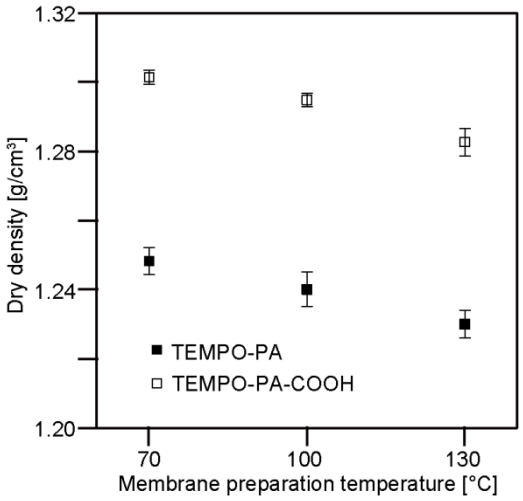

Figure 5-11 Dry densities of **TEMPO-PA** and **TEMPO-PA-COOH** films fabricated at different temperatures (70, 100, and 130 °C).

5.2.4.3 Time-resolved contact angles measurement

The surface reorganization of the **TEMPO-PA** and **TEMPO-PA-COOH** films induced by liquid molecules was investigated by water contact angle measurements. **Figure 5-12** represents the time course of the water contact angles for the **TEMPO-PA** and **TEMPO-PA-COOH** films prepared at different temperatures. Since the contact angle value is mostly influenced by the surface roughness, the root-mean-square roughness, R_{RMS}, of **TEMPO-PA** and **TEMPO-PA-COOH** were determined by atomic force microscopy (AFM).[20] The R_{RMS} values for all the films were from 0.2 to 0.4 nm, indicating that the contact angle values mainly depend on the surface chemical structure. The water contact angles of all the **TEMPO-PA** membranes and the **TEMPO-PA-COOH** film fabricated at 70 °C linearly decreased with the increasing time. On the other hand, two regions (an initial exponential decay and the subsequent linear line) can be seen in the **TEMPO-PA-COOH** films fabricated at 100 °C and 130 °C.

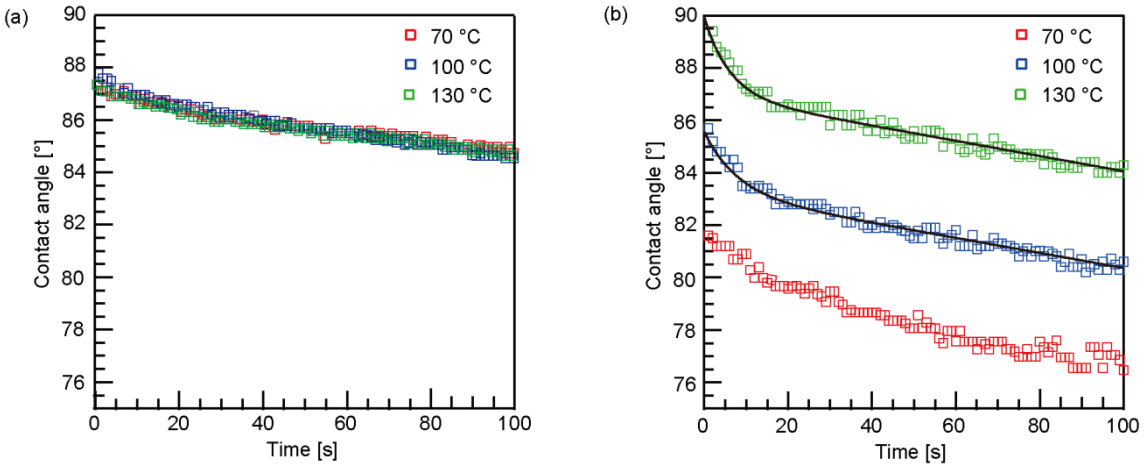

Figure 5-12 Time dependence of water contact angle against (a) **TEMPO-PA** and (b) **TEMPO-PA-COOH** films fabricated at 70, 100, and 130 °C.

According to a previous report, the initial contact angle decay and a subsequent linear decrease reflect both the surface segregation induced by the water droplet and the change in the droplet shape due to water evaporation, respectively.[21,22] As the initial decay cannot be seen in all the **TEMPO-PA** films, the segregation would arise not only from the amide and ester linkages in the alkoxyamine unit but also from the carboxylic acid group in the DABA unit. In addition, the experimental plot for the time course of the water contact angles were fitted by the following equation:[23]

$$\theta(t) = (\theta_{\mathrm{ini}} - \theta_{\mathrm{ter}})\exp\left(-\frac{t}{\tau}\right) - kt + \theta_{\mathrm{ter}} \quad (5.1)$$

where θ_{ini} and θ_{ter} are the initial and terminal values of the contact angles at t=0 and in a quasi-equilibrium state, τ is the time constant of the contact angle decay in the initial stage, and k is the constant related to water evaporation, respectively. Especially, τ is correlated to the relaxation time of the interfacial mobility, and the difference in the θ_{ini} and θ_{ter} values means the degree of surface reorganization induced by the water.[2123] With an increase in the film fabrication temperature, the τ value decreased from 6.77 to 5.87. Taking the FTIR spectra and dry densities into account, the decrease in the τ value is probably due to suppressing the aggregation of the polymer chains.

Table 5-3 θ_{ini}, θ_{ter}, and τ values of TEMPO-PA-COOH films fabricated at 70, 100, and 130 °C.

Temperature [°C]		70	100	130
θ_{ini}[a]	[°]	81.6	85.7	90.1
θ_{ter}[a]	[°]	ND	83.5	87.0
τ[a]	[s]	ND	6.77	5.87

[a]Time-resolved contact angle measurement was carried out by using the sessile drop method with water droplet of 2.0 μL.

Meanwhile, the difference in the θ_{ini} and θ_{ter} values increased from 2.18 to 3.11. Also, it is noted that the increase in the contact angles of the **TEMPO-PA-COOH** films along with the increasing film fabrication temperature was observed while all the **TEMPO-PA** films showed the same contact angles. This observation implies that more hydrophilic domains in **TEMPO-PA-COOH** are formed and the number of carboxylic acid groups to be involved in the surface reorganization is increased with the increase in the membrane preparation temperature. Such an interfacial behavior will be discussed in detail after presenting the tapping mode phase image by AFM measurements.

5.2.4.4 AFM observations

In order to clarify the phase separation between the hydrophilic and hydrophobic domains, the phase images of the surfaces of the **TEMPO-PA-COOH** films were recorded in the tapping mode AFM under ambient conditions (**Figure 5-13**). Although all the samples are random copolymers, nanoscaled phase separations are clearly observed. The bright and dark regions in the images are derived from the hard segments corresponding to the TEMPO units and the soft segments corresponding to the DABA units, respectively (**Figure 5-13**(above)). Furthermore, threshold method was carried out to obtain binarized images as shown in **Figure 5-13**(bottom), where the blue and red regions are derived from hydrophilic and hydrophobic segments corresponding to the TEMPO and DABA units, respectively.

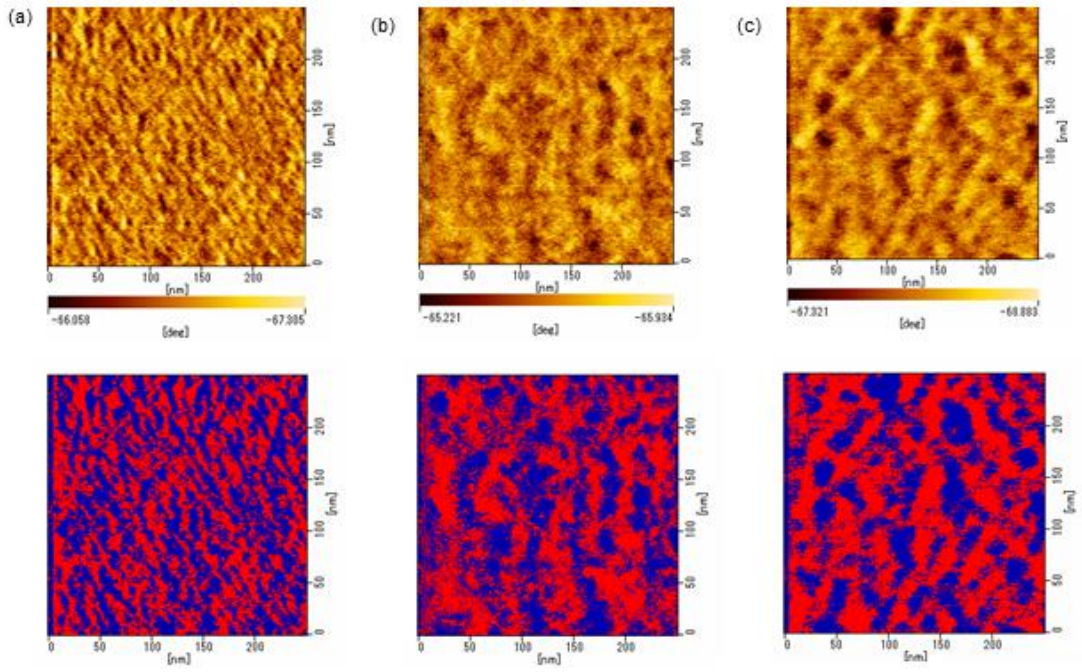

Figure 5-13 AFM tapping mode phase images (above) and their binarized image using threshold method (bottom) of **TEMPO-PA-COOH** films fabricated at (a) 70 °C, (b) 100 °C, and (c) 130 °C. Scan sizes are 250 × 250 nm^2.

The area fractions of hydrophilic domains of **TEMPO-PA-COOH** were summarized in **Table 5-4**. As can be seen in **Figure 5-13**(bottom) and **Table 5-4**, it is obvious that with an increase in the film fabrication temperature, the size of the hydrophilic domain has become larger whereas the total area of the hydrophobic domains increased. Based on this observation, it is suggested that both the DABA and TEMPO units tend to be discretely aggregated near the film surface. The hydrophobic TEMPO units are likely to be oriented toward the air to minimize the surface free energy, which is induced by the thermal reorganization behavior during the film fabrication process. In addition to the thermal reorganization behavior, the suppression of the hydrogen bondings in the casting solution would also assist in the separation of both the hydrophobic and hydrophilic domains. These results are in good agreement with the difference between θ_{ini} and θ_{ter} of **TEMPO-PA-COOH**. This is probably related to the hydrophilic domain size. For the **TEMPO-PA-COOH** film fabricated at 70 °C, the surface reorganization could not be observed since the small hydrophilic domains are surrounded and suppressed by the large amount of hydrophobic domains. By comparison of the differences in the θ_{ini} and θ_{ter} values of the **TEMPO-PA-COOH** films fabricated at 100 and 130 °C, an increase in the size of the hydrophilic domains would support the increase in the degree of surface reorganization induced by the water. The polymer aggregation and phase separation behaviors in the films were easily controlled by thermal treatments during the film fabrication, indicating that the dynamic covalent polymers can provide any desirable physical properties without chemical modification, inorganic-organic hybridization, etc.

Table 5-4 Area fraction of hydrophobic domains of **TEMPO-PA-COOH** films fabricated at different temperatures (70, 100, and 130 °C), estimated by threshold method.

Temperature	[°C]	70	100	130
Area fraction of hydrophobic domains	[%]	48.9	53.5	57.9

5.3 Conclusions

In this chapter, dynamic covalent PA composed of TEMPO units (**TEMPO-PA**) and dynamic covalent random coPA containing the DABA unit (**TEMPO-PA-COOH**) were successfully synthesized by a low temperature polycondensation. The fundamental properties and the effect of the radical crossover reaction of the prepared dynamic covalent polymers on the solution and solid-state structures were investigated. Based on the ^{1}H NMR and DLS measurements, it was revealed that a rise in solution temperature induced suppression of the hydrogen bonding between the amide linkages and the decrease in the hydrodynamic radius with an increase in the diffusion coefficient. During the thin-film fabrication process, hydrophobic TEMPO and hydrophilic DABA units tend to be discretely aggregated near the film surface to minimize the surface energy with the suppression of the hydrogen bondings. Therefore, a rise in the film fabrication temperature led to (1) a suppression of the interaction between the polymer chains, (2) formation of a clear phase separated structure, and (3) an increase in the number of carboxylic acids to be involved in the surface reorganization induced by water molecules, as characterized by the dry density, FTIR, water contact angle, and AFM measurements. These results indicated that the solid-state molecular aggregation structure of the dynamic covalent polymers can be easily controlled by a thermal treatment during the solidification process.

5.4 Experimental

5.4.1 Materials

4-Hydroxy-2,2,6,6-tetramethylpiperidinyloxy (TEMPO), styrene, Pd-C, 4-nitrobenzoyl chloride, 3,5-diaminobenzoic acid (DABA), and isophthaloyl chloride were purchased from TCI, Japan. Dehydrated pyridine, dehydrated tetrahydrofuran (THF), *N*-methylpyrrolidone (NMP), *N*,*N*-dimehylformamide (DMF), and dimethyl sulfoxide (DMSO) were obtained from Wako Pure Chemical Industries. NMP was dried over calcium hydride and distilled under nitrogen. **PA2-20** was synthesized by the same procedure described in chapter 2.

5.4.2 Synthesis of TEMPO-based diol compound (TEMPO-OH)

According to a previous report, the diol was successfully prepared. The obtained TEMPO-OH was fully characterized by infrared and nuclear magnetic resonance spectroscopies.

^{1}H NMR (300 MHz, $CDCl_3$, δ, 25 °C): 1.21 (s, -CH_3, 3H), 1.28 (s, -CH_3, 3H), 1.31 (s, -CH_3, 3H), 1.54 (s, -CH_3, 3H), 1.31-1.98 (m, -CH_2- 4H), 3.72 (dd, -C*H*-, *J* = 11.1 Hz, 1H), 4.01 (dd, -C*H*-, *J* = 11.1 Hz, 1H), 4.20 (t, -C*H*-, 6.0 Hz, 1H), 5.26 (m, -C*H*-, 1H), 7.26-7.34 (m, Ar*H*, 5H). IR (KBr), *v* (cm^{-1}): 3295 (O-H stretching), 3111-2855 (C-H stretching), 1456 (C=C stretching).

5.4.3 Synthesis of TEMPO-based dinitro compound (TEMPO-NO_2)

4-Nitrobenzoyl chloride (6.96 g, 37.5 mmol), TEMPO-OH (3.52 g, 12.5 mmol),

and, dehydrated THF (50 mL) were added into a two-necked 100 mL flask under a nitrogen atmosphere. After complete dissolution, dehydrated pyridine (3.96 mg, 50.0 mmol) was injected into the solution. After the solution was stirred at room temperature for 12 h, a white precipitate was removed by filtration, then the filtrate was evaporated. The crude product was purified by silica gel chromatography eluting with $CHCl_3$ to give TEMPO-NO_2 as a white powder.

Yield: 6.20 g (84 %). ^{1}H NMR (300 MHz, $CDCl_3$, δ, 25 °C): 0.79 (s, -C*H*$_3$, 3H), 1.23 (s, C*H*$_3$, 3H), 1.36 (s, -C*H*$_3$, 3H), 1.45 (s, -C*H*$_3$, 3H), 1.67-2.07 (m, -C*H*$_2$- 4H), 4.59 (dd, -C*H*$_2$-, *J* = 11.1 Hz, 1H), 4.90 (dd, -C*H*$_2$-, *J* = 11.1 Hz, 1H), 5.10 (t, -C*H*-, *J* = 6.0 Hz, 1H), 5.24-5.33 (m, -C*H*-, 1H), 7.27-7.38 (m, Ar*H*, 5H), 8.06-8.30 (m, Ar*H*, 8H). ^{13}C NMR (75 MHz, $CDCl_3$, δ, 25 °C) : 21.16, 21.27, 34.01, 34.13, 44.61, 44.67, 60.68, 60.79, 67.30, 68.55, 84.22, 123.74, 123.77, 127.79, 128. 37, 128.54, 130.84, 130.85, 135.61, 136.06, 139.92, 139.96, 150.78, 164.47(C=O), 164.65(C=O). IR (KBr), *v* (cm^{-1}): 3111-2855 (C-H stretching), 1711 (-C=O- stretching), 1607 (-C=C- stretching), 1526 (-NO_2 asymmetric stretching), 1349 (-NO_2 symmetric stretching).

5.4.4 Synthesis of TEMPO-based diamine compound (TEMPO-NH_2)

Under a hydrogen atmosphere, TEMPO-NO_2 (4.43 g, 7.5 mmol), Pd-C (886.83 mg, 20 wt%), and ethyl acetate (300 mL) were injected into a two-necked 500 mL flask. After stirring at room temperature for 24h, the solution was filtered off and evaporated to give the crude product. Finally, the crude product was purified by silica gel chromatography eluting with ethyl acetate/hexane (1/5, v/v) and dried in a vacuum at 70 °C for 24h.

Yield: 3.50 g (88 %). ^{1}H NMR (300 MHz, $CDCl_3$, δ, 25 °C): 0.76 (s, 3H), 1.21 (s, -C*H*$_3$, 3H), 1.35 (s, -C*H*$_3$, 3H), 1.44 (s, -C*H*$_3$, 3H), 1.61-2.01 (m, -C*H*$_2$-, 4H), 4.04 (s, -N*H*$_2$, 4H), 4.47 (dd, -C*H*$_2$-, *J* = 12.0 Hz, 1H), 4.90 (dd, -C*H*$_2$-, *J* = 11.4 Hz, 1H), 5.06 (t, -C*H*-, *J* = 6.0 Hz, 1H), 5.16-5.25 (m, -C*H*-, 1H), 6.63 (t, Ar*H*, *J* = 7.5 Hz, 4H), 7.34-7.39 (m, Ar*H*, 5H), 7.75-7.84 (m, 4H). ^{13}C NMR (75 MHz, $CDCl_3$, δ, 25 °C) : 21.30, 21.34, 34.14, 34.22, 45.01, 45.12, 60.66, 60.91, 66.32, 66.63, 84.55, 114.04, 119.95, 120.42, 128. 05, 128.37, 131.84, 131.96, 140.86, 151.11, 151.14, 166.58 (C=O), 166.72 (C=O). IR (KBr), *v* (cm^{-1}): 3475 (N-H asymmmetric stretching), 3369 (N-H symmetric stretching), 3227, 2973-2939 (C-H stretching), 1693 (-C=O- stretching), 1623 (N-H bending), 1602 (-C=C- stretching), 1517 (-C=C- stretching).

5.4.5 Synthesis of polyamide containing TEMPO moiety (TEMPO-PA)

TEMPO-NH_2 (531.7 mg, 1.0 mmol) was dissolved in dried NMP (3.0 mL) at room temperature and the solution was cooled to -78 °C. Subsequently, isophthaloyl chloride (203.0 mg, 1.0 mmol) was added and the temperature was slowly raised to room temperature. Then, the solution was stirred for 3 h and precipitated with methanol to obtain a white fibrous polymer. The obtained polymer was filtered off, washed several times with methanol, and dried in a vacuum oven for 48 h at 40 °C.

Yield: 615.4 mg (93%). M_n = 46400, M_w/M_n = 3.29. ^{1}H NMR (300 MHz, DMSO-d_6, δ, 40 °C): 0.73 (s, 3H), 1.29 (s, -C*H*$_3$, 3H), 1.40 (s, -C*H*$_3$, 3H), 1.52 (s, -C*H*$_3$, 3H), 1.73-2.01 (m, -C*H*$_2$-, 4H), 4.51 (dd, -C*H*$_2$-, *J* = 12.2 Hz, 1H), 4.76 (dd, -C*H*$_2$-, *J* = 12.2 Hz, 1H), 5.11-5.16 (m, -C*H*-, 2H), 7.27-7.46 (m, Ar*H*, 5H), 7.71 (t, Ar*H*, *J* = 7.5 Hz, 1H), 7.86-7.95 (m, Ar*H*, 8H), 8.16 (d, Ar*H*, *J* = 7.5 Hz, 5H), 8.57 (s, Ar*H*, 1H), 10.71 (s,

-N*H*-,1H). ^{13}C NMR (75 MHz, DMSO-d_6, δ, 40 °C) : 17.08, 20.70, 28.87, 29.96, 33.2, 44.18, 48.41, 60.22, 65.80, 66.33, 83.63, 119.70, 124.41, 124.85, 127.28, 127.67, 127.89, 128.13, 128.80, 130.08, 131.18, 134.79, 139.93, 143.62, 143.70, 164.93 (C=O), 165.10 (C=O), 165.46 (C=O), 165.50 (C=O). IR (KBr), *v* (cm^{-1}): 3295 (N-H stretching), 2973-2872 (C-H stretching), 1716 (-C=O- stretching), 1671 (-C=O- stretching), 1601 (-C=C- stretching), 1527 (-N-H bending).

5.4.6 Synthesis of random copolyamide containing TEMPO moiety (TEMPO-PA-COOH)

TEMPO-NH_2 (2346.3 mg, 4.4 mmol) and 3,5-diamino benzoic acid (668.5 mg, 4.4 mmol) were dissolved in dried NMP (18.7 mL) at room temperature. After the solution was cooled to -78 °C, isophthaloyl chloride (1791.8 mg, 8.8 mmol) was added. After the temperature was slowly raised up to room temperature, the solution was stirred for 3 h. Subsequently, a viscous reaction solution was precipitated with methanol to give a white fibrous polymer. The obtained polymer was filtered off, washed several times with methanol, and dried in a vacuum oven for 48 h at 40 °C.

Yield: 4032 mg (97%). ^{1}H NMR (300 MHz, DMSO-d_6, δ, 40 °C): 0.70 (s, 3H), 1.13 (s, -C*H*$_3$, 3H), 1.26 (s, -C*H*$_3$, 3H), 1.37 (s, -C*H*$_3$, 3H), 1.53-1.98 (m, -C*H*$_2$-, 4H), 4.48 (dd, -C*H*$_2$-, *J* = 12.2 Hz, 1H), 4.74 (dd, -C*H*$_2$-, *J* = 12.2 Hz, 1H), 5.07-5.13 (m, -C*H*-, 2H), 7.26-7.43 (m, Ar*H*, 5H), 7.67 (t, Ar*H*, *J* = 7.5 Hz, 2H), 7.83-7.92 (m, Ar*H*, 8H), 8.16 (s, Ar*H*, 6H), 8.52-8.68 (m, Ar*H*, 3H), 10.60. 10.66 (s, -N*H*-,4H). ^{13}C NMR (75 MHz, DMSO-d_6, δ, 40 °C) : 20.86, 33.51, 44.27, 44.36, 60.02, 60.26, 65.93, 66.04, 66.48, 66.53, 83.64, 116.47, 116.99, 119.81, 124.50, 124.93, 127.40, 127.82, 128.03, 128.28,

128.91, 130.28, 131.12, 131.15, 131.29, 131.61, 134.98, 135.06, 139.69, 139.72, 140.16, 143.70, 143.72, 143.78, 143.80, 165.07 (C=O), 165.23 (C=O), 165.33 (C=O), 165.46 (C=O), 165.63 (C=O), 165.69 (C=O), 165.75 (C=O), 167.25 (C=O). IR (KBr), ν (cm^{-1}): 3295 (N-H stretching), 2973-2872 (C-H stretching), 1719 (-C=O- stretching), 1684 (-C=O- stretching), 1674 (-C=O- stretching), 1597 (-C=C- stretching), 1526 (-N-H bending).

5.4.7 Fabrication of TEMPO-PA and TEMPO-PA-COOH films

The 10 wt% solutions of the obtained **TEMPO-PA** and **TEMPO-PA-COOH** films were prepared in DMSO. Subsequently, the polymer solutions were degassed by freeze-pump-thaw and filtered through a 0.45 μm poly(vinylidene fluoride) membrane filter in a glovebox. The polymer solutions were coated onto a clean glass substrate by a spin-coating method to form the as-cast films with less than 2.0 μm thickness. The as-cast films were then heated at various temperatures (70, 100, and 130 °C) for 3 h and dried under vacuum for at least 24 h before evaluation of the intrinsic properties of the films.

5.4.8 Evaluation of the stability and thermal rearrangement behavior of TEMPO unit

To evaluate the radical stability in solution, **TEMPO-PA** (M_n = 46400, $M_w/M_n = 3.30$) was dissolved in DMSO-d_6 at a concentration of 6 mg mL^{-1} and then heated at 130 °C under an air or argon atmosphere. ^{1}H NMR measurements were carried out for the samples collected at 16 and 24 h. After **TEMPO-PA** (M_n = 46400, $M_w/M_n = 3.30$) was dissolved in DMF with 0.05 M LiBr at a concentration of 2 mg mL^{-1}, the polymer solution was degassed by four cycles of freeze-pump-thaw and then heated at 130 °C under an argon atmosphere to study the thermal rearrangement behavior. GPC measurements of the samples collected at 0.5, 1, 2, 4, 16, and 24, respectively, were conducted.

5.4.9 Measurements

Proton nuclear magnetic resonance (^{1}H NMR) spectra were recorded on a Bruker DPX300S spectrometer in DMSO-d_6 calibrated to tetramethylsilane as an internal standard (δ_H 0.00). FTIR spectra were measured on a Horiba FT-720 spectrometer. Electron spin resonance (ESR) was measured by JEOL JES-X320 T-band ESR spectrometer equipped with a JEOL DVT temperature controller. The measured samples in DMSO at a polymer concentration of 10 wt% were contained in 0.8 mm glass capillaries, which were sealed after being degassed by four cycles of freeze-pump-thaw. The microwave power was 0.5 mW, the field modulation was 0.2 mT with a time constant of 0.03 s, and the number of scans was 16. The relative intensities were calculated using the integral areas in the spectra. The thermal analysis (TGA) was

performed in a nitrogen atomosphere on a RIGAKU Thermo plus EVO TG8120 thermal analyzer under a nitrogen atmosphere for the thermogravimetry (TG) and differential thermal analysis (DTA). Before the evaluation, all the samples were preheated at 80 °C to remove any moisture and residual solvents in the TG/DTA furnace. The samples were subsequently cooled to 30 °C and then heated to 500 °C at the heating rate of 10 °C/min. Inherent viscosity was measured at 30 °C in DMSO at a polymer concentration of 0.5 g L^{-1}. Gel permeation chromatography was measured on Viscotek GPC-1000 system equipped with a TDA 302 triple detector and a TSK-GEL α-M column with a conventional calibration curve based on polystyrene standards. DMF with 0.05 M LiBr was used as the carrier solvent at flow rate of 0.6 mL/min. The number and weight average molecular weights (M_{n} and M_{w}) were calculated based on the light-scattering data. Dynamic light scattering measurements were performed on Wyatt DynaPro NanoStar. The hydrodynamic diameter (R_H) and the diffusion coefficient (D) of the prepared polymers in DMSO at a concentration of 2.0 wt% were calculated on the basis of CONTIN analysis using DYNAMICS software (Wyatt Technology Co., Ltd.). To avoid the side reaction between the TEMPO unit and oxygen, the polymer solutions were filtered through a 0.45 μm membrane filter after four cycles of freeze-pump-thaw and transferred to quartz cells in a glove box. Viscosities of DMSO at 70, 100, and 130 °C were determined to be 1.277, 0.855, and 0.408 mPa·s, respectively, by the viscometer. Also, refractive indices were found to be 1.452, 1.431, and 1.392, respectively, by the interferometric method. The polymer densities in the thin films were determined using an Alfa Mirage SD-200L electronic densimeter at ambient temperature (24-25 °C). Ethanol was selected as the non-solvent. Contact angles of the thin films were measured by the sessile drop method using a DropMaster 500, Kyowa

Interface Science Co., Ltd., at ambient temperature (24-25 °C). As the probe liquid, a purified water droplet with the volume of a 2.0 μL was used and the contact angles were calculated on the basis of a contour curve-fitting method using FAMAS software (Kyowa Interface Science Co., Ltd.). The surface morphology was characterized using atomic force microscopy (AFM, SPA400, SII Nanotechnology) in the phase contrast mode.

5.5 References

(1) Yuan, C.; Rong, M. Z.; Zhang, M. Q.; Zhang, Z. P.; Yuan, Y. C. *Chem. Mater.* **2011**, *23*, 5076–5081.

(2) Rao, J.; De, S.; Khan, A. *Chem. Commun.* **2012**, *48*, 3427–3429.

(3) Rao, J.; Khan, A. *Polym. Chem.* **2013**, *4*, 2691–2695.

(4) Otsuka, H.; Aotani, K.; Higaki, Y.; Amamoto, Y.; Takahara, A. *Macromolecules* **2007**, *40*, 1429–1434.

(5) Otsuka, H.; Aotani, K.; Higaki, Y.; Takahara, A. *J. Am. Chem. Soc.* **2003**, *125*, 4064–4065.

(6) Espeso, J. F.; Lozano, A. E.; de la Campa, J. G.; Garcia-Yoldi, I.; de Abajo, J. *J. Polym. Sci. Part A Polym. Chem.* **2010**, *48*, 1743–1751.

(7) García, J. M.; García, F. C.; Serna, F.; de la Peña, J. L. *Prog. Polym. Sci.* **2010**, *35*, 623–686.

(8) Shibasaki, Y.; Abe, Y.; Sato, N.; Fujimori, A.; Oishi, Y. *Polym. J.* **2010**, *42*, 72–80.

(9) Tanatani, A.; Yokoyama, A.; Azumaya, I.; Takakura, Y.; Mitsui, C.; Shiro, M.; Uchiyama, M.; Muranaka, A.; Kobayashi, N.; Yokozawa, T. *J. Am. Chem. Soc.* **2005**, *127*, 8553–8561.

(10) Shi, H.; Zhao, Y.; Zhang, X.; Zhou, Y.; Xu, Y.; Zhou, S.; Wang, D.; Han, C. C.; Xu, D. *Polymer* **2004**, *45*, 6299–6307.

(11) Schulze, M.; Michen, B.; Fink, A.; Kilbinger, A. F. M. *Macromolecules* **2013**, *46*, 5520–5530.

(12) Xie, W.; Ju, H.; Geise, G. M.; Freeman, B. D.; Mardel, J. I.; Hill, A. J.; McGrath, J. E. *Macromolecules* **2011**, *44*, 4428–4438.

(13) Shimazu, a; Ikeda, K.; Miyazaki, T.; Ito, Y. *Radiat. Phys. Chem.* **2000**, *58*, 555–561.

(14) Lin, H.; Wagner, E.; Swinnea, J.; Freeman, B.; Pas, S.; Hill, a; Kalakkunnath, S.; Kalika, D. *J. Memb. Sci.* **2006**, *276*, 145–161.

(15) Aiba, M.; Tokuyama, T.; Matsumoto, H.; Tomioka, H.; Higashihara, T.; Ueda, M. *J. Polym. Sci. Part A Polym. Chem.* **2014**, *52*, 3453–3462.

(16) Telitel, S.; Amamoto, Y.; Poly, J.; Morlet-Savary, F.; Soppera, O.; Lalevée, J.; Matyjaszewski, K. *Polym. Chem.* **2014**, *5*, 921–930.

(17) Xie, G.; Pino, P.; Lorenzil, G. P. *Macromolecules* **1990**, *23*, 2583–2588.

(18) Yamauchi, K.; Kuroki, S.; Fujii, K.; Ando, I. *Chem. Phys. Lett.* **2000**, *324*, 435–439.

(19) Skrovanek, D. J.; Howe, S. E.; Painter, P. C.; Coleman, M. M. *Macromolecules* **1985**, *18*, 1676–1683.

(20) Cassie, A. B. D.; Baxter, S. *Trans. Faraday. Soc.* **1944**, *40*, 546–551.

(21) Horinouchi, A.; Tanaka, K. *RSC Adv.* **2013**, *3*, 9446–9452.

(22) Oda, Y.; Horinouchi, A.; Kawaguchi, D.; Matsuno, H.; Kanaoka, S.; Aoshima, S.; Tanaka, K. *Langmuir* **2014**, *30*, 1215–1219.

(23) Horinouchi, A.; Atarashi, H.; Fujii, Y.; Tanaka, K. *Macromolecules* **2012**, *45*, 4638–4642.

Chapter 6

General Conclusions

Conclusions of each chapter and further prospect for the development of polymeric membranes for water treatment are summarized in this chapter.

The general introduction regarding the background of this study is described in chapter 1.

In chapter 2, wholly-aromatic polyamide (PA) membranes were prepared and their transport properties were characterized. With the increase in the hydrophilic carboxylic acid groups, the water sorption coefficient was slightly increased. However, the enhancement of water transport properties induced by the introduction of the hydrophilic group was not substantial. Therefore, **PA2-20-additive** was prepared via non-solvent induced phase separation method. As a result, **PA2-20-additive** showed higher water flux (14.2 L m^{-2} h^{-1}) and NaCl rejection (35 %). The formation of pores was supported by differential scanning calorimetry and scanning electron microscope. Also, attenuated total reflectance Fourier transform infrared spectroscopy and solid-state

carbon polarization and magic angle spinning nuclear magnetic resonance spectroscopy demonstrated that the aggregation of polymer chains due to the hydrogen bonds among the amide linkages was suppressed probably due to the coordination of the aqueous additives to the amide linkage.

In chapter 3, the synthesis, conformational preferences, hydrogen bonding behaviors, and membrane properties of partially *N*-methylated random aromatic coPAs (**PA-X-Ys**) were investigated. **PA-X-Ys** were prepared by the low temperature polycondensations of isophthaloyl chloride with 3,5-diaminobenzoic acid, *N*,*N*'-dimethyl-4,4'-diaminodiphenyl ether (MDAE), and 4,4'-diaminodiphenyl ether. The incorporation of the *N*-methyl amide linkages into the polymer backbone decreased the content of the *cis* conformation in the *N*-methyl amide linkages and suppressed the hydrogen bondings among the amide linkages, which assisted the surface reorientation of the carboxylic acid. These experimental results indicated that the suppression of the hydrogen bonding and the existence of the tertiary amide linkage in the *cis* conformation induced the loose packing of the polymer chains. Indeed, the *N*-methyl amide linkage increased the free-volume. As a result, the incorporation of the *N*-methyl amide linkage increased water flux and decreased salt rejection due to the increase in water and salt diffusion coefficients.

In chapter 4, semipermeable membranes based on various polybenzimidazoles (PBIs) were prepared and characterized. PBI with *N*-butylsufonate (**BSPBI**) was prepared by the two steps, that is, deprotonation of PBI using lithium hydride, followed by treatment with 1,4-butanesultone. From WAXD analyses, FTIR spectra, and time-resolved contact angle measurements, it was confirmed that the suppression of the hydrogen bonding induced by the *N*-substitution and the cross-linked structure led to the

polymer packing disruption. The cross-linking reaction of **BSPBI** with divinyl sulfone induced the change of the pore size distribution, where the selective permeation of water molecule was successfully achieved. As a result, simultaneous improvement in water permeability and selectivity was achieved by the simple cross-linking reaction due to the selective increase in water diffusion coefficient. The cross-linked **BSPBI** (**CL-BSPBI**) membrane exhibited considerably high water permeability (6.24 L μm m^{-2} h^{-1} bar^{-1}) with relatively low NaCl permeability (0.144×10^{-8} cm^2 s^{-1}), compared with conventional polymeric membranes.

In chapter 5, thermally-rearrangeable aromatic PA (**TEMPO-PA**) and random coPA (**TEMPO-PA-COOH**) incorporating alkoxyamine moieties in the main chain were synthesized and then the effect of the thermal reorganization behavior on their solution and solid-state structures was investigated. ^{1}H NMR spectra and DLS measurements revealed that a rise in the solution temperature suppressed hydrogen bondings between the amide linkages as well as decreasing the hydrodynamic radius. For the thin films fabricated at high temperature, on the other hand, both the decrease in the density and the suppression of the hydrogen bonding were observed. Furthermore, the surface wettability and phase separation behaviors of the **TEMPO-PA-COOH** containing both reversible covalent bonds and hydrophilic units were characterized by time-resolved water contact angle measurements and AFM observations, respectively. These analyses clearly showed that the surface hydrophilicity of the random copolyamide had decreased. The water-induced surface reorganization (i.e., phase separation of hydrophilic and hydrophobic domains) easily occurred to minimize the surface energy via a radical crossover reaction. This study indicated that both the solution structure and the solid-state molecular aggregation structure of the dynamic

covalent polymers can be easily controlled by a thermal trigger, and brought a new option for controlling the high-order structure of polymer solutions and solids.

As described above, we have investigated the influence of chemical and molecular aggregation structures of various PAs on fundamental transport properties in chapters 2 and 3 as a first step of this study. In chapter 3, we have concluded that it seems difficult to independently control permeability and selectivity by designing the polymer backbone. The MDAE unit-induced the suppression of the hydrogen bonding between the amide linkages enables an increase in free volume while a traditional trade-off relationship, that is the permeability gain and the concomitant selectivity loss, is also observed. For example, **PA-20-60** with large free volume elements (0.089 nm^3) showed higher water flux (2.25 L m^{-2} h^{-1}) and lower NaCl rejection than **PA-20-0** with small free volume one (0.069 nm^3). By expanding the approach for suppression of polymer/polymer interaction, crosslinking reaction between the *N*-substituted PBIs during the desolvation process has been examined in chapter 4. Especially, the free volume elements (radius: 0.14-0.24 nm) has played an important role in the selective enhancement of water diffusion coefficient, as can be seen in the **CL-BSPBI**. For further improvement in membrane performance, we need to minimize the membrane thickness and to afford high pressure tolerance for increasing water flux as high as possible by using a thin-active-layer composite membrane. If a composite membrane with a **CL-BSPBI** active layer are operated without a pressure-induced compaction and concentration polarization under some practical RO operating conditions (*e.g.*, ΔP = 75 bar and $\Delta\pi$ = 49.8 bar for 1M NaCl aq), water flux and NaCl rejection can be

estimated to be 157.3 L m^{-2} h^{-1} and 99.9 %, respectively. These values are comparable to those of the cross-linked PA membranes and cellulose acetate asymmetric membranes.

In order to prepare the fine structure-controlled semipermeable membrane materials, ideally, it is necessary to develop the way for forming monomodal free-volume radius distribution around 0.14-0.24 nm. Unfortunately, this cannot be accomplished by cross-liking reaction during desolvation process even in **CL-BSPBI** membrane. To address this problem, utilization of radical crossover reaction on the hydrogen bonding and aggregation behavior was presented in chapter 5. Although the free-volume radius distribution of **TEMPO-PAs** still remains unclear, the molecular rearrangement of **TEMPO-PA-COOH** was effectively occurred at the membrane-air surface to reduce surface free energy, supported by the time resolved contact angle measurements and AFM observations. This indicates that there is a probability that **TEMPO-PA-COOH** can alter free volume near the membrane surface. Also, we think that alkoxyamine-based cross-linked PBIs can bring new potential to optimize the free-volume radius distribution via radical cross-over reaction.

Finally, the author believes that some developments and findings in this study will be useful for the development of the next generation water purification systems.

Appendix

List of publications (concerning this dissertation)

(1) ‘‘Improvement in Semipermeable Membrane Performance of Wholly Aromatic Polyamide through an Additive Processing Strategy’’ Aiba, M.; Tokuyama, T.; Baba, S.; Matsumoto, H.; Tomioka, H.; Higashihara, T.; Ueda, M. *J. Polym. Sci. Part A Polym. Chem.* **2014**, *52*, 1275–1281.

(2) ‘‘Effect of *N*-Methyl Amide Linkage on Hydrogen Bonding Behavior and Water Transport Properties of Partially *N*-methylated Random Aromatic Copolyamides’’ Aiba, M.; Tokuyama, T.; Matsumoto, H.; Tomioka, H.; Higashihara, T.; Ueda, M. *J. Polym. Sci. Part A Polym. Chem.* **2014**, *52*, 3453–3462.

(3) ‘‘Effect of Primary Structure on Permselectivity of Ultrathin Semipermeable Polybenzimidazole Membrane’’ Aiba, M.; Tokuyama, T.; Matsumoto, H.; Tomioka, H.; Higashihara, T.; Ueda, M. *J. Appl. Polym. Sci.* **2015**, *132*, 41531/1-7.

(4) ‘‘Enhancement of Salt Rejection and Water Flux by Crosslinking-Induced Microstructural Change of *N*-substituted Polybenzimidazole Membranes’’ Aiba, M.; Tokuyama, T.; Matsumoto, H.; Tomioka, H.; Higashihara, T.; Ueda, M. *Mater. Res. Symp. Proc.* **2015**, *1745*, FF12.05/1–6

(5) ‘‘Novel Membrane Development in Pressure Retarded Osmosis: Ultrathin Semipermeable Membrane Based on Cross-linked Polybenzimidazole’’ Aiba, M.; Tokuyama, T.; Matsumoto, H.; Tomioka, H.; Higashihara, T.; Ueda, M. *Desalination* **2015**, submitted.

(6) ‘‘Triggered Structure Control of Dynamic Covalent Aromatic Polyamides: Effect of

Thermal Reorganization Behavior in Solution and Solid States'' Aiba, M.; Higashihara, H.; Ashizawa, M.; Otsuka, H.; Matsumoto, H.; *Macromolecules* **2015**, submitted.

List of other publications

(7) ''Nucleobase-functionalized ABC triblock copolymers: self-assembly of supramolecular architectures'' Zhang, K.; Fahs, G. B.; Aiba, M.; Moore, R. B.; Long, T. E. *Chem. Commun*. **2014**, *50*, 9145–9148.

(8) ''Nucleobase-functionalized acrylic ABA triblock copolymers and supramolecular blends'' Zhang, K.; Aiba, M.; Fahs, G. B.; Hudson, A. G.; Chiang, W. D.; Moore, R. B.; Ueda, M.; Long, T. E. *Polym. Chem.* **2015**, *6*, 2434-2444.

(9) ''Development of nano-structured membranes and their application in water treatments: from control of molecular interactions to utilization of nanomaterials'' Aiba, M.; Konosu, Y.; Matsumoto, H. *Kino Zairyo* **2015**, *35*, 29-34.

List of presentations (concerning this dissertation)

(1) ''Development of Forward Osmosis Polyamide Membrane Via Non-solvent Induced Phase Separation'' Aiba, M.; Tokuyama, T.; Matsumoto, H.; Tomioka, H.; Higashihara, T.; Ueda, M. *62nd Symposium on Macromolecules*, Kanazawa (Japan), September 2013 (oral).

(2) ''Polyamide-Based Freestanding Ultrathin Membranes for Forward Osmosis'' Aiba, M.; Tokuyama, T.; Matsumoto, H.; Tomioka, H.; Higashihara, T.; Ueda, M. *2nd*

International Education Forum on Environment and Energy Science, California (USA), December 2013 (oral).

(3) ‘‘Development of Membranes Based on Polybenzimidazoles with Crown Ether Moiety’’ Aiba, M.; Ashizawa, M.; Higashihara, T.; Ueda, M.; Matsumoto, H. *63rd Symposium on Macromolecules,* Nagasaki (Japan), September 2014 (poster).

(4) ‘‘Effect of *N*-Methyl Amide Linkage on Hydrogen Bonding Behavior and Membrane Properties of Partially *N*-Methylated Random Aromatic Copolyamides’’ Aiba, M.; Tokuyama, T.; Matsumoto, H.; Tomioka, H.; Higashihara, T.; Ueda, M. *3rd International Education Forum on Environment and Energy Science,* Perth (Australia), December 2014 (oral).

(5) ‘‘Enhancement of Salt Rejection and Water Flux by Crosslinking-Induced Microstructure Change of *N*-Substituted Polybenzimidazole Membranes’’ Aiba, M.; Tokuyama, T.; Matsumoto, H.; Tomioka, H.; Higashihara, T.; Ueda, M. *2014 MRS Fall Meeting & Exhibit,* Boston (USA), December 2014 (oral).

(6) ‘‘Development of Semipermeable Membrane Based On Cross-linked *N*-Substituted Polybenzimidazole’’ Aiba, M.; Tokuyama, T.; Matsumoto, H.; Tomioka, H.; Higashihara, T.; Ueda, M. *64th SPSJ Annual Meeting*, Sapporo (Japan), May 2015 (oral).

(7) ‘‘Effect of *N*-Methylated Amide Linkage on Hydrogen Bonding Behavior and Water Transport Properties of Partially *N*-Methylated Random Aromatic Copolyamides” Aiba, M.; Tokuyama, T.; Matsumoto, H.; Tomioka, H.; Higashihara, T.; Ueda, M. *64th SPSJ Annual Meeting*, Sapporo (Japan), May 2015 (poster).

List of patents

(1) ‘‘Semi-permeable membrane and method for manufacturing same, and concentration-difference power generating method using semi-permeable membrane’’ Tokuyama, T.; Hiranabe, R.; Tomioka, H.; Kurihara, M.; Ueda, M.; Higashihara, T.; Aiba, M.; *PCT Int. Appl.* **2013**, (WO 2013172330)

Acknowledgement

The studies described in this dissertation have been carried out under the direction of Assoc. Prof. Hidetoshi Matsumoto, Department of Organic and Polymeric Materials, Graduate School of Science and Engineering, Tokyo Institute of Technology, during AY 2013 to 2016. The studies are concerned with the development of novel polymeric membranes for water treatment.

The author is sincerely grateful to Academy for Co-creative Education of Environment and Energy Science (ACEEES), Tokyo Institute of Technology, for financial supports for living and research during AY 2012 to 2016. Without financial support by ACEEES, the studies cannot be completed.

The author wishes to express his gratitude to Assoc. Prof. Hidetoshi Matsumoto for his ardent guidance and invaluable suggestion throughout this work. The author is sincerely grateful to Emeritus Prof. Mitsuru Ueda, Tokyo Institute of Technology, and Assoc. Prof. Tomoya Higashihara, Yamagata University, for his helpful advice and encouragement about this work including writing papers. The author also thanks to Assistant Prof. Minoru Ashizawa and all members of Matsumoto group for their collaboration.

The author also expresses his appreciation to Mr. Hiroki Tomioka and Mr. Takahiro Tokuyama, Toray Industries Inc., for their kind experimental assistance and benignant discussion. The author is sincerely grateful to Prof. Mitsuru Higa, Yamaguchi University, for the experimental advice for the water transport instruments. The author acknowledges Dr. Kenji Ito, National Institute of Advanced Industrial Sicience and Technology, for the appropriate advice and experimental assistance for PALS measurements. The author is grateful to Prof. Hideyuki Otsuka and Mr. Takahiro Kosuge for a kind discussion and experimental support for ESR measurements. Acknowledgement is also made for Assoc. Prof. Masatoshi Tokita and Ms. Chiharu Takahashi for the experimental support of WAXD measurements. The author is grateful to Prof. Masa-aki Kakimoto and Ms. Yu Sudo for the help in GPC measurements.

The author would like to be grateful to Prof. Timothy E. Long, Virginia Polytechnic Institute and State University, for giving me a precious opportunity to

collaborate with him for three months and his ardent guidance and suggestion. The author also gives his thank to Ms. Keren Zhang in Long group for her kind helps and supports.

Finally, the author wishes to express his deep appreciation to his parents, brother, sister, Shoji Aiba, Nobuko Aiba, Hisaki Aiba, and Yuki Aiba for their constant assistance and kind support, and also special thanks to all my friends.